

Thickness Measurements below the Rayleigh
Depth Resolution Limit Using
Frequency-Modulated Continuous-Wave
Millimeter and Terahertz Waves

*Schichtdickenbestimmungen unterhalb der
Rayleigh-Tiefenauflösungsgrenze mit
frequenzmodulierten Dauerstrich-Millimeter-
und Terahertzwellen*

vom Fachbereich Elektrotechnik und Informationstechnik der Technischen Universität
Kaiserslautern zur Verleihung des akademischen Grades Doktorin oder Doktor der
Ingenieurwissenschaften (Dr.-Ing.) genehmigte Dissertation

Nina Susan Schreiner

Geburtsort: Homburg / Saar

Dekan: Prof. Dr. Marco Rahm

1. Gutachter: Prof. Dr. Ralph Urbansky
2. Gutachter: Prof. Dr. Georg von Freymann

Tag der mündlichen Prüfung: 2. November 2021
D 386

Lebenslauf

Nina Susan Schreiner

Berufserfahrungen

06/15-06/21 Technische Universität Kaiserslautern (TUK), FB Physik /
Fraunhofer Institut für physikalische Messtechnik / Fraun-
hofer Institut für Techno- und Wirtschaftsmathematik, wis-
senschaftliche Mitarbeiterin

Akademische Ausbildung

04/16-11/21 Promotionsstudium Elektrotechnik und Informationstechnik,
TUK

04/09-05/15 Studium Elektrotechnik und Informationstechnik, Kommu-
nikationstechnik, TUK

Abschluss Master of Science, 03/15

Projektarbeit im Bereich "Embedded-Systems", 11/13-06/14

Abschluss Bachelor of Science, 02/13

Kurzfassung

Das zerstörungsfreie Testen von Erzeugnissen mehrlagiger Materialien wird sowohl im wissenschaftlichen als auch im industriellen Umfeld zunehmend eingesetzt. Insbesondere die Entwicklungen in der Millimeterwellen- und Terahertztechnik eröffnen durch die nicht-ionisierenden Eigenschaften dieses Wellenlängenbereichs neue Anwendungsfelder wie der berührungslosen Schichtdickenmessung. Bei den hierfür häufig verwendeten Messverfahren führen übliche Analysemethoden zu einer Auflösungsbegrenzung, die von der Bandbreite des Messsystems abhängt. In dieser Arbeit wird analysiert, wie sich mit einem modellbasierten Signalauswertungsansatz Schichtdicken unterhalb dieser Auflösungsgrenze zuverlässig bestimmen lassen.

Im Kontext dieser Arbeit wird die elektromagnetische Strahlung durch das frequenzmodulierte Dauerstrichverfahren (FMCW von *frequency-modulated continuous-wave*) erzeugt und detektiert. Hierfür werden Proben mit Wellen bestrahlt, deren Frequenzen kontinuierlich erhöht werden, um das frequenzspezifische Übertragungsverhalten zu erfassen. Die Grenzschichten zwischen Materialien unterschiedlicher Brechungsindizes erzeugen Reflexionen, die sich im resultierenden Messsignal als additive Schwingung einfügen, deren Frequenzen von den Laufzeiten der Wellenanteile abhängen. Um deterministische Störanteile wie die Reflexionen durch das Messsystem zu kompensieren, werden die Messdaten kalibriert. Durch eine genaue Bestimmung der korrigierten Frequenzanteile können somit die Dicken der einzelnen Materialschichten berechnet werden. Zur Analyse kann die diskrete Fouriertransformation verwendet werden. Eine einzelne Schwingung im Messsignal wird auf einen ausgedehnten Hauptanteil (*peak*) mit einem Maximum an der gesuchten Frequenz abgebildet. Um diesen herum treten Nebenanteile (*side lobes*) auf. Die Messdauer bzw. die Bandbreite der Frequenzmodulation bestimmt die Breite dieser Spektralanteile und somit den Abstand zwischen dem Maximum und der nächsten Nullstelle, der als Rayleigh-Auflösungsgrenze bezeichnet wird. Schichtdicken unterhalb dieses Wertes können ausschließlich durch den Fouriertransformationsansatz nicht bestimmt werden, da sich die Hauptanteile überlagern. Für dünnere Schichten werden in dieser Arbeit alternative Signalverarbeitungsmethoden untersucht, die nicht durch die Rayleigh-Auflösungsgrenze limitiert sind. Hierzu wird das Messsignal einerseits durch spektrale Schätzverfahren und andererseits durch einen alternativen modellbasierten Ansatz nachgebildet.

Spektrale Schätzverfahren basieren auf Modellen, die es ermöglichen, das Leis-

tungsdichtespektrum des Messsignals durch wenige zu bestimmende Parameter zu nähern. Zwei spezielle Varianten der Verfahren, die modifizierte Kovarianzmethode und der MUSIC-Algorithmus (*multiple signal classification*) werden gewählt, um beispielhaft ihre Zuverlässigkeit für die Schichtdickenauswertung zu analysieren. Die modifizierte Kovarianzmethode basiert darauf, dass sich Anteile des Messsignals aus vorangegangenen Punkten abschätzen lassen. Demnach kann ein Filter entworfen werden, welches diese Charakteristik aufweist und eine Nachbildung spezieller Eigenschaften des Leistungsdichtespektrums ermöglicht. Unter Anwendung der Systemtheorie ergibt sich aus der Anzahl der Exponentialfunktionen des Messsignals die Modellordnung, die Vielzahl der Polstellen des Filters. Aus den Positionen der Polstellen wiederum lassen sich Schätzwerte für die gesuchten Frequenzanteile berechnen. Das Modell des MUSIC-Algorithmus gleicht einer Überlagerung komplexer Exponentialfunktionen und additiven weißen gaußschen Rauschen. Aufgrund der Orthogonalität beider Anteile lassen sich durch Eigenwertzerlegung Rauscheigenvektoren bestimmen. Diese werden zur Erzeugung eines Filters verwendet, dessen Inverses eine Schätzung des Leistungsdichtespektrums und der gesuchten Frequenzanteile ermöglicht. Durch Simulationen wird dargelegt, dass die Auflösungsgrenze der diskreten Fouriertransformation unterschritten werden kann, und, dass keine Nebenanteile zu beobachten sind. Die Kalibrierung und das vergleichsweise niedrige Signal-Störleistungsverhältnis beeinflussen jedoch die Modellcharakteristik und hierdurch die Modellordnung für beide Verfahren. Demnach können verfälschte Frequenzanteile und abweichende Schichtdicken beobachtet werden.

Die Verwendung eines alternativen modellbasierten Verfahrens kann die Auswertung falscher Frequenzanteile reduzieren: Ein Modell, welches der formalen Beschreibung des Messsignals entspricht, wird an dieses angepasst, wobei die Korrelation zwischen beiden als Gütemaß dient. Die Parameter, die das Modellsignal mit der höchsten Übereinstimmung erzeugen, entsprechen dann einer geeigneten Schätzung der Schichtdicken. A priori Abschätzungen der einzelnen Dicken können verwendet werden, um Suchintervalle entsprechend einzuschränken. Die formale Beschreibung des Messsignals besteht aus Hauptreflexionen, den ersten Strahl- bzw. Signalanteilen, die von den verschiedenen Grenzflächen erzeugt werden, und weiteren Mehrfachreflexionen. Es konnte gezeigt werden, dass der Einfluss Letzterer signifikant ist, wenn die Kontraste zwischen den Brechungsindizes benachbarter Materialien hoch sind, oder, wenn sich der Schichtaufbau auf einem leitenden Substrat befindet. Um Mehrfachreflexionen effizient zu berechnen, wird eine Transfermatrixmethode modifiziert. Sie beschreibt die einzelnen Schichten als Vierpole und die Wellenausbreitung als Matrixmultiplikation. Die Modifikation besteht darin, dass anstelle der vollständigen Beschreibung lediglich die Auswirkungen auf das Messsignal berechnet werden. Die Auswertung von gemessenen Signalen kann das Verfahren sowie die Fähigkeit des modellbasierten Ansatzes validieren, Schichten unterhalb der Rayleigh-Auflösungsgrenze zu bestimmen.

Neben dem Auflösungsvermögen ist die Genauigkeit der Messergebnisse ein entscheidendes Kriterium für die Zuverlässigkeit des Mess- und Auswertungsver-

fahrens. Dabei wird in zwei maßgebende Aspekte, Richtigkeit und Präzision, unterschieden. Die Richtigkeit bezieht sich auf den systematischen Fehler, dem in diesem Fall durch die verwendete Kalibrierung weitgehend entgegengewirkt wird. Die Präzision beschreibt die Messunsicherheit, die sich mit Hilfe der Schätztheorie methodisch analysieren lässt. Hierfür wird die Cramér-Rao-Schranke, das theoretische Minimum der Varianz, speziell für das FMCW-Verfahren hergeleitet. Zugrunde liegt die Annahme, dass es sich bei den Störungen im Messsignal um additives weißes gaußsches Rauschen handelt, welche durch Hypothesentests bekräftigt wurde. Die berechnete Schranke stellt den Zusammenhang zwischen der Varianz der Messung und dem Signal-Störleistungsabstand dar und wird mittels Simulationen und Messungen validiert. Die hohe Präzision und die Richtigkeit der Messergebnisse weisen das Potenzial des modellbasierten Ansatzes für einen zuverlässigen Einsatz in Messanwendungen nach.

Im Hinblick auf zeitliche Anforderungen im industriellen Kontext werden verschiedene Methoden für den Anpassungsprozess zwischen dem modellierten und dem gemessenen Signal verglichen. Zuerst wird die Exhaustionsmethode angewendet, die sämtliche potenzielle Modellsignale berechnet. Solange die Schrittweite klein genug gewählt wird, stellt die Methode sicher, dass das globale Optimum gefunden wird. Einer hohen Rechenzeit wird durch eine parallele Verarbeitung auf Grafikprozessoren entgegengewirkt. Zur vereinfachten Berechnung des Gütemaßes kann an Stelle der Korrelation direkt die Kostenfunktion, der euklidische Abstand zwischen beiden Signalen, berechnet werden. Die Simulation der Lösungsräume charakteristischer Messszenarien zeigte eine hohe Anzahl von lokalen, weitgehend äquidistanten Minima auf. Es wird gezeigt, dass genetische Algorithmen, ein stochastisches Verfahren, das zufällig gewählte Punkte im Lösungsraum miteinander kombiniert, ungenaue Dickenwerte ermitteln. Aufgrund dessen wird ein alternatives Optimierungsverfahren entworfen, das speziell für die hohe Anzahl lokaler Optima konzipiert ist. Für dieses wird im ersten Schritt der mittlere Abstand der Minima mittels Fourieräquivalenzen berechnet. Danach wird ein engeres Raster an äquidistanten Startpunkten initialisiert, um in den jeweils konvexen Teilumgebungen die nächstgelegenen Extremwerte mittels Gradientenverfahren bzw. dem Nelder-Mead Algorithmus anzunähern. Die erste Variante nutzt für jede Iteration die Richtung des negativen Gradienten, da diese den lokal steilsten Abstieg anzeigt. Da der jeweils konvexe Ausschnitt des Lösungsraums nicht verlassen werden soll, wird eine vergleichsweise kleine, heuristisch bestimmte konstante Schrittweite verwendet. Der Nelder-Mead Algorithmus basiert auf einem initialen Simplex im Lösungsraum, dessen Eckpunkt mit dem höchsten Kostenfunktionswert iterativ durch einen Neuen mit niedrigerem Wert ersetzt wird, welcher sich aus den vorherigen Ecken ergibt. Beide Varianten identifizieren mit einer signifikanten Reduktion der Rechenkomplexität sowohl die meisten lokalen als auch das globale Minimum. Insbesondere der Nelder-Mead Algorithmus stellt aufgrund der Richtigkeit und Präzision der Ergebnisse eine effiziente Alternative zur Exhaustionsmethode dar.

Das Potenzial des modellbasierten Ansatzes für Anwendungen im Bereich des zerstörungsfreien Testens wird anhand industrieller Proben dargelegt. Dazu zäh-

len dreischichtige Rohre mit einem Rezyklatschaumkern. Vergleichsmessungen mit dem technisch und zeitlich aufwendigen Terahertz-Zeitbereichsspektroskopieverfahren validieren die gemessenen Ergebnisse. Eine weitere Messreihe an Polyesterfolien zeigt, dass Dicken bis $121\ \mu\text{m}$ (6 % der Rayleigh-Auflösungsgrenze) mit Abweichungen kleiner als 4 % bestimmt werden können.

Für das im Rahmen der Untersuchungen erarbeitete modellbasierte Verfahren wurden methodische Aspekte und Messergebnisse veröffentlicht. Zu den wesentlichen wissenschaftlichen Beiträgen zählen die folgenden Punkte:

- Abschätzung der Präzision: Im Gegensatz zu vorherigen Arbeiten wird bei der Herleitung der Cramér-Rao-Schranke die Abhängigkeit der Nullphase und der Frequenz der verschiedenen Schwingungen des FMCW-Messsignals berücksichtigt. Die Schranke stellt die Abhängigkeit der Präzision vom Signal-Störleistungsabstand des Messsystems, den Brechungsindizes der Materialien und weiteren Parameter der Messung dar.
- Effiziente Berechnung der Mehrfachreflexionen: Die Modifikation der Transfermatrixmethode ermöglicht die vollständige Betrachtung der Mehrfachreflexionen unter der vereinfachten Annahme von homogenen, linearen und dispersionsfreien Materialien, indem anstelle der Wellenausbreitung lediglich deren Auswirkungen auf das Messsignal berechnet werden. Die Anpassungen basieren darauf, dass sich eine Amplitudenänderung der elektromagnetischen Welle in gleicher Weise auf die Signalstärke auswirkt, und, dass sich Frequenz und Nullphase des Signalanteils linear zu einer längeren Ausbreitung im Material verschieben. Für den gegebenen Fall reduziert sich der Rechenaufwand auf einen Bruchteil von dem der klassischen Variante.
- Angepasstes Optimierungsverfahren: Eine spezielle Methode wird erstellt, die auf der äquidistanten Charakteristik des Lösungsraums basiert. Durch eine Kombination der Abschätzung des mittleren Abstands der Minima, einem Raster aus entsprechenden Initialpunkten und der Verwendung des Nelder-Mead Algorithmus zur Näherung des nächstgelegenen Minimums, kann das globale Optimum sowohl richtig als auch präzise ermittelt werden.

Abstract

The nondestructive testing of multilayered materials is increasingly applied in both scientific and industrial fields. In particular, developments in millimeter wave and terahertz technology open up novel measurement applications, which benefit from the nonionizing properties of this frequency range. One example is the noncontact inspection of layer thicknesses. Frequently used measuring and analysis methods lead to a resolution limit that is determined by the bandwidth of the setup. This thesis analyzes the reliable evaluation of thinner layer thicknesses using model-based signal processing.

In context of this work, the electromagnetic radiation is generated conforming the frequency-modulated continuous-wave (FMCW) approach. For this purpose, the samples-under-test are illuminated by waves, whose frequencies are linearly increased. Hence, their frequency-specific response is captured. Boundary surfaces between layers of different refractive indices cause characteristic reflections. Each of them corresponds to one superposed oscillation in the measured signal, whose frequency is determined by the propagation time of the wave. The measurement data is calibrated in order to compensate for spurious interfering echos such as reflections from the measurement system. If the adapted frequency portions of the signal are accurately determined, the thicknesses of the material layers can be calculated. For such a frequency analysis, the discrete Fourier transform is often applied. Then, a single oscillation is represented by a broad peak, whose center corresponds to the requested frequency. Additionally, side lobes are present in its approximation. The measurement duration or rather the bandwidth of the frequency modulation determine the width of these spectral portions. The distance between the maximum and the closest zero is referred to as the Rayleigh resolution limit. Layer thicknesses below this value cannot be determined solely by applying the Fourier transform, since their main peaks overlap. In this work, alternative signal-processing methods are analyzed, which are not restricted by the Rayleigh limit. For this purpose, on the one hand, spectral estimation algorithms are applied. On the other hand, the measured signal is replicated by an alternative model-based approach.

Spectral estimation algorithms are based on models to approach the power spectral density of the measured signal. For this, few parameters have to be determined. The total number of significant oscillations influences the quantity of required parameters, which is referred to as model order. Two specific algorithms are chosen to investigate the reliability of spectral estimation for FMCW thickness

analysis: modified covariance method and MUSIC (*multiple signal classification*) algorithm. The modified covariance method is based on the model, that portions of the measurement signal can be estimated using previous data points. Accordingly, a filter can be designed which models this property and enables to estimate certain characteristics of the power spectral density. Applying system theory, the number of exponential functions of the measured signal results in the model order, the quantity of poles of the filter. Evaluating the positions of these poles, the frequency portions can be estimated. For MUSIC algorithm, the measured signal is expected to consist of complex exponential functions in additive white Gaussian noise. Due to the inherent orthogonality between both portions, noise eigenvectors can be calculated based on an eigenvalue decomposition. These vectors determine the coefficients of a filter, whose inverse enables estimating the power spectral density and the frequency portions. It can be shown by simulations that the thickness resolution can be extended to thinner layers. Moreover, side lobes cannot be observed for the resulting (pseudo) power spectra. However, the calibration and the comparatively low signal-to-noise power ratio influence the model order for both methods. Therefore, inaccurate frequency portions and deviating layer thicknesses can be observed.

Applying an alternative model-based approach, the evaluation of inaccurate frequency portions can be reduced. For this purpose, a model, which corresponds to the mathematical description of the expected measurement signal, is generated and adapted to it. The conformity between both is quantified by the correlation in the first place. The parameters of the best fit indicate an appropriate approximation of the thicknesses. A priori estimates of the different layer gauges enable to correspondingly delimit the search intervals. The expected measurement signal is characterized by main reflections, which are the first beam or signal portions caused by the different boundary surfaces. Additional multiple reflections can be observed as well. It can be shown that their influence is significant either, when the contrasts between the refractive indices of adjacent materials are high, or, when the layered structure is attached on a conductive substrate. To efficiently calculate multiple reflections, a transfer matrix method is modified. It remodels the individual layers as quadrupoles and the wave propagation as matrix multiplications. For the modification, instead of the entire wave propagation, solely its effects on the measurement signal are calculated. The evaluation of measured data validates the method and the ability of the model-based approach to determine layers below the Rayleigh resolution limit.

Besides the resolution, the accuracy and the precision of the results are significant criteria for the reliability of a measurement system and evaluation process. The accuracy relates to the systematic error, which in this case is largely counteracted by the calibration. The precision instead classifies the measurement uncertainty. It is analyzed theoretically by applying estimation theory. For this purpose, the Cramér-Rao lower bound, which approximates the minimum variance for unbiased estimators, is derived. It is assumed that the signal is interfered with additive white Gaussian noise, which is indicated by hypothesis tests. The calculated bound represents the relation between variance of the results and the

signal-to-noise power ratio. It is validated by simulations and measurements or representative examples. High accuracies and precisions of the results demonstrated the potential of the model-based approach for a reliable use in measurement applications.

With regard to potential real-time requirements in industrial production lines, different optimization methods for the fit process between the modeled and the measured signal are compared. Firstly, exhaustive search is applied, which requires the calculation of all potential modeled signals within the search intervals. As long as the step size is chosen as small enough, the method ensures that the global optimum is found. The high computation time is counteracted by parallel computing on graphics processors. To simplify the calculation of the correlation between modeled and measured signals, the cost function, the Euclidean distance between both, can be determined. Simulating solution spaces of representative measurement scenarios invariably shows a high number of local, rather equidistant minima. It is demonstrated that genetic algorithms, a stochastic procedure that combines randomly selected points in the solution space, frequently achieves imprecise thickness values for such spaces. An alternative optimization method is established for FMCW considering the high number of local optima. Firstly, the mean distance between the minima is calculated using Fourier equivalences. Afterwards, a set of narrower initial points is generated in order to approximate the closest extreme values in the respective convex section of the space. For this step, the gradient method or the Nelder-Mead algorithm are applied. For each iteration, the first variant shifts the points towards the direction of the locally steepest descent indicated by the negative gradient. Since the respective convex section should not be exceeded, a comparatively small, heuristically determined step size is used. Nelder-Mead algorithm is based on initial points in the solution space arranging a simplex. Iteratively, the vertex with the highest cost function value is replaced by a point with a lower value. Both variants identified the global and almost all local minima determined by the exhaustive search. However, the computation load and time is significantly reduced. Particularly, Nelder-Mead variant is an efficient alternative due to the high accuracy and precision of the results.

Different measurement results indicate the potential for industrial applications. Multilayered tube wall sections characterized by a recycle foam core are exemplary analyzed and the results validated by comparing terahertz time-domain spectroscopy measurements. The minimum measurable thickness is determined for biaxially-oriented polyethylene terephthalate sheets resulting in value of 121 μm corresponding to 6 % of the Rayleigh limit with a bias of less than 4 %. In terms of future application, the bandwidth is reduced to outline the potential of the signal-processing approach for compact systems such as monolithic microwave integrated circuit.

While model-based approaches have been used for numerous previous applications, different aspects of the thickness evaluation show a significant degree of novelty, which is discussed in the following.

- Estimation of precision: in contrast to former work, the Cramér-Rao lower

bound is derived with a special consideration on the dependency of frequencies and zero phases of the signal's oscillations. Since both quantities are simultaneously processed in case of the model-based approach, this characteristic is significant. The bound represents the dependency of the measurement uncertainty on the signal-to-noise ratio, material characteristics, and setup parameters.

- Efficient calculation of multiple reflections: the modification of the transfer matrix method particularly for FMCW computes multiple reflections for linear, homogeneous, isotopic, and dispersion-free materials by observing the influence of the wave propagation directly on the measured signal. It is based on the linear amplitude relation of reflections and signal portions as well as a frequency, and zero phase shift in case of varying the optical path length. For the presented case, instead of millions, solely thousands data points are required.
- Optimization process: based on the equidistant characteristic of the solution space with numerous local optima, an optimization strategy is customized for FMCW thickness measurements. Utilizing Fourier transform equivalences, the average distance between adjacent minima is derived. A set of equidistant initial points is then initialized to approach the closest optimum, respectively. For the presented examples, the evaluated thicknesses are almost as accurate and precise as exhaustive search, while the computation load and time is significantly reduced.

Contents

1	Introduction	1
1.1	Thickness Measurements Using Millimeter and Terahertz Waves	2
1.2	Requirements for Applications	3
1.3	Aspects of Novelty	4
1.4	Structure	5
2	Distance and Thickness Measurements	7
2.1	Frequency-Modulated Continuous-Wave Approach	8
2.2	Frequency-Modulated Continuous-Wave Setup	10
2.3	Lateral Resolution	11
2.4	Preprocessing	13
2.5	Depth Resolution	17
3	Spectrum Estimation	21
3.1	Parametric Estimation	22
3.2	Subspace Method	24
3.3	Model Order	25
3.4	Influence of Additive White Gaussian Noise	27
4	Model-Based Signal Processing	31
4.1	Model-Based Approach	32
4.2	Influence of Multiple Reflections	33
4.2.1	Single Layers	34
4.2.2	Multilayers	35
4.3	Modified Transfer Matrix Method	36
4.4	Validation of Model-Based Approach	39
4.5	Comparison of Algorithms	40
5	Accuracy and Precision	43
5.1	Influences of Components and Processing	44
5.2	Influence of Phase Noise	46
5.3	Analysis of Resulting Signal Noise	48
5.3.1	Ensemble Characteristic	49
5.3.2	Sample Function Characteristic	51
5.4	Limitation of Precision	52
5.4.1	Distance Measurements	53

5.4.2	Thickness Measurements	54
5.5	Precision of Simulations and Measurements	57
5.5.1	Distance Measurements	57
5.5.2	Thickness Measurements	59
6	Optimization	63
6.1	Cost Functions	64
6.2	Influences on Solution Space	68
6.3	Optimization Algorithms	70
6.3.1	Gradient Descent	71
6.3.2	Nelder-Mead Algorithm	74
6.3.3	Genetic Algorithm	77
6.4	Comparison of Algorithms	79
6.4.1	Validation of Algorithms	79
6.4.2	Computation Time, Precision, and Accuracy	80
6.4.3	Measurement Results	82
6.4.4	Multilayers	83
6.4.5	Discussion of Algorithms	84
7	Applications	87
7.1	Measurement Setup	87
7.2	Measurement Results	89
7.2.1	Tube Wall Inspection	89
7.2.2	Stepped Tube Wall Section	92
7.2.3	Minimum Thickness	93
7.2.4	Towards Lower Bandwidths	95
8	Summary and Outlook	99
	List of Abbreviations	103
	List of Variables, Symbols, and Operators	105
	List of Figures	109
	List of Tables	111
	List of Publications	113
	Bibliography	119

1. Introduction

On the one hand, the functionality and safety of different industrial products can only be guaranteed by achieving certain minimum layer thicknesses. On the other hand, material resources can be saved if the layers are simultaneously chosen as thin as possible. Therefore, thickness measurements are essential for nondestructive testing. The aim of this work is to determine multilayers without requiring contact between sensor and object using millimeter and terahertz waves, which resulted in a significant amount of publications [1]–[22]. Several alternative thickness measurement systems are already commercially available such as mechanical, ultrasonic, and X-ray approaches. In the following, an overview of established techniques and their requirements is given.

Mechanical measurement systems such as millimeter gauges are often cost-efficient. However, they are based on a direct contact between sensor and sample-under-test (SUT). The mechanical tension between both can affect the accuracy of the results. Depending on the choice of the measurement spot, the SUT even has to be removed (which is usually quite cost-intensive such as for tubes in service [23]) or to be destroyed (for instance cut into smaller sections). For single layers, alternative approaches are eddy current and capacitive techniques. Eddy current-based sensors enable determining single conductive layers [24], [25] and dielectric coatings [26] but they still are contact-based. Capacitive sensors have to be large in comparison to the measured object, because otherwise, the dependency of the thickness on the capacity is nonlinear and biased results may be obtained. Thus, both methods are not practical in certain scenarios.

All of the following techniques are based on measuring the propagation time of electromagnetic or acoustic waves. The boundary surfaces of the SUT generate characteristic reflections. Propagation time differences result in distinctive time, phase or frequency shifts, which are processed to evaluate the thicknesses.

Optical methods such as interferometry [27] enable highly accurate thickness evaluations due to the low wavelength of the electromagnetic waves. Nevertheless, since many materials are opaque for the visible spectrum, not any information of the internal structures may be detected. Instead of the single thicknesses of the different layers, solely the width of the entire SUT can then be determined. Even thinner layers are resolvable by X-ray techniques, because of the reduced wavelength and transparency of respective materials. However, because of the low wavelength and high photon energy, the radiation is ionizing. Therefore, a high effort for shielding can be required in case the production lines have to be accessible for humans.

In terms of ultrasound techniques, one approach for the design of setups and systems is based on generating and detecting pulses [28]. The time differences between the different reflections indicate the thicknesses. For thinner pulse widths, the minimum measurable thickness is lower. Such short pulses correspond to broad amplitude spectra in the frequency range. A continuous-wave radiation with a linearly increasing frequency is characterized by a broad spectrum and therefore enables thickness determination as well. This approach is referred to as frequency-modulated continuous-wave (FMCW). The measurement signal however corresponds to a sum of oscillations, whose frequencies and zero phases are shifted according to the propagation times of the beam portions.

Usually, ultrasonic techniques are applied for thicknesses in the order of the corresponding wavelengths. Using signal processing, thinner multilayers can be processed such as by deconvolution [29] or by fitting a signal model to the measured data and utilizing the model's parameter as an appropriate estimate of the requested thicknesses. The model itself for instance corresponds to a sum of Gaussian wavelets [28]. Based on resonance models characteristics [30], even the thickness of thin fluids can be determined. However, ultrasound systems provide moderate measurement rates of roughly 5 Hz–250 Hz [31] due to the low acoustic propagation velocity [32]. Moreover, ultrasonic systems usually benefit from coupling between sensor and SUT. Despite developments of novel noncontact sensors [33], the propagation velocity of the acoustic waves is highly influenced by the temperature [34]. In industrial environments, temperature fluctuation cannot be prevented which may affect the accuracy of the results.

1.1 Thickness Measurements Using Millimeter and Terahertz Waves

In comparison to optical and X-ray frequency ranges, the electromagnetic spectrum from several gigahertz to few terahertz is both nonionizing and transparent for many dielectric materials. Within the terahertz frequency region from 100 GHz to 10 THz [35], setups and measurement systems are often designed according to the time-domain spectroscopy (TDS) approach [36]. It is based on electromagnetic pulses [3] which are generated using a photoconductive antenna [37]. For multilayered samples-under-test, the propagation times of the reflections by the different boundary surfaces indicates the thicknesses of the single layers. In case the time delay of two reflections is shorter than the pulse width, signal-processing techniques allow an accurate resolution. Similar to ultrasonic approaches, potential methods are the comparison of measured data with modeled signals [4], [38] or deconvolution [39]. In [40] instead, the data is extrapolated by calculating novel points based on the given set. Based on the model approach, layers down to approximately 6 μm [38] in case of car paints are determined. However, due to the stronger attenuation of the higher frequency portions, the penetration depth of the pulses is restricted depending on the material.

In [41], a continuous-wave approach is presented using lower frequencies of ap-

proximately 10 GHz: a multilayer SUT is illuminated by an electromagnetic waves with constant frequencies. The signal of the transient time, the delay until reflections by all boundary surfaces attain the receiver, can be processed to achieve the single thicknesses. For both, this continuous-wave approach and for TDS, the required sampling frequency is higher than the one of available detectors. Therefore, the radiation is sub-sampled requiring one pulse or transition per data point. Resulting measurement rates are rather low such as 100 Hz for TDS [42]. The frequency range 30 GHz–300 GHz is referred to as millimeter waves [43]. Within the spectrum of their applications, different approaches are adapted for distance and thickness measurements. For instance, continuous-wave interferometric radar configurations of multiple ports support testing conducting sheet thicknesses [44] by ranging distances from two opposite sides of the SUT. For vector network analysis [45], the frequency of the radiation is increased stepwise, to sample the respective frequency response of the SUT. For a priori given thicknesses [46]–[48], the material parameters can be determined. Inversely, with information of the refractive indices, thicknesses could be evaluated as well. However, since the frequency is stepped slowly, rather lower measurement rates are achievable depending on the number of steps and the bandwidth.

Utilizing the FMCW approach allows for rates up to kilohertz. Different thickness measurement applications have already been investigated based on it: in [49], the frequency band of 1 – 2 GHz is applied for measuring layers within coal mines and to detect anomalies. The measurement of snow thickness is presented in [50] using roughly 8 – 12 GHz. For millimeter wave application, the thickness of steel strips has been evaluated by two separate distance measurements detecting the face and back of the sheet [51], respectively. However, the resolution is restricted for FMCW: in case the frequency analysis of the measured oscillations is performed by the Fourier transform, one reflection results in a main peak with side lobes. The width of a single peak restrict the ability to separate it from a second one. The aim of this work is to analyze alternative model-based signal-processing techniques to expand for thin layer resulting in interfering peaks.

1.2 Requirements for Applications

Utilizing the FMCW approach enables novel application scenarios for nondestructive thickness testing. One promising example is the inspection of multilayered polyvinyl chloride tube walls. Due to the attenuation of the higher frequency portions, the penetration depth is restricted for TDS. Thus, solely thinner walls can be determined. Some tube configurations also exhibit recycle foam cores, which may affect the signal quality and hence accuracy of ultrasound measurements. In contrast, FMCW W band transceivers provide high penetration depths for polyvinyl chloride, other kinds of plastics, glass or ceramics. However, the resolution is affected: since frequency multiplication is utilized to generate the radiation, addressing a rather low frequency range (such as W band) results in a reduced bandwidth. The width of the peaks however increases. The ability to separate reflections and to determine their center frequencies, which indicate the

quested thicknesses, is affected.

Since the aim of this work is to expand for layers below this restriction by the peak width, novel layer compositions such as thin layers hidden behind thick structures could be addressed. Besides the resolution, repeatability as well as unbiased results are required for reliable testing. For that purpose, all error sources of respective setups should be identified and sufficiently compensated. On the one hand, the fast measurement rates of FMCW systems may be an important step towards real-time requirements of production processes. On the other hand, the computational load of advanced model-based signal-processing approaches could not instantly fulfill this demand. Therefore, the potential of promising optimization processes should be exploited.

1.3 Aspects of Novelty

Similar to ultrasound [28] and TDS [38] applications, the replication of the measured signal with modeled versions results in estimation of parameters, that corresponds in accurate thicknesses below the resolution restrictions. However, novel procedures and characteristics are introduced, discussed, and validated in [1]–[22]. The most significant aspects are summarized.

- Optimization method based on equidistant characteristic of solution space: the Euclidean distance between a measured and a modeled signal corresponds to the cost function, which has to be minimized for the model-based approach. The corresponding solution space is observed to be characterized by numerous equidistant minima. A procedure is presented in [7] which significantly reduces the calculation time in comparison to exhaustive search: the average distance of the optima is calculated as a function of setup parameters utilizing Fourier transform equivalences. Afterwards, an equidistant set of initial points approaches the respectively closest minima using a classical optimization method such as Nelder-Mead algorithm. Accuracy and precision of the results are similar to exhaustive search. The procedure is validated by measurements.
- Modification of the transfer matrix method to efficiently calculate multiple reflections: for an accurate signal model, the entire sum of reflections has to be integrated. The complete wave propagation within multilayer materials can be described by a transfer matrix method. However, a modification of it [1], [9] further reduces the computation load by solely observing the effects on the measured signal. Instead of millions, the number of required data samples reduces to few thousands for the W band setup.
- Analysis of the precision for reliable results: an important quantity for analyzing the quality of determined thicknesses is the precision or rather the

measurement uncertainty. Estimation theory enables the calculation of the theoretical minimum variance, referred to as Cramér-Rao lower bound. The limitation is derived in [6] under special consideration of the dependency of frequency and zero phase of the FMCW signal's oscillations. The applied assumption of additive white Gaussian noise is indicated by hypotheses tests.

Additionally, the results of the model-based approach are compared with the one of spectral estimation algorithms in [2]. Besides static single sensors, other setup configuration such as for imaging [12] and a handheld device [4], [19] were presented.

1.4 Structure

This thesis is organized in 7 chapters. In the following one, the FMCW approach is presented. A focusing setup configuration is introduced resulting in a restricted lateral resolution, which is estimated as the width of the beam. A calibration procedure is discussed, which removes spurious echos from the measured signals. In case the Fourier transform is performed to determine the thicknesses, the resolution is restricted by the peak width. This characteristic is described, e.g., by introducing the Rayleigh limit, the distance between maximum and the first zero of one peak.

Chapter 3 presents spectral estimation approaches, which are tested to resolve layers below the Rayleigh limit. For this purpose, the algorithms utilize models of the measured signal such as expecting oscillations in additive noise. The influence of the calibration on the model order, which usually depends on the number of significant reflections, is discussed. Two variants of spectral estimation algorithms are chosen, modified covariance method and MUSIC (multiple signal classification) algorithm. They are tested using simulated signals for which the noise of the setup is estimated.

The following chapter presents a model-based approach, which fits models resulting from a priori given estimates of the thicknesses to the measured signal. By maximizing the correlation coefficient, layers below the previous limit can be evaluated, since the parameters of the best fit indicate the requested thicknesses. The influence of multiple reflections is discussed. A modification of the transfer matrix method is presented to calculate their effects on the measurement signal, efficiently. Measured data validates the approach. The presented signal-processing approaches are compared and discussed.

Chapter 5 addresses the influences on bias and repeatability of the results. The theoretical minimum of the variance, referred to as Cramér-Rao lower bound, is derived taking special consideration on the dependency of frequency and zero phase of each oscillation within the measured signal. The calculated limit is validated by simulation and measurements.

Since the fitting process of the modeled signals comes with a high computation load in case of an exhaustive search, alternative techniques are discussed. Nu-

merous local optima of the solution space require a modification of classical optimization algorithms. For this purpose, the average distance between the optima is theoretically derived. A set of equidistant initial values enables approaching the closest optima, respectively. The procedure is tested for validation using simulated and measured signals.

The following chapter analyzes the potential for future applications. The novel resolution limit is determined exemplarily for single-layered biaxially-oriented polyethylene terephthalate sheets. Thickness determinations on industrial tube sections validate the model-based approach. Finally, the potential for future setups based on compact transceivers such as monolithic microwave integrated circuits is presented. Such sensors are usually characterized by a reduced bandwidth and the signals are virtually adapted to this condition by reducing their lengths.

In this work, the term simulation describes numerical calculations of physical processes, of which the parameters are partially or completely given. For simplicity, abbreviations are introduced in each chapter.

2. Distance and Thickness Measurements

For both distance and thickness measurements using electromagnetic waves, the samples-under-test are illuminated. At each boundary surface, the radiation is separated into reflected and transmitted portions. A sum of such beams is detected by the setup. Their propagation time differences indicate the thicknesses of the single layers. For interferometry using a single frequency continuous wave, the propagation time is indicated by a phase shift. However, the ambiguity range is small, e.g., 1.5 mm for 100 GHz, since it equals half of the wavelength. In case of pulsed radiation, the time delay of the pulses are processed. One of these short pulses corresponds to a broad spectrum in the frequency domain. A similar spectrum can be generated by a continuous wave, whose frequency is increased linearly over time. This approach is referred to as frequency-modulated continuous-wave approach (FMCW) [52]. By a frequency-specific analysis of the samples-under-test, distances and thicknesses can hence be measured.

For terahertz application, the pulse-based time-domain spectroscopy is widely used for thickness measurements. Corresponding technically complex setups offer bandwidths of roughly up to 6 THz [42]. Dispersion may affect the accuracy of the results and can be implemented in the signal processing. The FMCW approach is chosen in this work. Setups operating in the W band provide higher penetration depths such as in plastics. Due to typically smaller bandwidth such as 40 GHz, the influence of dispersion is inherently reduced. The FMCW technique has already been applied for precise ranging [53]–[56]. The measurement signal corresponds to a sum of oscillations, whose frequencies are determined by the propagation times of the beam portions. Usually, a Fourier transform is performed for evaluating the frequency portions and hence thicknesses. However, for multitargets, inaccurate results can be observed [57] due to the superposition of frequency peaks. The aim of this chapter is to systematically analyze the limitations of the Fourier transform-based evaluation in case of thickness measurements.

In the following, the FMCW approach is introduced. For each measurement, a sum of oscillations is detected, whose frequency portions indicate the propagation times. Based on this approach, a measurement setup operating in reflection mode is presented, whose sampling frequency determines the ambiguity range. To focus the beam into the samples-under test, optics are included. The corresponding lateral resolution, which depends on the width of the beam, is estimated. To

reduce reflections by the surroundings of the setup, a calibration is discussed next. Finally, the resulting depth resolution is analyzed. Due to the superposition of different frequency peaks, the ability to separate them is restricted. The Rayleigh criterion, which is a common quantity to describe this limitation, is introduced and discussed.

2.1 Frequency-Modulated Continuous-Wave Approach

The FMCW approach is based on the schematic of uniform plane waves. The electromagnetic wave equations resulting from Maxwell's equations describe the propagation through source-free unbound free-space media. For FMCW, the frequency f of a wave is modulated linearly over time t and radiates a sample-under-test (SUT). The oscillation can be described by the equation,

$$s_t(t) = \Re\{\underline{s}_t(t)\}, \quad (2.1)$$

with the operator $\Re\{\cdot\}$, which evaluates the real part of the complex representation

$$\underline{s}_t(t) = \exp\left(j2\pi F_1 t + j\pi \frac{B}{T} t^2\right), \quad (2.2)$$

with start frequency F_1 , modulation bandwidth B , measurement duration T , and imaginary unit j . In this work, all equations and quantities conform to the International System of Units (SI) [58]. The underscore $\underline{\cdot}$ indicates that the signal or quantity is complex.

As depicted in Figure 2.1 *left*, the radiation propagates through the layers. At each boundary surface of materials with different complex refractive indices $\underline{\eta}_0$, $\underline{\eta}_1$, and $\underline{\eta}_2$, it is separated into a reflected and transmitted portion. The first reflections of the respective boundary surfaces are referred to as main and the remaining ones as multiple reflections. The angle of incident is usually chosen as approximately normal, but tilted for this schematic.

The complex refractive index of an isotropic homogeneous medium,

$$\underline{\eta} = \eta + j \cdot \kappa, \quad (2.3)$$

with real η and imaginary part κ determines the degree of reflection and transmission of the wave: the Fresnel equations enable calculating the amplitude ratio for each separation at boundary surfaces. The reflection coefficient \underline{r}_{01} at normal incidence results in

$$\underline{r}_{01} = \frac{-\underline{\eta}_1 + \underline{\eta}_0}{\underline{\eta}_1 + \underline{\eta}_0}. \quad (2.4)$$

The transmission coefficient \underline{t}_{01} equals

$$\underline{t}_{01} = \frac{2 \cdot \underline{\eta}_0}{\underline{\eta}_1 + \underline{\eta}_0}. \quad (2.5)$$

For the W band, the real part of the refractive indices is usually significantly larger than the imaginary value for characteristic materials-under-test such as plastics. Hence, the coefficients are typically approaching real values. Within one layer, amplitudes of the beams are reduced due to attenuation caused by absorption, scattering etc. With the extinction coefficient κ , the loss or the amplitude reduction can be described by $\exp\{-\kappa d \frac{2\pi f}{c_0}\}$ [59], with the depth d , and vacuum speed of light c_0 .

In case of reflection mode, the optical path is passed twice. The antenna receives the signal $s_r(t)$ corresponding to a sum of reflected and propagation time τ_l -delayed portions of the oscillations

$$s_r(t) = \Re\{\underline{s}_r(t)\} = \Re\left\{\sum_l a_l \underline{s}_t(t - \tau_l)\right\} \quad (2.6)$$

for the l^{th} of L significant reflection with the resulting (approximately real) amplitude a_l . The signals $s_r(t)$ and $s_t(t)$ are mixed to transfer the information into the intermediate frequency range, which is more convenient to measure. The complex representation of the output equals

$$\underline{s}_{IF}(t) = \underline{s}_t(t) \cdot \underline{s}_r^*(t). \quad (2.7)$$

The operator (*) denotes complex conjugate. The real discretized measurement signal results in

$$s_{IF}[n] = \sum_l a_l \cos\left(2\pi f_{b,l} \frac{n}{f_s} + \phi_{\tau_l}\right) \quad (2.8)$$

with sampling frequency f_s , digital index of time $n \in \{0, 1, \dots, N - 1\}$, and the number of samples N . The beat frequency $f_{b,l} = \frac{B}{T} \tau_l$ and the zero phase $\phi_{\tau_l} = 2\pi \cdot \left(F_1 - \frac{1}{2} \frac{B}{T} \tau_l\right) \cdot \tau_l \approx 2\pi F_1 \tau_l$ are functions of τ_l .

In Figure 2.1 *right*, the relation of FMCW quantities for a single reflection Rx is schematically depicted. Tx denotes the transmitted signal characteristics. In case of an ideal linear rise, the frequency difference between both, f_b , is a constant value.

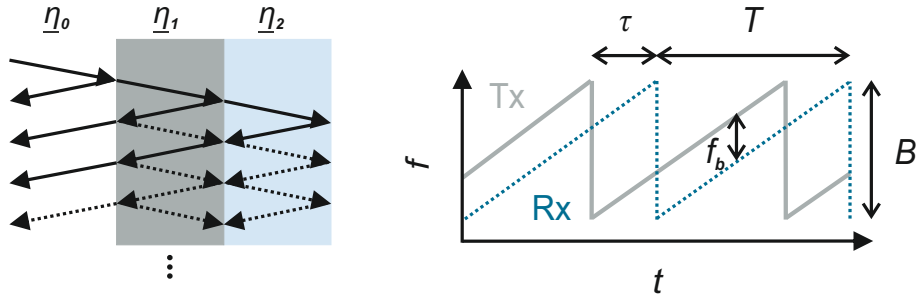


Figure 2.1: *left:* schematic of multilayered SUT of different refractive indices, main (solid) and multiple (dotted) reflections, *right:* relation of FMCW quantities for one reflector

The time delay τ and hence the beat frequency enable determining the optical

path length. Considering the refractive indices, distances and thicknesses can be evaluated.

2.2 Frequency-Modulated Continuous-Wave Setup

Based on the FMCW approach, a setup is designed for distance and thickness measurements. Figure 2.2 shows its schematic. To generate a linearly frequency-modulated oscillation, a voltage-controlled oscillator is driven by the data acquisition unit of a computer. Ideally, it transfers an increasing input voltage into an oscillation whose frequency linearly rises over time. To compensate for a non-linear rise, the input is counteractively pre-distorted [60]. The oscillation has a center frequency of 15 GHz (K_u band) and a bandwidth of 6 GHz. It is frequency-multiplied afterwards into the radio frequency range of roughly 70 – 110 GHz.

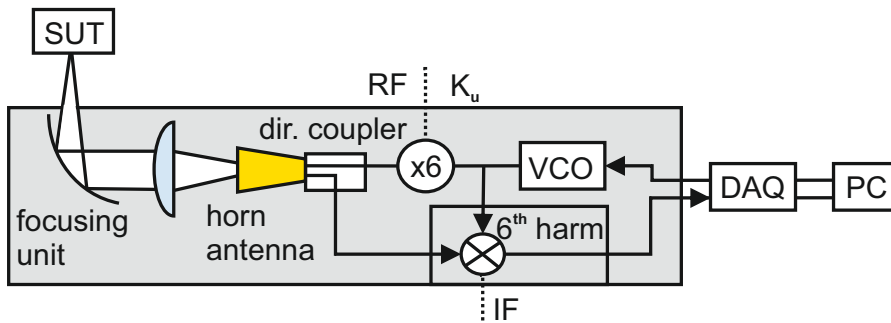


Figure 2.2: Schematic of an FMCW setup including a focusing unit, radio frequency (RF), directional coupler (dir. coupler), frequency multiplier (x6), voltage-controlled oscillator (VCO), data acquisition unit (DAQ), computer (PC), 6th harmonic mixer (6th harm), intermediate frequency (IF)

A directional coupler divides the paths of the emitted and received signal. It guides the multiplied output to a conical Pickett-Potter antenna. This variant of a horn emitter is characterized by a high symmetry of electric and magnetic field plane pattern and a low side lobe level [61].

Due to a rectangular waveguide, the radiation is linearly polarized. The beam is collimated by a lens and focused by an off-axis parabolic mirror into the center of the SUT. The received reflection is mixed with the 6th harmonic of the currently emitted oscillation. The intermediate frequency portion is analog-to-digital converted by the data acquisition with a sampling frequency of $f_s = 10$ MHz. To avoid ambiguity with regard to distance measurements, the Nyquist theorem

$$f_b < \frac{f_s}{2} \quad (2.9)$$

has to be fulfilled. The term $f_s/2$ is referred to as Nyquist frequency. The corresponding distance

$$d_N = \frac{c_0 T f_s}{4B} \quad (2.10)$$

describes the ambiguity range $2d_N$ in air. For the presented setup parameters and $T = 170 \mu\text{s}$, $d_N = 3.19 \text{ m}$ is many orders larger than the focus length of the parabolic mirror of 7.5 cm . Therefore, potential reflections from distant regions are blurred and attenuated.

In comparison, for utilizing a single constant frequency, the ambiguity range equals half of the wavelength and hence less than few millimeters. However, the thickness of many samples-under-tests is larger. For TDS, the scanning range is modifiable because it is determined by the delay unit of the system. For instance in [42], it equals $3,200 \text{ ps}$ or rather 96 cm in air. Nevertheless, in case of larger scanning ranges, the size of the system and the duration of the measurement increases. The FMCW method inherently provides a high ambiguity range, which however can only be fully exploited when using a collimating setup.

2.3 Lateral Resolution

For thickness measurements, the depth resolution is an important quantity, because it describes the minimum thickness that can be evaluated. For simplicity, it is assumed that the width of the measurement spot approaches the value zero. However, this ideal cannot be achieved. Nevertheless, in case the SUT layers are plane-parallel in approximation within the illuminated area, the point reflector model serves as an appropriate approximation. Therefore, the lateral resolution is a significant value, and discussed in this section.

For simplicity, the beam is assumed to be Gaussian such as in Figure 2.3. Its symmetric intensity $\iota(d, r)$ decreases perpendicular to the optical axis corresponding to a Gaussian bell shape [59]:

$$\iota(d, r) = \iota(d, 0) \cdot \exp\left(-2\frac{r^2}{w(d)^2}\right) \quad (2.11)$$

with the on-axis intensity $\iota(d, 0)$, radius $w(d)$, and radial distance from the center axis r . For $r = w(d)$, the intensity is decreased to $\iota(d, 0)/e^2 \approx 0.14\iota(d, 0)$. The thinnest section of the focused Gaussian beam is the waist with radius w_0 .

At the waist, the wave front is assumed to be plane in approximation due to a larger distance between the SUT and the components as well as the utilization of a focusing unit. The radius $w(d)$ for all distances can be described by

$$w(d) = w_0 \left[1 + \left(\frac{\lambda d}{\pi w_0^2} \right)^2 \right]^{\frac{1}{2}} \quad (2.12)$$

with wavelength λ . The waist w_0 is estimated using the parameters of the parabolic mirror of 2 inch (5.08 cm) diameter and a focal length of $\theta = 7.5 \text{ cm}$.

The radius can be approximated as

$$w(d) \approx \frac{\lambda d}{\pi w_0} \quad (2.13)$$

for a larger d . The equation indicates that for a lower frequency band, the lateral resolution limit increases. Significant estimates of w_0 are depicted in Table 2.1 representing the variations of the beam width during the frequency modulation: the upper width limit varies from 3.97 mm to 2.55 mm.

A practical quantity for applications is the Rayleigh length, the distance for which the cross section doubles in comparison to the beam waist:

$$d_R = \frac{\pi w_0^2}{\lambda}. \quad (2.14)$$

To achieve the highest lateral solution, the SUT is positioned in the focus, and its extensions are not exceeding the Rayleigh length.

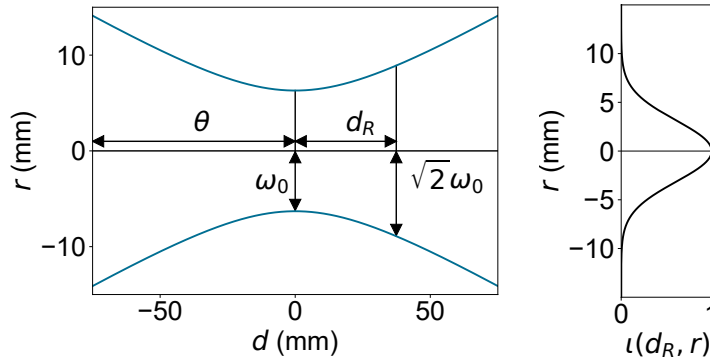


Figure 2.3: Schematic of focused Gaussian beam *left*: radius $w(d)$ (blue) as function of distance, *right*: transverse intensity profile at Rayleigh length d_R

Table 2.1: Estimated Upper Limit of Rayleigh Length d_R and Beam Waist w_0 for the W Band Transceiver

frequency	upper limit w_0	upper limit d_R
71.1 GHz	3.97 mm	11.71 mm
90.9 GHz	3.10 mm	9.16 mm
110.6 GHz	2.55 mm	7.53 mm

Figure 2.4 depicts a schematic of two different reflector surfaces. The three arrows represent the on-axis beam and two off-axis ones. They illustrate the different portions of a Gaussian beam, schematically. In Figure 2.4 *left* with the plane surface the propagation times τ_l are equal for all cases, while in *right* they differ. Therefore, an averaged time delay between τ_l and $\tau_l + \Delta\tau$ will be measured.

Material density fluctuations may result in different propagation times between portions of the beam as well. However, a rather constant curvature such as of a tube wall can be compensated by using a similarly curved conducting object for the calibration. This procedure is described in the following section.

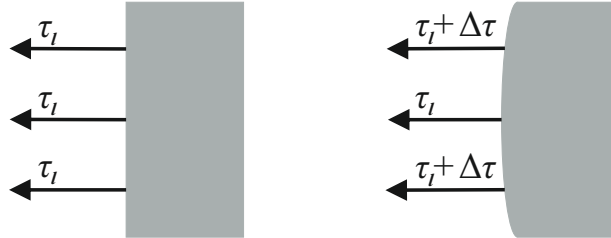


Figure 2.4: Schematic of reflections by *left*: plane and *right*: curved boundary surfaces

2.4 Preprocessing

A frequency analysis of the measured signal determines the propagation times of the beam sections and hence, thicknesses of the SUT layers. However, it also contains reflections by the measurement system, which have to be compensated. Therefore, a preprocessing procedure is performed. The included calibration requires an analytic representation of the signal, which is calculated first.

Figure 2.5 illustrates the complete procedure. To reduce noise, the measured signal can be buffered and averaged. A bandpass filter is used afterwards for two reasons. On the one hand, it suppresses the frequency portions corresponding to distances, which are not representing the region-of-interest. In this way, direct current portions can be reduced. On the other hand, a band-limited signal is required for the calculation of the analytic representation.

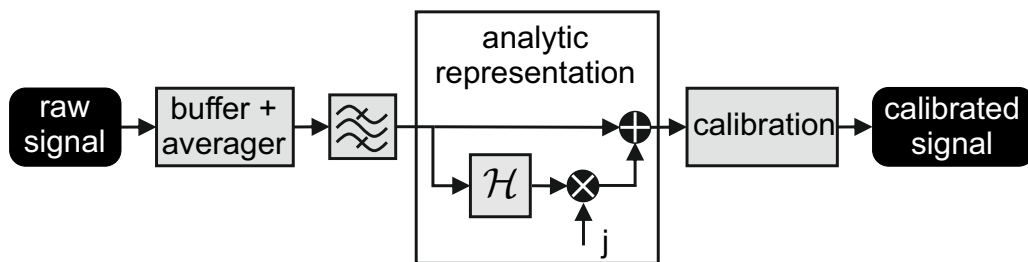


Figure 2.5: Preprocessing: averager to reduce noise, bandpass to cut off insignificant frequency portions, analytic representation (\equiv real and imaginary part are related by Hilbert transform \mathcal{H}), and calibration to remove reflections caused by the setup

Originally, the term analytic specifies continuous signals with zero spectral components at negative frequencies. Hence, an analytic signal has to be complex in values. It also has the property, that its real and imaginary part are related

by a $\pi/2$ shift in time domain. In the frequency domain, their relation can be mathematically described by Hilbert transform. For data transmission, by ideally shifting the center frequency of a band-limited signal to an appropriate higher frequency range, this modulated signal does not contain any negative frequency portions. Then, it is sufficient to solely transfer the real part of the signal. The Hilbert transform property of analytical signals allows to reconstruct their imaginary parts from the real portions as shown in Figure 2.5.

In [62], a definition is proposed for a discrete-time signal. It requests a $\pi/2$ phase shift between its real and imaginary part as well. Since the measurement signals are not inherently band-limited, the bandpass removes portions, which cannot be reconstructed afterwards. Therefore, it is advantageous to cut off frequency portions that do not represent the SUT.

One method to calculate an analytic representation of the signal is based on utilizing the discrete Fourier transformation (DFT). The real bandpass-filtered signal s_{BP} is transformed into the frequency range and multiplied with the Heaviside function

$$\Theta[k] = \begin{cases} 1, & \text{if } k > 0 \\ \frac{1}{2}, & \text{if } k = 0 \\ 0, & \text{otherwise} \end{cases} \quad (2.15)$$

with digital frequency k . The inverse transformed results in a complex signal $\underline{s}_{BP}[n]$, whose real and imaginary part are related by Hilbert transform \mathcal{H} :

$$\underline{s}_{BP}[n] = s_{BP}[n] + j(\mathcal{H}\{s_{BP}\}[n]). \quad (2.16)$$

Figure 2.8 *left* displays the artifacts of this calculation variant comparing an ideal signal with a version utilizing the procedure. The positive peak at the beat frequency $f = 30.98$ kHz corresponds to a reflector at $d = 10$ cm. Due to the restricted measurement duration or rather bandwidth, the spectrum corresponds to a sinc function instead of an ideal Dirac distribution. The resulting DFT-based signal slightly differs from the ideal one in terms of side lobe level and their maxima positions.

An alternative method for generating an analytical signal is the utilization of a finite length impulse response (FIR) filter. Its impulse response equals

$$\underline{h}_{FIR}[n] = \sum_{v=1}^q \underline{b}_v \delta[n - v] \quad (2.17)$$

with filter length q , coefficients $\underline{b}_1, \underline{b}_2, \dots, \underline{b}_q$, $n \in \{0, 1, \dots, N - 1\}$, and the number of samples N . The equation 2.17 indicates that the current sample of the output depends on q weighted variants of the input. The discrete Dirac distribution $\delta[n]$ is defined by

$$\delta[n] = \begin{cases} 1, & \text{if } n = 0 \\ 0, & \text{otherwise.} \end{cases} \quad (2.18)$$

One advantage of FIR filters is their stability inherently given by their finite impulse response. Since the passband is limited in this case, they enable to additionally substitute the bandpass filter of Figure 2.5 resulting in Figure 2.6.

With MATLAB, a Hilbert FIR filter has been designed using the function `designfilt` [63]. Since the distance between the focus and the transceiver is constant, this value can be used to allow a wide transition band. Figure 2.7 *left* depicts the amplitude of the frequency response of such a configuration with a filter length of 50 samples and a distance between sensor and focus of 60 cm. Due to the wide transmission band of 30 cm, potential passband ripples are minor. The phase of the filter is linear, which prevents the distortion of the signal. If necessary, the linear phase shift can be compensated by forward-backward filtering or by the following calibration.



Figure 2.6: FIR-based preprocessing: averager, FIR filter as bandpass and to calculate the analytic representation, as well as calibration

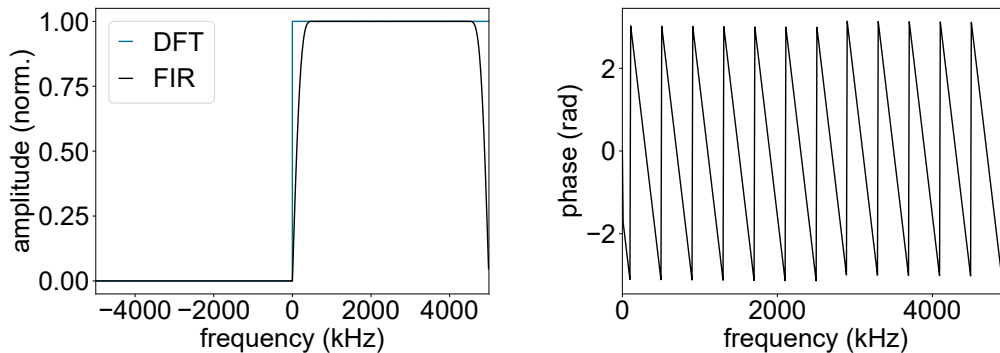


Figure 2.7: Frequency response of an FIR Hilbert filter *left*: amplitude, *right*: linear phase

For DFT, the windowing process usually results in ringing, which was suppressed by removing signal portions at the origin and the end. For FIR, the sequence has been cut off according to the filter length. Figure 2.8 *right* shows the influence of an FIR Hilbert filter for a transmission width of 20 cm indicating a higher conformity between the resulting and ideal signal.

The calibration according to [64] is based on the assumption of three different main disturbing influences in case of reflectivity measurements in free space – leakage of the signal, the frequency response of the whole system, and an imperfect impedance matching. Since the setup includes a horn antenna, the impact of a mismatch may be negligible. To compensate for the two remaining influences, two individual measurements are sufficient referred to a two-term (2T) calibration. In this context, the calibration standards empty room and conducting plate

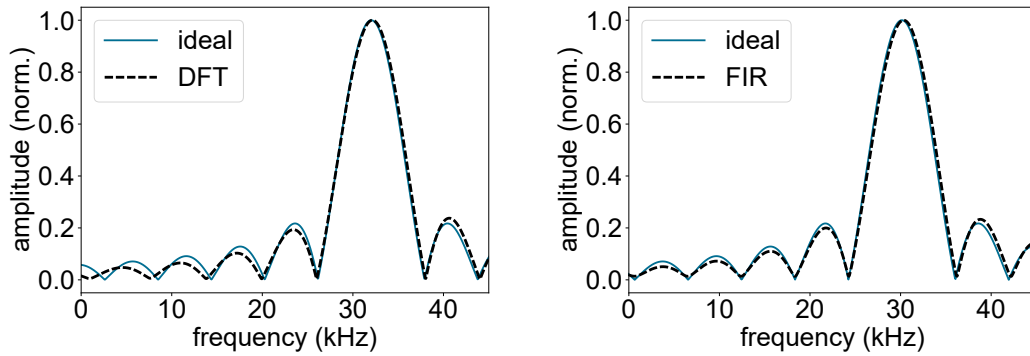


Figure 2.8: Influence of calculating an analytic representation of an ideal signal using *left*: DFT and *right*: FIR

depicted in Figure 2.9 were chosen. The ideal empty room represents a measurement scenario without any reflections apart from the ones of the internal system such as by the optical unit or leakage. Therefore, it is proposed to apply a gate to reduce remaining reflections by the room walls in [64]. The conducting plate, which is perpendicular to the optical axis, corresponds to the maximum reflection. Ideally, it is positioned at the beam waist, to achieve the highest lateral resolution.

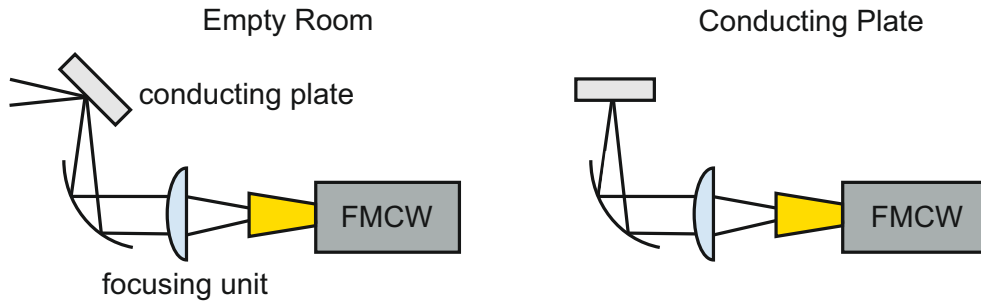


Figure 2.9: Calibration standards *left*: empty room approached by reflecting the beam away from the optical axis, *right*: conducting plate corresponds to maximum reflection

To suppress the influence of noise, the corresponding signals \underline{s}_{ER} and \underline{s}_{CP} of empty room and conducting plate are averaged. The calibration process of the bandpass-filtered signal \underline{s}_{BP} is described by

$$\underline{s}_{2T}[n] = -\frac{\underline{s}_{BP}[n] - \underline{s}_{ER}[n]}{\underline{s}_{CP}[n] - \underline{s}_{ER}[n]} \quad (2.19)$$

with the calibrated output \underline{s}_{2T} .

For analytic signals, modulation and demodulation can be described, the multiplying the time representation by a complex exponential function. The ideal conducting plate standard corresponds to a single oscillation. The division of

equation 2.19 can therefore be interpreted as demodulation as well. Then, the new beat frequencies are relative differences between the old position and the conducting plate, referred to as reference plane. By dividing by $\underline{s}_{CP}[n] - \underline{s}_{ER}[n]$, propagation time differences of beam portions along the plane are compensated for this position.

Since the conducting plate defines the shape of the reference plane, for the measurement of tube walls, a conducting tube section with the same diameter is beneficial to compensate for phase shifts between beam portions. In chapter 3 and 5, the measurements of the conducting plate standard are used to estimate the characteristic of the setup noise, because not any alignment of the SUT is then required. The preprocessed signal enables analyzing the propagation time information to evaluate distances or thicknesses.

2.5 Depth Resolution

For determining beat frequencies of the different reflections illustrated by equation 2.8, the DFT can be applied. After calibration, the distance between one peak in the frequency domain and the origin is supposed to be proportional to the distance between boundary surface and the reference plane. Utilizing the Fourier transform, an infinite signal length and a single reflection would result one Dirac distribution at the exact beat frequencies. However, the resulting finite length can be expressed by multiplying the signal by a rectangular window function [65]. Therefore, the spectrum of the corresponding infinite length signal is convoluted with a sinc function. The potential of separating two reflections originating from different distances is referred to as depth resolution. Due to the interference in case of more than one reflection, the resolution depends on the width of the peaks. For the following simulations, a setup according to section 2.2 was used. In Figure 2.10 *left*, the amplitude spectrum of a conducting plate is calculated applying the inherent rectangular window function (conducting rectangular). The resulting sinc function represents a single main reflection. It has been interpolated by zero padding: by adding zeros at the end of the signal, the number of frequency points can be increased to interpolate the spectrum [66], [67]. The width of the main lobe restricts the ability to separate this signal from a second reflection.

According to the Rayleigh criterion, the minimum distance which can be evaluated is approached as the difference of the maximum and its first zero crossing. The corresponding Rayleigh resolution limit Δr_R equals

$$\Delta r_R = \frac{c_0}{2\eta B} \quad (2.20)$$

[68]. For the setup parameters of section 2.2, Δr_R equals 3.9 mm for $\eta = 1$. The limit is inversely proportional to the refractive index η and the bandwidth B . In case of a constant B , the product $\Delta r_R \cdot \eta$ remains unchanged. It indicates the optical path length of the limit, which enables generalized observation on the resolution. In case of a single reflection, the center frequency f_b of the sinc function is proportional to the propagation time τ . Then the x-axis can be linearly

transformed into the optical path length.

The following simulations indicate difficulties for layer thicknesses in approximation of the Rayleigh limit. For simplicity, in this section, solely main reflections have been considered because for many samples-under-test, the multiple reflections are much smaller than the main ones. Figure 2.10 *left* illustrates a shift of the main lobe of the conducting plate (conducting rectangular) by adding a second peak (dielectric rectangular) at an optical path length of 4.1 mm. The amplitudes of the first and second reflections were 1 and -1 , respectively. For absorption-free single layers in air, this ratio¹ of -1 is rough estimate for single layers. To reduce the influences of different sinc functions on each other, the time-domain signal can be multiplied by a window function. The function solely suppresses the side lobes but increases the width on the main lobes such as for a dielectric sheet and for applying the Hamming window (dielectric Hamming). For this example, only one peak can be evaluated demonstrating that window functions are not beneficial for evaluating thin layers due to the reduced resolution.

Figure 2.10 *right* illustrates the measurement error as a function of the optical path length of the thickness. Solely for values, which are larger than $2\Delta r_R$, evaluating the maxima (peak detection) delivers rather accurate results with deviations smaller than 5% of the absolute thickness. This threshold of $2\Delta r_R$ corresponds to the distance of the main lobe and first zero crossing after applying Hamming window. However, for thicker samples, also a more selective window function could be chosen, which increases the width, but further suppresses side lobes.

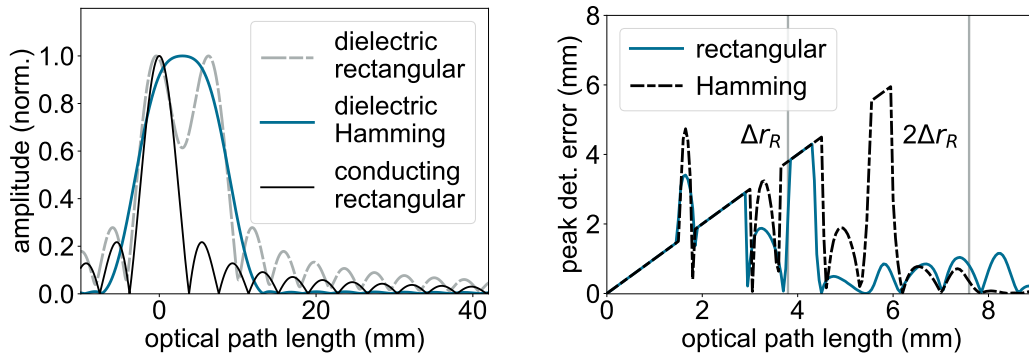


Figure 2.10: *left*: simulated signal of conducting plate (black), dielectric sheet (blue) and dielectric sheet using Hamming window (dashed, gray), *right*: thickness error by peak detection as function of optical path length, vertical lines at Rayleigh limit Δr_R and $2\Delta r_R$

Hence, the Rayleigh limit does not indicate the minimum thickness, which can be accurately evaluated by peak detection, since also the side lobes can affect the maxima position. For this reason, an alternative heuristic resolution limit is proposed as the distance between main peak and the first side lobe:

$$\Delta r_S \approx 0.72 \cdot \frac{c_0}{\eta B}. \quad (2.21)$$

¹For $\eta < 2$, the deviation from this value equals less than 12%.

Due to the approximate symmetry of the amplitude spectrum in this point, the influence of the side lobe on the peak positions is reduced. The optical path length $\Delta r_S \approx 5.5$ mm indicates a negligible error for the rectangular window. Above $2\Delta r_S$, peak detection after applying the Hamming window even results in deviations smaller than 0.7%.

For the given setup, the only way to improve the depth resolution is to increase the bandwidth. In case of frequency multiplication, the lateral resolution is simultaneously improved but a higher bandwidth comes with an increased center frequency and therefore, a lower penetration depth. However, several applications require measuring thin layers in composition with thicker materials. One solution is the combination of utilizing the lower frequency range with the maximum penetration depth and to expand the resolution limit to thinner layers using signal-processing techniques.

Figure 2.11 represents an additional observation: two signals with a rather high conformity. The boundary surfaces are positioned at optical path length of 0 mm and 3.5 mm as well as -1 mm and 4.5 mm, respectively. The corresponding thick-

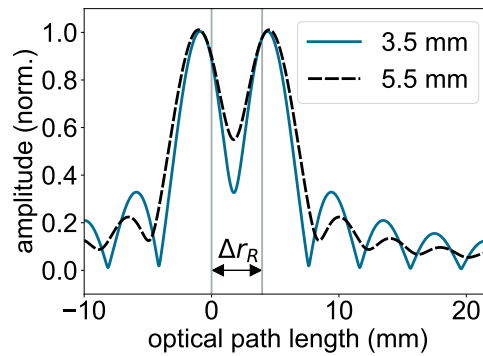


Figure 2.11: Calculated signals of thicknesses of 3.5 mm and 5.5 mm, Rayleigh limit Δr_R

nesses equaled 3.5 mm and 5.5 mm. Applying peak detection, similar thicknesses would be evaluated. To differentiate both cases and similar ambiguities is an additional difficulty for accurate signal processing.

For FMCW, solely applying DFT is invariably limited by the measurement duration or the bandwidth. However, since information of the measurement signal is given, since it conforms to oscillation in additive noise, model-based approaches represent an alternative option for frequency analysis. In the next chapter, spectral estimation techniques are discussed, which enable estimating the power spectral density of the signal based on few parameters.

3. Spectrum Estimation

For a frequency-modulated continuous-wave (FMCW) measurement signal, the propagation time of a single reflection transfers linearly into its frequency and zero phase values. If the Fourier transform is applied for a frequency analysis of time-limited measurement signal, the inherent width of the peaks restricts resolving two or more reflections. Additionally, for thin layers, interference shifts the maxima positions. If such distances are calculated to determine the propagation times and hence thicknesses, biased results are obtained. Spectrum estimation algorithms enable approaching the power spectral density for ergodic¹ processes using information of the signal such as expecting exponential functions in additive noise. Using the evaluated parameters, the corresponding power spectral densities are not restricted by the measurement duration (or bandwidth in case of FMCW) resulting in thinner peaks particularly in case the model fits the process [67].

Several variants for estimation algorithms are described in [67], [69]. Three different sets of variants are separated in [69]: nonparametric, parametric and subspace² methods. The nonparametric variants are based on estimates of the autocorrelation function, which is Fourier-transformed afterwards to approach the power spectral density. The quality of the estimation is supposed to be improved such as by compensating for noise utilizing averaging. However, the resolution remains a function of the length of the data set. It even downgrades in case of applying a window function similar to section 2.5. Therefore, these algorithms are not as promising for the thickness measurements and not considered in the following sections.

The parametric algorithms are based on autoregressive models: for the ideal signal, the current data sample can be estimated using previous ones. One hypothetical application to illustrate the potential of such methods is the option of extrapolating signal points based on the model. For Fourier transform, the signal values are assumed to be 0 outside the measurement interval. Adding samples, which differ from 0, the bandwidth is artificially increased and the Rayleigh resolution limit reduced. However, in case of a poor estimation, the signal quality is adversely affected which could lead to biased results. The measured signal or autoregressive process can be designed as the output of an all-pole infinite impulse response filter, whose input corresponds to additive white noise. Instead of

¹The characteristic of ergodicity is introduced in chapter 5 and, e.g., requires the process to be wide-sense stationary.

²Subspace methods are also referred to as frequency estimation approaches.

extrapolating the data, the parameters of the filter are directly processed because they already contain significant information of the signal: the poles of the filter indicate the requested frequencies.

Subspace methods separate the signal and noise information into two different subspaces utilizing their orthogonality. For oscillations, the orthogonal characteristic is given in case of additive white noise. The resulting signal or noise subspace then enables designing a filter, which determines the estimated frequencies and approaches the power spectral density of the signal as well.

Variants of parametric and subspace methods have been tested in [57], [70]–[72] for similar applications to increase the distance resolution between targets or the resolution of images [73]. However, distances in the range or below the Rayleigh limit can lead to inaccurate results as shown in [70], [71]. The aim of this chapter is to systematically analyze the applicability of spectrum estimation algorithms for reliable thickness evaluations using the presented setup of section 2.2. Besides the ability to separate neighboring peaks, the bias between evaluated and true thickness values, is an important criterion.

In this chapter, for each variant of parametric and subspace methods, one promising algorithm is exemplarily introduced: modified covariance method and multiple signal classification (MUSIC). Both are based on the model order, which is a linear function of the number of significant reflections for the ideal case. The influence of the preprocessing procedure on it is analyzed. Finally, the signal-to-noise ratio of the setup is estimated and its influence on the results is discussed.

3.1 Parametric Estimation

The parametric estimation algorithms are based on the autoregression model. For such signals, the current data sample depends linearly on previous ones according to model order p . The Z-transform indicates, that for such a model of a closed feedback loop, a time delay of one lag corresponds to a pole in the Z-domain, and therefore as well for the discrete Fourier transform (DFT) spectrum. An estimate of these poles indicate a pseudo power spectrum P_{AR} ,

$$P_{AR}[k] = \frac{|b|^2}{\left|1 + \sum_{l=1}^p \underline{a}_l e^{-jl2\pi \frac{k}{N}}\right|^2} \quad (3.1)$$

for autoregressive processes with digital frequency index k , complex factors b , \underline{a}_1 , $\underline{a}_2, \dots, \underline{a}_p$, and the total number of samples N . The term pseudo suggests that the spectrum usually differs from the power spectral density. While the positions of the frequencies are approached by peaks, the total power differs from the one of the actual signal.

However, an alternative method is the covariance method that is restricted to the measured data points and therefore more promising in terms of resolution. It is

based on the covariance equation, which is then minimized:

$$\begin{pmatrix} r_x(1,1) & r_x(2,1) & \cdots & r_x(p,1) \\ r_x(1,2) & r_x(2,2) & \cdots & r_x(p,2) \\ \vdots & \vdots & \ddots & \vdots \\ r_x(1,p) & r_x(2,p) & \cdots & r_x(p,p) \end{pmatrix} \cdot \begin{pmatrix} \underline{a}_1 \\ \underline{a}_2 \\ \vdots \\ \underline{a}_p \end{pmatrix} = - \begin{pmatrix} r_x(0,1) \\ r_x(0,2) \\ \vdots \\ r_x(0,p) \end{pmatrix} \quad (3.2)$$

with

$$r_x(\nu, \nu) = \sum_{n=p}^{N-1} \underline{x}[n-\nu] \underline{x}^*[n-\nu] \quad (3.3)$$

for the entry (ν, ν) with $\nu, \nu \in \{0, 1, \dots, p\}$. The term $\underline{x}[n]$ denotes a signal, which is superposed with additive noise, and $\underline{x}^*[n]$ corresponds to its complex conjugate. A disadvantage of the covariance method is that unstable results can occur: applying system theory, it can be derived that poles outside the unit circle do not result in stable filters. However, the covariance method does not restrict the position of the poles. Therefore, in this work, the modified covariance method³ is preferred with the modified covariance function

$$r_x(\nu, \nu) = \sum_{n=p}^{N-1} \underline{x}[n-\nu] \underline{x}^*[n-\nu] + \underline{x}[n-p+\nu] \underline{x}^*[n-p+\nu]. \quad (3.4)$$

The first term of the sum equals the covariance method and can be interpreted as a forward prediction error. Then, the second term equals the backward error. For modified covariance method, both are minimized at once. The combination is justified, since $\underline{x}[n]$ and $\underline{x}^*[n-\nu]$ result in the same auto-correlation function. However, in case the forward filter is unstable, the backward error would grow and dominate the total error. Since the same compensation can be analogously observed for the inverse case, the probability of unstable solutions is reduced. The modified covariance method [74] is a promising variant for FMCW thickness evaluation due to additional reasons. The estimated spectra are statistically stable [75] and the peak positions are not as sensitive to the initial phase as other algorithms [74].

Equation 3.2 results in estimates of the coefficients $(\underline{a}_1, \underline{a}_2, \dots, \underline{a}_p)^T$ with the transposition operator $\{\cdot\}^T$. The denominator of equation 3.1 can be rewritten as a product of roots indicating the beat frequencies of the signal [69].

³The method is also referred to as forward-backward method, least square method or forward-backward least square method [69].

3.2 Subspace Method

The subspace methods⁴ are based on the estimation of complex exponential functions in additive white noise $\underline{\omega}[n]$ with variance σ_n^2 :

$$\underline{x}[n] = \sum_{l=1}^p \underline{a}_l e^{j2\pi k_l \frac{n}{N}} + \underline{\omega}[n] \quad (3.5)$$

with model order p , complex amplitude \underline{a}_l , and frequency parameter k_l . By comparing equation 3.5 and the analytic representation of 2.8, it can be derived that \underline{a}_l models the approximate real amplitude a_l as well as the phase shift by zero phase ϕ_{τ_l} . The quotient of beat and sampling frequency in contrast equals the term k_l/N .

Since the white noise is uncorrelated, its auto-correlation function equals $\sigma_n^2 \delta[n]$ with Dirac distribution $\delta[n]$. Then, the auto-correlation function of the sum of signal and noise corresponds to

$$r_x[v] = \sum_{l=1}^p P_l e^{j2\pi k_l \frac{v}{N}} + \sigma_n^2 \delta[v] \quad (3.6)$$

with power $P_l = |\underline{a}_l|^2$. It indicates the orthogonality between signal and noise for each v under the assumption of additive white Gaussian noise (AWGN). The $M \times M$ auto-correlation matrix with $M > p$

$$\begin{aligned} \mathbf{R}_x &= \mathbf{R}_s + \mathbf{R}_n \\ &= \begin{pmatrix} r_x[0] & r_x[-1] & \cdots & r_x[-M+1] \\ r_x[1] & r_x[0] & \cdots & r_x[-M+2] \\ \vdots & \vdots & \ddots & \vdots \\ r_x[M-1] & r_x[M-2] & \cdots & r_x[0] \end{pmatrix} + \sigma_n^2 \cdot \mathbf{I}_M \end{aligned} \quad (3.7)$$

is therefore the sum of matrices of signal \mathbf{R}_s and noise \mathbf{R}_n . The term \mathbf{I}_M represents the unity matrix with rank M . The rank of \mathbf{R}_s equals p . Performing an eigenvalue decomposition enables the separation into signal and noise subspace. Usually, the condition $M = p + 1$ is sufficient for the decomposition. The lowest eigenvalue serves as an estimate of the noise variance σ_n^2 . Then, the noise subspace is characterized by a dimension of one and is spanned by the corresponding eigenvector. However, a more precise estimate of the variance can be evaluated by averaging. In this thesis, the MUSIC algorithm [76] was chosen due to its promising results in [57], [71] for distance evaluations. It requires $M > p + 1$. Then, the $M - p$ lowest eigenvalues are estimates of the noise variance σ_n^2 which can also be averaged. One of the corresponding noise eigenvectors is orthogonal to the signal vectors, since their product equals 0 for the estimated frequencies.

⁴also referred to as frequency estimation in [69]

For its multiplicative inverse, these zeros corresponds to poles. Due to averaging, the resulting pseudo spectrum can be estimated precisely as

$$P_M[k] = \frac{1}{\sum_{m=p+1}^M |\mathbf{e}\mathbf{v}_m|^2} \quad (3.8)$$

with noise eigenvectors $\mathbf{v}_{p+1}, \mathbf{v}_{p+2}, \dots, \mathbf{v}_M$ of the $(M - p)$ lowest eigenvalues, $\mathbf{e} = (1, e^{-j2\pi k \frac{1}{N}}, \dots, e^{-j2\pi k \frac{M-1}{N}})$. Again, the requested frequencies are indicated by the positions of the poles.

3.3 Model Order

For evaluating measured data, both, modified covariance method and MUSIC algorithm, require the determination of the model order p representing the measurement scenario. Usually, it equals 1 for one complex exponential function and hence, 2 for one sinusoid⁵. For an ideal signal of $L + 1$ significant reflections, it then corresponds to $2L + 2$ for the real representation. The amplitudes of the main reflections are usually rather high. Then, all of them have to be considered for calculating the model order. The amplitudes of multiple reflections are often low or even approach 0 after few reflections. Depending on the refractive indices, the number of significant reflections has to be determined individually for each SUT. Moreover, spurious echoes and noise can affect the model order. For instance, in [69], different functions are compared to estimate this value for given data sets. The model order is varied until a minimum of this function is found. Then, the corresponding value is assumed to serve as an appropriate estimate. In [77], the effects of wrong values such as peaks at zero or half of the sampling rate are used to approach the best fit.

In the following section, the influence of the preprocessing (calculation of analytic representation and calibration according to Figure 2.5) is analyzed by simulations based on the Signal Processing Toolbox of MATLAB [78]. For simplicity, multiple reflections were not included. An ideal analytical signal for L layers solely consists of $L + 1$ spectral peaks. Therefore, a model order of $p = L + 1$ is assumed. However, Figure 3.1 indicates an influence of the FIR-based preprocessing. For two reflections, model orders of $p = 2$, $p = 4$ and $p = 8$ were not sufficient for modified covariance method to separate two reflectors at 0 mm and 4 mm. In contrast, $p = 30$ resulted in the exact positions⁶. However, in case the model order was adapted, the modified covariance method determined the exact frequency portions, which could not be extracted from the DFT spectrum even though the distance of 4 mm is slightly larger than the Rayleigh limit of 3.9 mm. For modified covariance method, the width of the peaks and hence the resolution limit were significantly reduced. Moreover, side lobes cannot be observed in the pseudo

⁵which can be illustrated by Euler's formula

⁶Similar results were obtained for the alternative configurations, DFT-based generation of an analytic representation and for MUSIC algorithm.

spectra of the modified covariance method. This characteristic could be significant for thickness measurements, if the amplitude of a reflection was smaller than the side lobes of another one.

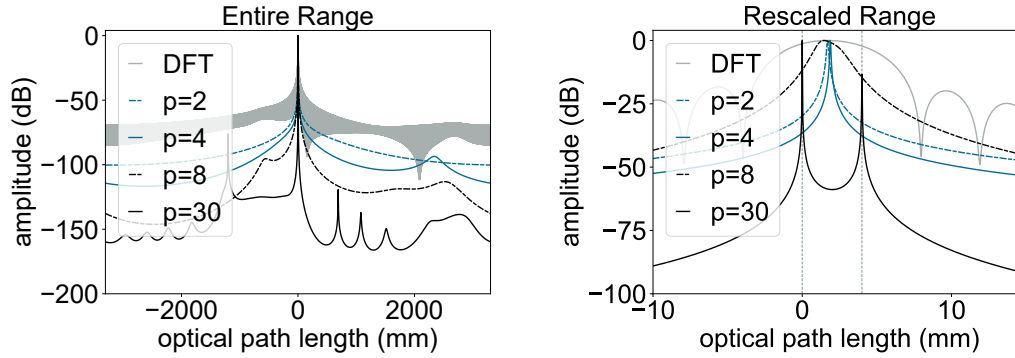


Figure 3.1: Power spectral density of the simulated signal via discrete Fourier transform (DFT) and pseudo spectra of modified covariance method using different model orders for FIR-based preprocessing according to section 2.4. The x-axis was rescaled from *left* to *right* in order to improve the visibility of the peaks. The vertical lines in *right* correspond to positions of reflectors at 0 mm and 4 mm.

In terms of the model order, Figure 3.2 shows more gradual results of additional simulations for both MUSIC and modified covariance method. The model order varies from 2 to 50 in steps of 2. Four simulations were performed for each value: The position of the first reflector remained at 0 mm, while the second one moved from 1 mm to 4 mm in 1 mm steps. The optical path length is depicted in Figure 3.2. Hence, markers at 0 mm, 1 mm, 2 mm, 3 mm and 4 mm were expected even at a model order of 2.

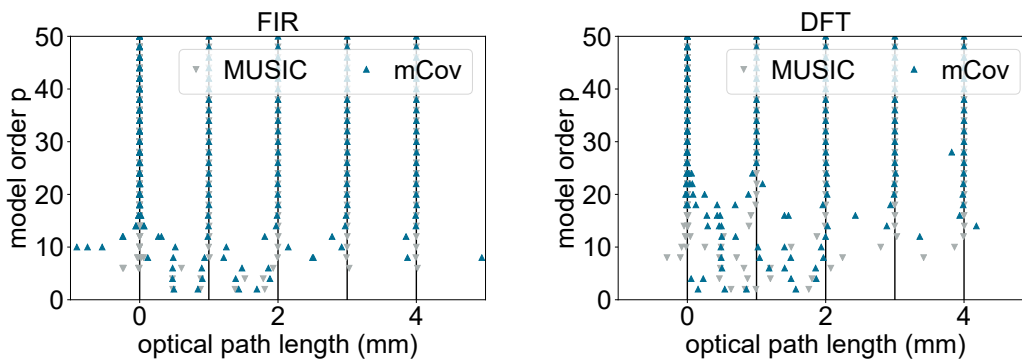


Figure 3.2: Evaluated positions of different model orders using *left*: finite impulse response (FIR), *right*: discrete Fourier transform (DFT)-based preprocessing utilizing MUSIC and modified covariance method (mCov)

For the preprocessing in section 2.4, two different options were presented to generate analytical representations of the signals: a finite impulse response (FIR)

and a DFT variant. For FIR filtering represented in Figure 3.2 *left*, $p = 16$ appears to be sufficient to accurately determine all thicknesses. The DFT variant in *right* requires $p = 26$ for accurate estimates. For higher model orders, additional markers can occur such as at $p = 28$, which would be processed as an inaccurate thickness. Nevertheless, since all distances are close or smaller than the Rayleigh limit, the resolution is significantly improved in comparison to the DFT-based evaluation.

Again, the model order was affected. While the real signals (before preprocessing) were simulated as ideal, the generation of an analytical representation and the calibration are identified as an influences on p . The calibrated signal is assumed to not ideally conform to the described autoregressive model (characterized by the original p). For instance, the influence on the calibration is analyzed: in case of an ideal conducting plate signal, the division would correspond to a demodulation and shift the peak position which would not affect p . However, the conducting plate signal is non-ideal because it is influenced by the artifacts of the bandpass filtering (such as presented in Figure 2.8 *right*). However, for measured signals, the calibration cannot be neglected, because it significantly improves the quality of the signals. Particularly, for measured data, the model order can additionally be affected by additive noise, which is analyzed in the next section.

3.4 Influence of Additive White Gaussian Noise

To determine a realistic model of the setup's noise, its characteristic is analyzed. A statistic 500 measurements of a conducting plate standard (which served as a calibration standard in section 2.4) was performed at the reference plane. At this position, the ideal signal solely consists of entries of one, due to the division within the calibration process. The deviation from this value for each time sample is assumed to be caused by AWGN⁷. A resulting noise variance of $3.42 \cdot 10^{-4}$ was observed.

Figures 3.3 and 3.4 present the results of corresponding simulations. The first reflector was positioned at 0 mm, while the second one varied from 0 mm to 10 mm. In contrast to the previous section, the signals corresponded their ideal analytic representations consisting of one complex exponential function for one reflection. A value of $p = 2$ was used for all cases. The resulting thickness errors without the presence of noise are represented in Figure 3.3. For the modified covariance method, the error equaled 0 for all positions. MUSIC algorithm resulted in biased values in particular for the smaller distances. This deviation could be influenced by the absence of AWGN, which was however assumed for MUSIC: the noise eigenvectors are the basis to determine the poles of the filter.

In Figure 3.4, results are given for the estimated noise characteristic. Errors up to distance of 3.19 m, which equals half of the sampling rate, occurred. Even in the region of optical path lengths close to 10 mm, the maximum error is still larger than 1 mm. However, these distances can be evaluated accurately by Fourier

⁷Chapter 5 will present indications for this assumption.

transform-based peak detection.

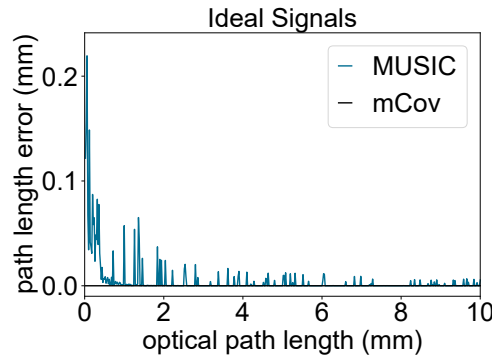


Figure 3.3: Evaluated distance error without the presence of noise by MUSIC algorithm and modified covariance method (mCov)

It can be observed, that the AWGN influences the order p : for rather high noise levels, it will be modeled by the process resulting in biased peaks. Evaluating a distance equal to half of the sampling rate indicates that the procedure of [77] to estimate the resulting model order might not work in this case: it may classify the order as too high, while it is in fact too low to separate the neighboring peaks (in particular for distances below the Rayleigh limit of 3.9 mm). Even in case the measured signal conforms to the model, AWGN might still affect the values. Hence, for each data set, a new model order would have to be chosen. Therefore, it is assumed that evaluated results may significantly vary and be unreliable similar to an exemplary measurement of a tube wall sections evaluated in [2].

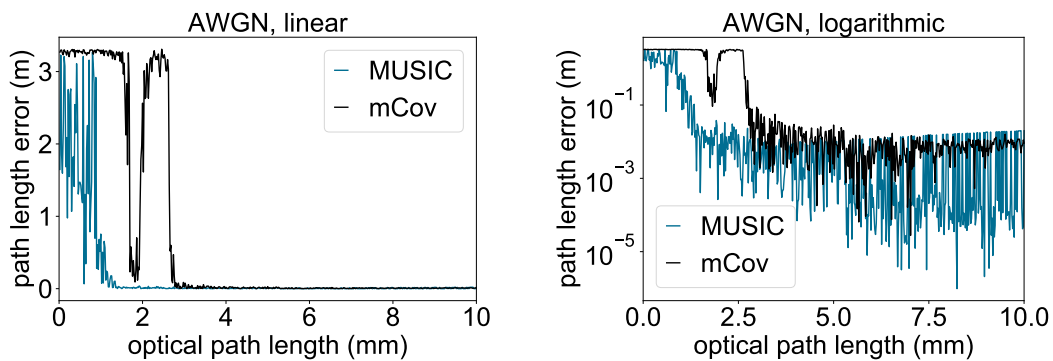


Figure 3.4: Evaluated distance error in the presence of AWGN by MUSIC algorithm and modified covariance method (mCov) *left*: linear scale, *right*: logarithmic scale

Based on simulated signals, both modified covariance method and MUSIC algorithm enable to determine distances and hence layer thicknesses below the Rayleigh limit, since the resulting pseudo spectra were characterized by peaks thinner than the sinc functions resulting from DFT. Due to the absence of side lobes, the quality of thickness measurements but also imaging could be signifi-

cantly improved in case the model order could be adapted for each single measurement. However, in presence of significant multiple reflection, the model does not differentiate between those and the main reflections. Therefore, an investigation would be required, to trace the single reflections and extract the resulting distances. One additional disadvantage of the spectral estimation methods is that peaks cannot be restricted to a priori given distance intervals. Due to the focusing unit, a region-of-interest is inherently defined, which could be utilized by the processing. The model of the approach, which is discussed in the following chapter, exactly conforms to the measured signal of FMCW. Then, multiple reflections can be included and the search intervals be adapted to a priori given interval.

4. Model-Based Signal Processing

As demonstrated in the last chapters, the frequency-modulated continuous-wave (FMCW) signal consists of oscillations whose frequencies are linear functions of the propagation time of the beam portions. If their frequencies were determined, accurately, the thicknesses could be calculated as proportional values to their differences. In case of a Fourier transform-based analysis, the smallest determinable thickness is restricted to few millimeters [1], [68] due to the superposition of frequency peaks, referred to as Rayleigh resolution limit. For thicknesses in approximation of this limit, biased results are evaluated influenced by side lobes. Spectral estimation algorithms enable modeling the power spectral density of the signal based on few parameters to analyze the frequencies. However, they are likely to result in the evaluation of inaccurate thicknesses [2], [70], [71]: the noise as well as the calibration of the signal influence the model order which is required for an accurate model. In the presence of significant multiple reflections, the origin of all oscillations has to be identified in case of a Fourier transform-based as well as spectral estimation analysis. Only through this, the exact number of layers can be determined and the significant propagation time differences calculated.

Moreover, both methods analyze the complete frequency range determined by the sampling process. However, a wide range of frequencies can be inherently excluded for the presented setup. In case of larger distances between corresponding reflectors and the focus of the optical unit, the amplitudes of those reflections are usually highly reduced. Thus, a certain region-of-interest is inherently given and the processing could be restricted, e.g., to the range corresponding to the Rayleigh length. For many industrial applications, rough or accurate estimates of the layer thicknesses are additionally given. It appears to be beneficial to restrict the search intervals, correspondingly. An alternative model-based approach is presented in this chapter. It compares the measured signal to simulated ones which are calculated by the formula description. The parameters of the best fit then indicate the thicknesses. In case the formula description includes multiple reflections, they are inherently considered and support the accuracy of the thickness analysis. Such model-based approaches have been utilized for terahertz time-domain spectroscopy [4], [38] and material characterization using vector network analysis [79] to resolve structures below the respective resolution limits and are therefore promising for FMCW.

In this chapter, a model-based approach is introduced, which is based on a priori evaluated search intervals for the reflector positions. Fitting a modeled signal to a reference, a high correlation indicates appropriate estimates of the requested thicknesses. The first iteration is based on exhaustive search calculating all potential models within the intervals. For accurate models, the number of significant reflections is analyzed by observing the influence of multiple reflections. A modification of the transfer matrix method is derived to efficiently calculate them by observing the influence of the wave propagation on the measured signal. The procedure is tested for validation. Finally, the model-based method is compared to peak detection, spectrum estimation, and an additional signal-processing technique [80].

4.1 Model-Based Approach

For testing thicknesses in the range of the Rayleigh resolution limit Δr_R discussed in section 2.5 and smaller, an alternative signal-processing approach has to be employed. A promising method is to fit modeled signals to the measured data [1], [5], [8]. For the fitting process either exhaustive search or an optimization algorithm can be applied. The model-based approach is advantageous in case that the number of layers is a priori given.

The model-based approach is introduced using an illustrative example. According to the setup described in section 2.2, a sample-under-test (SUT) with boundary surfaces at optical path lengths of 0 mm and 4 mm as well as amplitudes¹ of 1 and -1 has been observed. The parameters resulted in a reference signal, which was restricted to the main reflections for simplicity. Figure 4.1 *left* depicts the frequency representation. Exhausted search was chosen for the first implementation. Within the search intervals of -5 mm to 5 mm and 0 mm to 10 mm for the boundary surface positions, all combinations of equidistant reflector position were calculated. They were separated by a step size of 50 μm . In order to guarantee accurate results, this size has to be chosen small to hit the global maximum and to minimize the rasterization effects.

The modeled signals have then been calculated conforming to equation 2.8. Figure 4.1 *right* represents the solution space featuring numerous local maxima besides the global one (both indicated by dark shades). The step size of exhausted search then corresponds to width and height of one pixel. Such local optima indicate the conformity of modeled signals with different thicknesses. One of such examples was presented in Figure 2.11. It is caused by the shift of the zero phase as the propagation time increases. The optimization procedure of chapter 6 can utilize the characteristic of several local optima to efficiently evaluate the global one.

The reference \underline{s}_{ref} and modeled signals \underline{s}_{SM} were compared using the Pearson

¹For moderate refractive indices such as 1.8, the actual amplitude of the two main reflections are 0.29 and -0.26 , and therefore, an amplitude ratio of -1 might be an appropriate approximation. The associated thickness would be 2.22 mm.

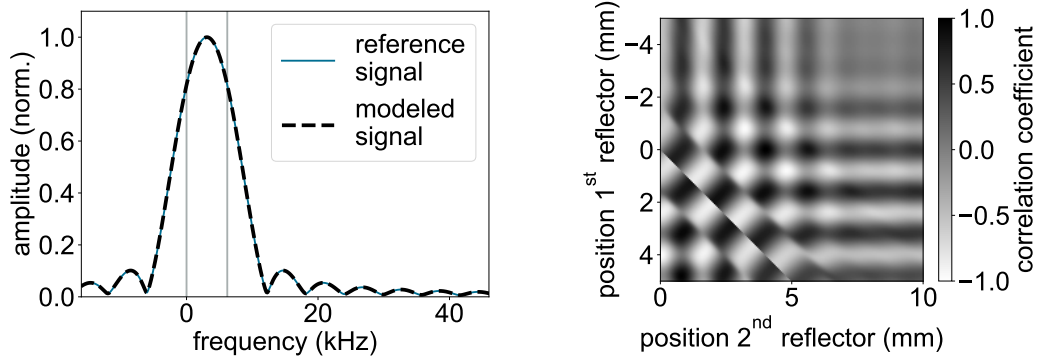


Figure 4.1: *left:* reference and best fit of modeled signals, vertical lines represent the reflector positions at 0 mm and 4 mm *right:* solution space, grayscale indicates the conformity between modeled signal and reference

correlation coefficient r_P :

$$r_P = \frac{\sum_{n=0}^{N-1} (\underline{s}_{ref}[n] - \overline{\underline{s}_{ref}}) \cdot (\underline{s}_{SM}[n] - \overline{\underline{s}_{SM}})^*}{\sqrt{\sum_{n=0}^{N-1} (|\underline{s}_{ref}[n] - \overline{\underline{s}_{ref}}|)^2} \cdot \sqrt{\sum_{n=0}^{N-1} (|\underline{s}_{SM}[n] - \overline{\underline{s}_{SM}}|)^2}} \quad (4.1)$$

with total number of time samples N . The operator $\bar{\cdot}$ denotes the arithmetic mean value. The nominator corresponds to the cross-covariance function to compare the signals. The denominator normalizes the value. For real signals, r_P varies from -1 to 1 . For uncorrelated signal, the coefficient equals zero. In this case, the maximum value is requested.

In case of exhausted search, depending on the search intervals of the SUT and the number of layers, several millions of signal models are usually required. To compensation for the high computation time, the calculations are processed in parallel using graphics processors. For this simulation, the exact signal could be found to identify the accurate thickness of 4 mm. However, for measurements, influences of noise, a nonideal calibration etc. might affect the quality of the results. The measured signal also contains multiple reflections, which can affect the accuracy. Therefore, in the next sections, the compositions are analyzed for which their influence is significant and has to be considered.

4.2 Influence of Multiple Reflections

The influences of multiple reflections on thickness measurements is discussed in the following sections based on the separation of two different cases: for single layers, solely the beam portions of the second boundary surface can influence the evaluation of the main peaks. In case of multilayers, different constellations of main and multiple reflections can interfere.

4.2.1 Single Layers

For single layers in air or on a metal substrate, the most significant influence on the main peak in terms of multiple reflections is the first one of them caused by the second boundary surface. Its amplitude is the highest and the time delay the lowest. The ratio of its amplitude and the one of the second main reflection equals:

$$\xi = \frac{\eta_1 - 1}{\eta_1 + 1} \cdot \frac{\eta_1 - \eta_2}{\eta_1 + \eta_2} \quad (4.2)$$

with the approximately real refractive indices, η_1 of the material and η_2 of the substrate or air utilizing equations 2.4 and 2.5 and neglecting attenuation. For a large ξ , the influence of multiple reflections increases. Two significant configurations can be extracted of the equation: on the one hand, in case of a metal substrate, η_2 can be approximated by a high value to describe the reflection process. It results in rather large absolute values of ξ . On the other hand, for a single layer in air, η_2 equals 1. The value of ξ rises as η_1 increases.

Based on the presented setup, a set of simulations is performed to validate these cases. Figure 4.2 depicts the evaluated error of different materials caused by neglecting multiple reflections. The Fourier transform-based peak detection was applied for the frequency analysis, since the procedure is the most illustrative. For the variants ($\eta_1 = 1.6$, air) and ($\eta_1 = 4$, air), samples-under-test in air were simulated, whereas ($\eta_1 = 1.6$, con) represents a layer on a conducting plate. In case of ($\eta_1 = 1.6$, air), the error was negligible for optical path lengths larger than 1 mm. For the other configurations, the error was more significant. The maximum error of ($\eta_1 = 4$, air) even equaled 1.8 mm for the optical path length of 1.9 mm. This simulation confirmed that multiple reflections are more significant for conducting substrates and for higher contrasts. However, also for small thicknesses, their influence has to be considered.

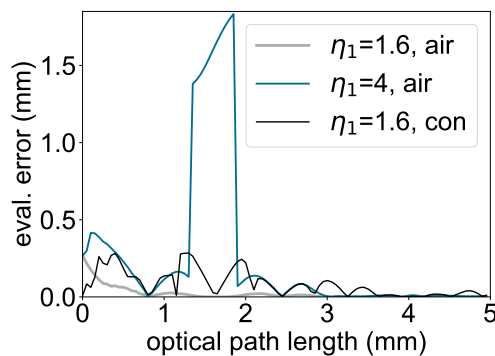


Figure 4.2: Influence of the first one of the multiple reflections on peak detection varying the refractive indices

Figure 4.3 represents the impact of neglecting multiple reflections for a layer of $\eta_1 = 1.6$ in air for different bandwidths. For 40 GHz, the maximum error equals 0.27 mm. Solely for optical path lengths larger than 1.2 mm, deviations smaller

than $26\ \mu\text{m}$ or rather 2.2% of the thickness were determined. By cutting off half and three quarter of the signal's data points, its bandwidth was virtually reduced to $20\ \text{GHz}$ and $10\ \text{GHz}$. The peaks got wider and the degree of interference with multiple reflections increased. Hence, the evaluated error grew. For $10\ \text{GHz}$, significantly high deviations of up to $1.7\ \text{mm}$ occurred. The results indicated that for closer peaks, e.g., in case of reduced bandwidths, the influence of multiple reflections grows.

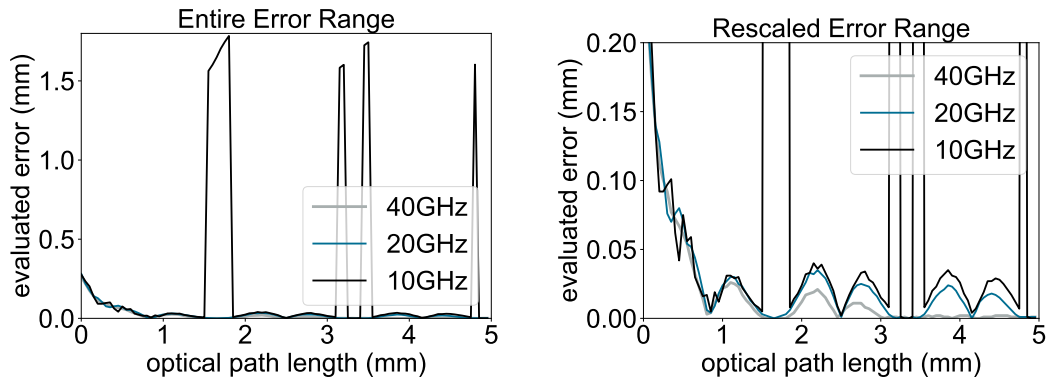


Figure 4.3: Influence of the first one of the multiple reflections on peak detection results varying the bandwidth: from *left to right* the y-axis is rescaled to visualize the range of lower error values.

4.2.2 Multilayers

For multilayer compositions, all multiple reflection can interfere with the different main portions of boundary surfaces depending on the optical path lengths of the layers. Hence, different amplitude ratios can be observed. For each layer system, a rough knowledge of the thicknesses can identify the peaks, which are prone to be superposed. An estimate of the refractive indices delimits the possible amplitudes.

In Figure 4.4, the distance deviation of a single reflector's position is depicted interfering with a second unconsidered peak. They represent a main and the first one of the interfering multiple reflection. The main peak is positioned at $0\ \text{mm}$ and the second one varies from $0\ \text{mm}$ to $10\ \text{mm}$. The amplitude of the second reflection varies along the y-axis. The maximum error is depicted in Figure 4.4 *right* and equals $1.8\ \text{mm}$.

Using the estimates of layer thicknesses, the maximum error caused by the respective portion of the multiple reflections can be evaluated. Generally, increasing the amplitude of the second reflection results in a higher deviation. However, a larger distance does not linearly result in a reduced error, since the phase of the second peaks varies. If the multiple reflections can be neglected, the complexity of the modeled signal reduces to the calculation of the main reflections. However, in case they are significant, an efficient method to calculate them is presented in

the next section.

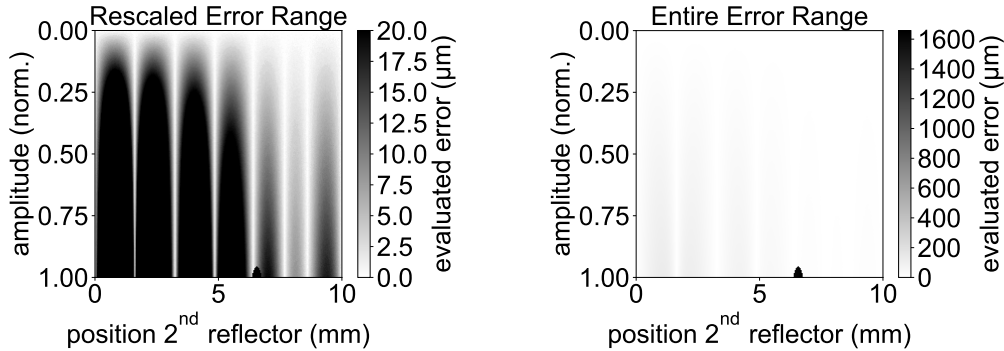


Figure 4.4: Thickness error by interference using peak detection: the position and the amplitude of the second reflection varies. From *left to right*, the maximum depicted value (grayscale) is increased to illustrate the maximum error.

4.3 Modified Transfer Matrix Method

To calculate multiple reflections, different methods can be applied. One approach is to ray trace the beam, which is separated into two parts at each boundary surface [81]. Then, the computational load increases exponentially for each additional layer. The tracing has to be terminated by reaching an amplitude threshold, because in theory the length of the propagation is infinite. Depending on the choice of this threshold, the approach may result in inaccurate thickness values. An alternative recursive procedure is the Rouard method [82] used in [38] for time-domain spectroscopy thickness measurements. Starting with the last boundary surface, the reflected beam portion is calculated and enables the computation of the second last reflection etc. until the first is attained. However, the recursive characteristic of ray tracing and Rouard method may result in rather high computation times.

The iterative transfer matrix method (TMM) [83], [84] instead offers flexibility for parallel computing because intermediate results are independent of each other. Besides reflected, also transmitted signal portions are calculated, which makes the method more flexible for different setup configurations. For the TMM, each layer and boundary surface represents equations based on inputs and outputs according to Figure 4.5. They can be rewritten as matrices, which are multiplied to calculate the complete SUT-specific transfer function. If the TMM was directly applied to an FMCW setup, the sequence of the flow chart in Figure 4.6 *left* would have to be executed: a frequency modulation of 70 GHz–110 GHz has to be calculated considering the Nyquist theorem. With a duration of 170 μs , $2 \cdot 110 \cdot 10^9 \cdot 170 \cdot 10^{-6} = 37.4 \cdot 10^6$ data points are required. For each, an individual transfer matrix is necessary to calculate a transfer function of the respective SUT, which is multiplied with the Fourier-transformed of the signal. The inverse transformed of the product is mixed with a second, time-shifted frequency-modulated

signal. Afterwards, the result must be resampled to conform the sampling frequency of the analog-to-digital converter.

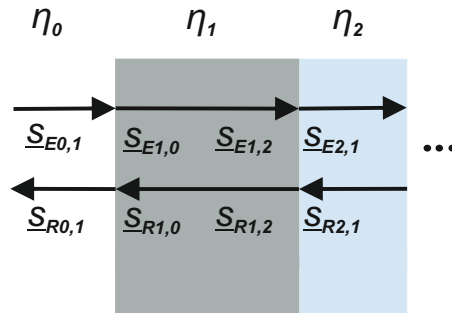


Figure 4.5: Notation of transfer matrix method, each layer corresponds to a quadrupole

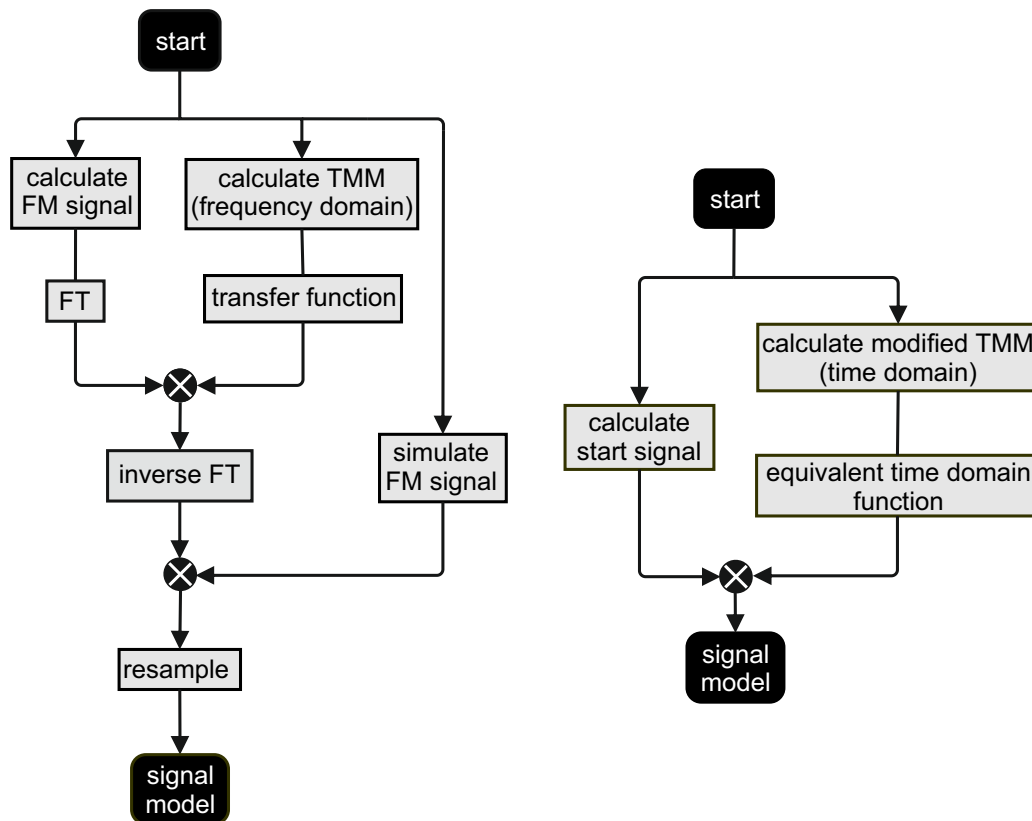


Figure 4.6: Comparison of *left*: classical, *right*: modified TMM, Fourier transform (FT), frequency modulation (FM) for an FMCW setup

A modification of the TMM [1], [9] instead is restricted to compute only the data points of the resulting measurement signal, which equals $N = 1700$ for

$f_s = 10$ MHz and does not require any Fourier transform. Its float chart is depicted in Figure 4.6 *right*. Exclusively, the effects of the wave propagation on the measured data are observed. The idea for the modification can be shown by comparing the reflected wave and the detected signal represented in equations 2.6 and 2.7: variations of amplitudes of the reflections linearly transform the amplitudes of the measured signal's oscillations. Moreover, an increase of propagation time proportionally (by approximation) shifts the beat frequency and the zero phase of the measured signal's oscillations.

The modified transfer matrix for a layer l of L is also based on a crossover matrix $\mathbf{D}_{l,l+1}$ and a propagation matrix \mathbf{P}_{l+1} . The beams of Figure 4.5 result in the following equations for virtual versions of start signal $\underline{s}_{E_{0,1}}$, reflected $\underline{s}_{R_{l,l+1}}$ and emitted $\underline{s}_{E_{l,l+1}}$ portions for attaining the boundary surface between layers l and $l+1$ from layer l . The signal $\underline{s}_{R_{0,1}}$ describes the entire sum reflections:

$$\underline{s}_{E_{l+1,l}}[n] = t_{l,l+1} \cdot \underline{s}_{E_{l,l+1}}[n] + r_{l+1,l} \cdot \underline{s}_{R_{l+1,l}}[n] \quad (4.3)$$

$$\underline{s}_{R_{l,l+1}}[n] = t_{l+1,l} \cdot \underline{s}_{R_{l+1,l}}[n] + r_{l,l+1} \cdot \underline{s}_{E_{l,l+1}}[n]. \quad (4.4)$$

The real approximations of reflection $r_{l,l+1}$ and transmission coefficient $t_{l,l+1}$ correspond to the ones of the electromagnetic wave according the Fresnel equations 2.4 and 2.5. For this purpose, the materials are assumed dispersion-free.

Using matrix $\mathbf{D}_{l,l+1}$,

$$\mathbf{D}_{l,l+1} = \begin{pmatrix} \frac{1}{t_{l,l+1}} & \frac{r_{l,l+1}}{t_{l,l+1}} \\ \frac{r_{l,l+1}}{t_{l,l+1}} & \frac{1}{t_{l,l+1}} \end{pmatrix},$$

the equations 4.3 and 4.4 can be rewritten, as

$$\begin{pmatrix} \underline{s}_{E_{l,l+1}}[n] \\ \underline{s}_{R_{l,l+1}}[n] \end{pmatrix} = \mathbf{D}_{l,l+1} \cdot \begin{pmatrix} \underline{s}_{E_{l+1,l}}[n] \\ \underline{s}_{R_{l+1,l}}[n] \end{pmatrix}. \quad (4.5)$$

Neglecting attenuation, the effect of a propagation corresponding to τ equals a frequency and zero phase shift of the measured signal of $\exp(j2\pi\tau(nB/(Tf_s) + F_1))$. The modified propagation matrix is based on the approximated multiplicity of such shifts: by adding a layer $l+1$ causing a time increase of $\Delta\tau_{l+1}$ the complete propagation

$$\begin{aligned} & \exp\left(j2\pi\frac{B}{Tf_s}(\tau + \Delta\tau_{l+1})n + j2\pi F_1(\tau + \Delta\tau_{l+1})\right) \\ &= \exp\left(j2\pi\frac{B}{Tf_s}\tau n + j2\pi F_1\tau\right) \cdot \exp\left(j2\pi\frac{B}{Tf_s}\Delta\tau_{l+1}n + j2\pi F_1\Delta\tau_{l+1}\right) \end{aligned} \quad (4.6)$$

corresponds to the product of the single terms for τ and $\Delta\tau_{l+1}$. The novel propagation equations for the $(l+1)^{\text{th}}$ layer result in:

$$\underline{s}_{E_{l+1,l+2}}[n] = \exp\left(j2\pi\Delta\tau_{l+1}\left(\frac{B}{Tf_s}n + F_1\right)\right)\underline{s}_{E_{l+1,l}}[n] \quad (4.7)$$

and

$$\underline{s}_{R_{l+1,l}}[n] = \exp\left(j2\pi\Delta\tau_{l+1}\left(\frac{B}{Tf_s}n + F_1\right)\right)\underline{s}_{R_{l+1,l+2}}[n]. \quad (4.8)$$

With matrix $\mathbf{P}_{l+1}[n]$,

$$\mathbf{P}_{l+1}[n] = \begin{pmatrix} e^{-j2\pi\Delta\tau_{l+1}\left(\frac{B}{Tf_s}n + F_1\right)} & 0 \\ 0 & e^{j2\pi\Delta\tau_{l+1}\left(\frac{B}{Tf_s}n + F_1\right)} \end{pmatrix},$$

the propagation can be described by

$$\begin{pmatrix} \underline{s}_{E_{l+1,l}}[n] \\ \underline{s}_{R_{l+1,l}}[n] \end{pmatrix} = \mathbf{P}_{l+1} \cdot \begin{pmatrix} \underline{s}_{E_{l+1,l+2}}[n] \\ \underline{s}_{R_{l+1,l+2}}[n] \end{pmatrix}. \quad (4.9)$$

The complete transfer matrix $\mathbf{M}[n]$ is the product of the single matrices

$$\mathbf{M}[n] = \mathbf{D}_{0,1} \cdot \mathbf{P}_1[n] \cdot \mathbf{D}_{1,2} \cdot \mathbf{P}_2[n] \cdot \dots \cdot \mathbf{P}_L[n] \cdot \mathbf{D}_{L,L+1} = \begin{pmatrix} M_{00}[n] & M_{01}[n] \\ M_{10}[n] & M_{11}[n] \end{pmatrix} \quad (4.10)$$

including two layers representing air ($l = 0$ and $l = L + 1$). The equivalent time function $h_e[n]$ equals:

$$h_e[n] = \frac{M_{10}[n]}{M_{00}[n]} \quad (4.11)$$

to describe the complete reflection. As shown in Figure 4.6 *right*, this function is solely multiplied with an appropriate start signal such as a set of ones in case of a virtual start at the reference plane.

4.4 Validation of Model-Based Approach

To validate the modification of the TMM and the model-based approach, measurements of an acrylic glass sample were performed. Figure 4.7 depicts the SUT. In the first step, the plate was positioned in a way that the composition of air, acrylic, and air was measured to determine the refractive index. To reduce an error propagation, an accurate result and hence a small step size of 1 μm were required. A search interval² corresponding to an optical path length of 2.0 mm to 2.7 mm resulted in a refractive index of 1.59 for the signal model of solely main reflections and 1.58 for TMM. The corresponding Rayleigh limit equaled 2.4 mm. In order to address a typical measurement scenario, the thickness was analyzed afterwards based on the refractive indices. The SUT was measured from the back in a way that its metallic label served as a reflector beneath the acrylic layer. For the processing, the evaluated refractive indices of the different algorithms were used to calculate the thicknesses. A typical estimate of the thickness (0 mm

²A rough estimate of η is required.

to 2 mm) was chosen as the search interval. The step size³ was 3.1 μm . Table 4.1 represents the evaluated thicknesses for 5 individual measurements. A standard deviation of 0 for the model of main reflections is assumed to result from the choice of the step size: for a reevaluation with 2.5 μm , it was 0.6 μm . As expected, in case of a metal substrate, the TMM has to be chosen because the results of the model of main reflections were biased. For TMM, the thickness below the Rayleigh limit was determined accurately.



Figure 4.7: Acrylic sample of a thickness of 1.5166 mm \pm 0.4%

Table 4.1: Evaluated Thickness of Acrylic Sheet Using the Model of Main Reflections and TMM

	evaluated thickness	standard deviation
model of main reflections	0.5 mm	0 μm
TMM	1.53 mm	1.3 μm

This example indicates that the model of main reflection is often sufficient for dielectric materials⁴ in air, because both variants resulted in similar refractive indices. However, in case of a conducting substrate, the amplitudes of the multiple reflections increased requiring TMM. After the validation of the model-based approach, it is compared with the alternative signal-processing approaches.

4.5 Comparison of Algorithms

For a final comparison of the signal-processing algorithms, the simulated example of section 2.5 in Figure 2.11 with optical path length of 3.5 mm and 5 mm

³To remain the computation complexity, the step size was increased as the interval width was expanded.

⁴for moderate values such as 1.8

was used. Table 4.2 represents the results evaluated by Fourier transform-based peak detection, the model-based variant and a matching pursuit decomposition of [80], which iteratively compares a single reflection with the measured signal and subtracts the evaluated portion afterwards.

As expected and discussed in section 2.5, the peak detection utilizing a rectangular window delivered biased values. While the estimation of the matching pursuit decomposition was accurate for the example above the Rayleigh limit of $\Delta r_R = 3.9$ mm, for the thinner sample, the result is significantly biased. It indicates that the superposition of the peaks cannot be neglected for smaller thicknesses. For the model-based approach search intervals of -5 mm to 5 mm and 0 mm to 10 mm were used as well as a step size of 50 μ m. It resulted in accurate values. Therefore, it is the most promising algorithm for thin layers.

Table 4.2: Evaluated Optical Path Lengths of Different Signal-Processing Algorithms

optical path length	peak detection	matching pursuit decomposition	model-based approach
5.5 mm	5.6 mm	5.5 mm	5.5 mm
3.5 mm	4.5 mm	5.0 mm	3.5 mm

Table 4.3 summarizes the previous results comparing the signal-processing methods. The model-based approach includes the multiple reflections in case of the TMM, while the remaining algorithms either neglect them or require a separate analysis of each peak. The model-based approach is the only method enabling accurate results below the Rayleigh resolution limit. A higher computation time utilizing a central processing unit (CPU) and an exhaustive search can be compensated by parallel computing on a general-purpose graphics processing unit (GP-GPU).

The model-based approach highly conforms to the principle of a maximum-likelihood receiver in data communication: the received signal, which is assumed to be superposed by additive white noise, is correlated with potential data series. As for the MUSIC algorithm in section 3.2, both are assumed orthogonal. In an approximated absence of intersymbol interference, the maximum-likelihood receiver converts into a matched filter. The ratio of signal and noise power is maximized, while the error rate is minimized. Hence, the matched filter is optimal in this regard [86]. Due to the conformity, it is not expected that potential alternative signal-processing approaches may result in more accurate estimates of the thicknesses.

Since the requirement of resolving thin layers is fulfilled, the quality of the measured results such as the measurement uncertainty is analyzed in the next chapter utilizing theoretical aspects as well as measurements.

Table 4.3: Characteristics of Signal-Processing Algorithms

	peak detection	matching pursuit decomposition	spectral estimation	model-based approach
multiple reflection	- usually neglected [85]	- analysis required [80]	- analysis required	+ implemented by TMM
thicknesses below Δr_R	- not feasible (Figure 2.10)	- inaccurate (Table 4.2)	- inaccurate (model order)	+ most accurate
computation time (CPU)	+	+	+	- (\rightarrow GP-GPU)

5. Accuracy and Precision

In the previous chapter, a model-based approach was presented to determine layer thicknesses below the Rayleigh resolution limit for a frequency-modulated continuous-wave (FMCW) setup. Utilizing high penetration depths of W band transceivers, the approach is an important first step towards novel industrial applications inspecting combinations of thick substrates and thin layers. However, the resolution is only one aspect to describe the quality of a measurement approach. An additional requirement is the reliability of the evaluated results.

Since a measured signal interferes with noise, it can be classified as a stochastic process. Exemplarily, the Gaussian probability density function (PDF) p_x of a random variable X such as a noise sample is depicted in Figure 5.1. It differentiates two important aspects to determine the reliability of measurements, the accuracy and precision. The accuracy is determined by the average bias of the result: it can be quantified as the distance between the expectation value $\mathbf{E}\{X\}$ and the reference (true) value. The precision instead classifies the repeatability of the resulting values. It is related to the width of the PDF, which inversely depends on the variance

$$\begin{aligned}\text{var}(X) &= \mathbf{E}\{(X - \mathbf{E}\{X\})^2\} \\ &= \mathbf{E}\{X^2\} - (\mathbf{E}\{X\})^2\end{aligned}\tag{5.1}$$

or its square root, the standard deviation σ . For a sharp peak, the variance is low and the precision high. For industrial applications, both, accurate and precise, results are required.

In terms of reliability, it is additionally desirable, that at least the average value of the measured quantity does not depend on the start time of the measurement. This behavior is described by the concept of a wide-sense stationary process. For many applications, this characteristic is at least required over a short period of time. Otherwise, in dependency on the start time of the measurement, different results would be observed. Wide-sense stationarity also was a requirement for spectral estimation techniques of chapter 3. For these reasons, it is assumed for the presented setup.

In this chapter, the influences of the physical components on accuracy and precision are discussed. While their impact on the bias can be compensated by the calibration procedure, the resulting noise still determines the variance of the results. Therefore, the noise characteristic is investigated. An analysis of the resulting signal-to-noise ratio provides the basis to derive the minimum theoretical

variance, the Cramér-Rao lower bound. Finally, the evaluated limit is tested for validation by simulated and measured signals.

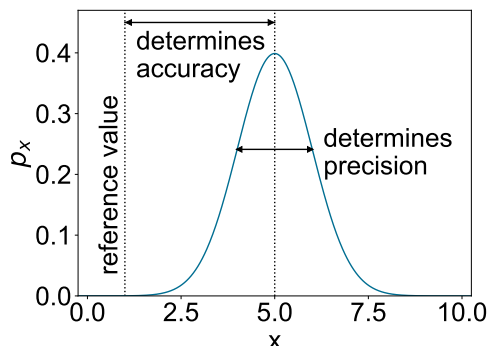


Figure 5.1: Accuracy and precision of a random variable X characterized by a biased normal probability density function

5.1 Influences of Components and Processing

Several influences caused by sample-under-test (SUT), setup, surroundings, and processing affect the accuracy and the precision of thickness measurements. In case that these effects can be described by deterministic methods, they tend to have an impact on the bias or accuracy. Influences that are characterized using stochastic methods rather affect the precision.

The block diagram of Figure 5.2 represents the setup and the preprocessing. In terms of accuracy, all components can have an influence, since their impulse responses are convoluted with the signal. One considerable example is a potential nonlinearity of the frequency modulation slope. It would result in a radio frequency that is slightly larger than the linearly interpolated value. Then, the beat signal would contain portions with a marginally higher frequency, which may shift the center of the peaks and widen them. However, the counteractive predistortion widely compensates for this kind of nonlinearity.

The influence of the geometry of the SUT can be illustrated based on the estimation of the lateral resolution in section 2.3. It was assumed, that the materials are homogeneous and the boundary surface plane-parallel at least within the illuminated area. Small deviations from this ideal may affect the accuracy of the results. Then, an average value of the complete measurement spot is evaluated such as indicated in Figure 2.4. A similar influence can be caused by material density variations, because they result in different propagation times of the beam portions. Reflections by the surroundings such as by walls and the focusing unit can cause additional peaks in the measured signal. Depending on the distances of the setup components, they may interfere with the significant reflections (by the SUT) and affect the accuracy.

However, such influences have been considered for the setup design. Due to the focusing unit of the setup, only reflections, which are originated from boundary surfaces in approximation of the Rayleigh length, are intensified. The remaining portions such as reflections caused by the setup are compensated by the calibration procedure.

The calibration procedure itself cannot only be interpreted as demodulation but also as a kind of deconvolution. The measured signal is divided by the conducting plate measurement (equation 2.19) resulting in an ideal peak in the frequency domain. Therefore, the combination of conducting plate and empty room compensates for a significant fraction of such influences in approximation of reference plane and hence Rayleigh length.

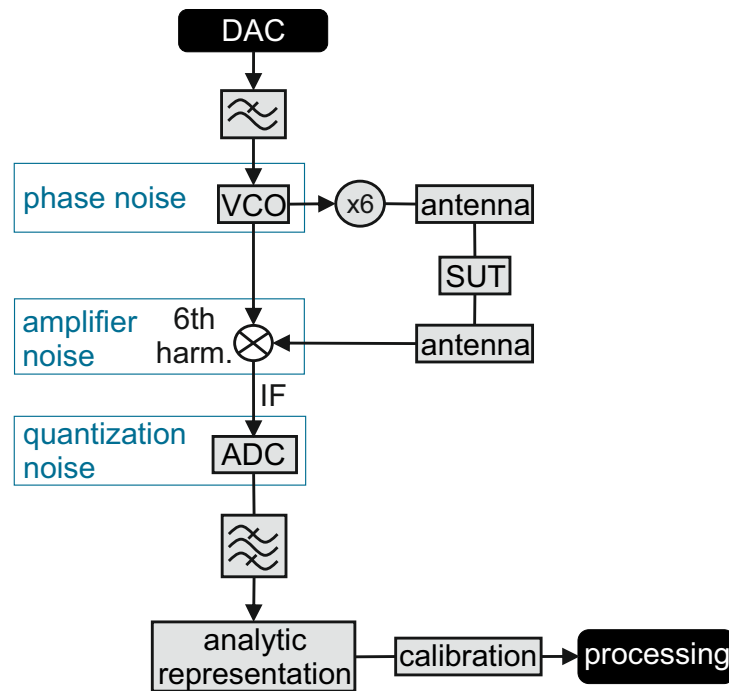


Figure 5.2: Block diagram of measurement system and processing indicating noise sources: digital-to-analog converter (DAC), lowpass filter, voltage-controlled oscillator (VCO), frequency multiplication (x6), a mixer using 6th harmonic (6th harm) of one input, analog-to-digital converter (ADC), and bandpass filter to prepare for (pre)processing, IF: intermediate frequency

In terms of precision, different influences have been identified such as phase noise by the voltage-controlled-oscillator [54], thermal noise by all components, noise resulting from the analog-to-digital conversion (ADC) [54], [55], and amplifier [55]. The one of quantization is assumed to be negligibly low due to the 12 bit dynamic range of the ADC. Depending on the system configuration and measurement rates, averaging of measured signals enables to reduce of the resulting noise. Previous studies [54], [55], [87], [88] have shown that phase noise has a decisive influence on precision. It is therefore examined in the next section using simulations.

5.2 Influence of Phase Noise

To analyze the influence of phase noise φ_n , different simulations have been performed. Its impact can be included in the description of the transmitted signal as

$$\underline{s}_t(t) = \exp\left(j2\pi F_1 t + j\pi \frac{B}{T} t^2 + j\varphi_n(t)\right) \quad (5.2)$$

with start frequency F_1 , time t , bandwidth B , and duration T for the linearly frequency-modulated oscillation [54]. Hence, the intermediate frequency signal results in

$$s_{IF}[n] = \sum_l a_l \cos\left(2\pi f_{b,l} \frac{n}{f_s} + \phi_{\tau_l} + \Delta\varphi_n\left(\frac{n}{f_s}, \tau_l\right)\right) \quad (5.3)$$

with amplitude of the l^{th} reflection a_l , time index $n \in \{0, 1, \dots, N - 1\}$, beat frequency $f_{b,l}$, and zero phase ϕ_{τ_l} . The phase is disturbed by the resulting phase noise difference:

$$\Delta\varphi_n\left(\frac{n}{f_s}, \tau_l\right) := \varphi_n\left(\frac{n}{f_s}\right) - \varphi_n\left(\frac{n}{f_s} - \tau_l\right) \quad (5.4)$$

in comparison to the ideal signal in equation 2.8.

The PDF of the phase noise was not determined for the presented setup. However, distinctive examples were simulated and compared. Under the assumption of additive white Gaussian phase noise (AWGPN), a simulated signal of a conducting plate is depicted in Figure 5.3 *left*. After the calibration, its amplitude equaled one. For the variance, an arbitrary value but high of 0.1 was chosen.

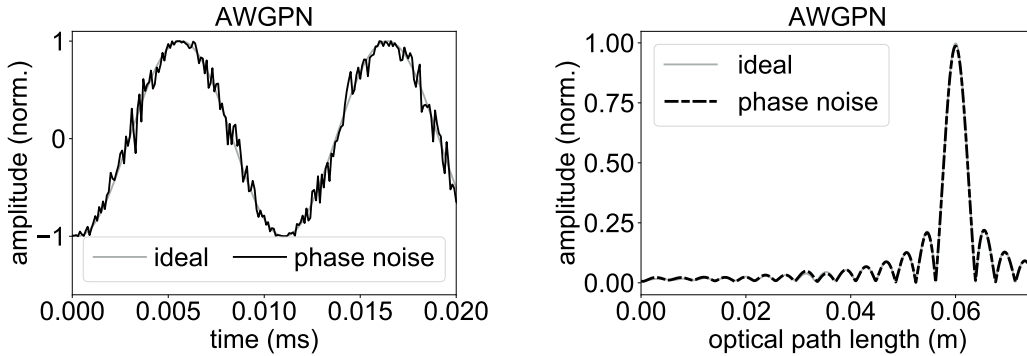


Figure 5.3: *left:* simulated signal of one conducting reflector at 0.6 m disturbed by AWGPN, *right:* comparison of peaks under the presence and without phase noise

Equation 5.3 indicates, that an additive phase portion may influence the measured signal in a way, that the current frequency of the beat signal might be larger for certain time samples and lower for other ones. However, due to the fast fluctuations of the noise, its average value for small section of the signal equals zero. Hence, the width and center frequency of the main peak in Figure 5.3 *right* remain unchanged.

Figure 5.4 depicts the peaks exemplarily for other PDFs: the Rayleigh phase noise (*left*) represents a distribution with a biased mean value: for variance $\frac{4-\pi}{2}\sigma_R^2$ with scale parameter σ_R , it equals $\sigma_R\sqrt{\pi/2}$. The amplitude of the peak is reduced in comparison to the ideal signal. The peak in Figure 5.4 *right* is affected by Brownian motion phase noise representing fluctuations, which can be modeled as a recursive memory similar to a closed feedback loop. Due to calculating the phase difference of equation 5.3, the bias and feedback are both eliminated for Rayleigh and Brownian motion phase noise.

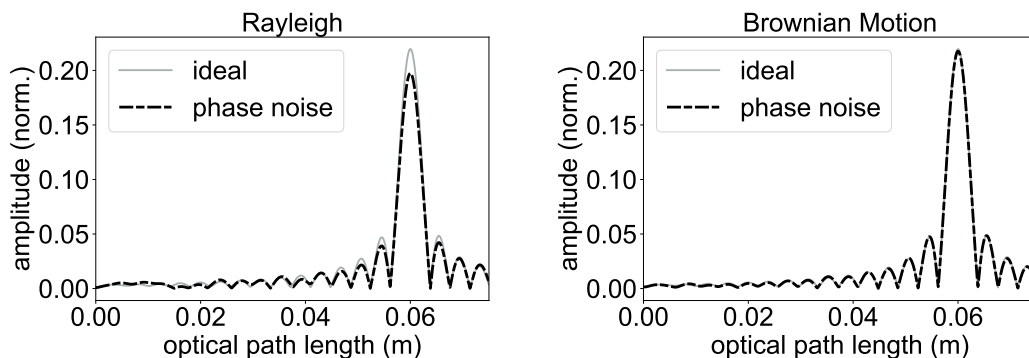


Figure 5.4: Comparison of peaks without (ideal) and under the presence of *left*: Rayleigh, *right*: Brownian motion phase noise

Figure 5.5 shows a histogram of amplitude fluctuations caused by the AWGPN of Figure 5.3 *left*. To analyze its distribution, a hypothesis test has to be chosen. One typical option is calculating the p value, which can be used to strengthen or weaken an assumption. For this purpose, a hypothesis is assumed to be true and its statistical significance is calculated. To interpret the results, a significance level has to be chosen. Typical values are 0.01 or 0.05 [89]. If the calculated significance, the p value, is smaller than the chosen level, the hypothesis is rejected, or else classified as significant. However, the p value is not a definitive test whether an assumption is true or false [89]. In this case, the histogram indicates, that the amplitude fluctuation could be either Gaussian or Laplace-shaped. Using the SciPy hypothesis testing [90], they are rejected to be one of both due to p values lower than $3 \cdot 10^{-8}$ contradicting the assumption of additive white Gaussian noise (AWGN) which was presumed in [88]¹ for instance.

The distance fluctuations of 500 simulations were analyzed resulting in the histogram in Figure 5.5 *right*. Testing for AWGN resulted in p values of 0.71, 0.62, and 0.76 for AWGPN, Rayleigh and Brownian motion phase noise using the SciPy hypothesis test [92]. Therefore, the measured results are assumed to be normally distributed for the resulting phase noise of the setup as well. After these theoretical considerations, the resulting noise of the measured signal is analyzed in the next section.

¹The authors of [88] apply estimations of the variance which were derived under the assumption of AWGN. However, this requirement is not explicitly mentioned [88] but in their reference [91].

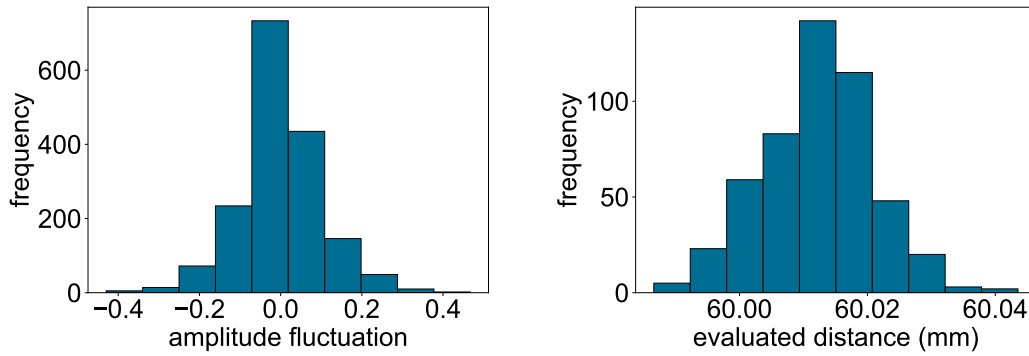


Figure 5.5: *left:* histogram of amplitude difference by AWGPN, *right:* histogram of 500 evaluated distances disturbed by AWGPN

5.3 Analysis of Resulting Signal Noise

Due to the presence of noise, the measured signal corresponds to a stochastic process. To analyze the influence of the noise on the results, two characteristics have to be estimated, the signal-to-noise ratio and the PDF. For the estimation, two different sets of observations are utilized, the sample function and the ensemble characteristic. In case of FMCW thickness determinations, a sample function corresponds to a single measurement signal as shown in Figure 5.6. To create an ensemble, a statistic of several measurement signals has to be generated. It then corresponds to a set of data points of one time index.

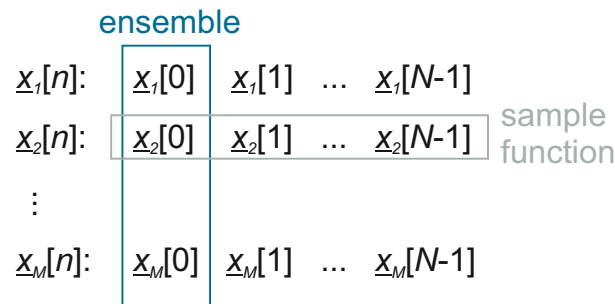


Figure 5.6: Ensembles and sample functions $\underline{x}_1, \underline{x}_2, \dots, \underline{x}_M$ with time index $n \in \{0, 1, \dots, N-1\}$

In terms of the spectrum estimation algorithms, the PDF and the signal-to-noise-ratio were required to simulate the noise and to generate sample functions of the signals. Characteristic sample functions are also included in the resulting reference signals for the comparison of different optimization algorithms in chapter 6. In terms of analyzing the theoretical variance and hence, the precision, the characteristics of the ensembles are required.

In case of an ergodic process, the mean value of a sample function and the ex-

pected value of an ensemble for any time index are equal with a probability of one. This implies that the mean value does not depend on the starting point of the measurement. Therefore, ergodicity requires the characteristic of wide-sense stationary, which has been assumed for this FMCW setup. A benefit in case of ergodic processes is the simplified calculation of characteristic values: the expected value of an ensemble can be estimated by only observing a randomly chosen sample function. Hence, the sample functions generated to compare the spectrum estimation algorithms also served as estimates for the ensemble characteristics. However, since for this work, a statistic of 500 signals could be directly recorded, the characteristic of ergodicity can be tested.

In the next section, a statistic of ensembles and then a set of samples functions are analyzed for their mean value.

5.3.1 Ensemble Characteristic

Measuring a conducting plate at the calibration position enables the estimation of the noise characteristics. The ideal real signal is assumed to be interfered with additive noise resulting in the sum $x_m[n]$. Due to the calibration, the entries of the analytic representation of the ideal signal $\underline{x}_m[n]$ would equal 1 for all time indices. Under the assumption, that fluctuations are mainly caused by additive noise, the variations can be used to estimate its characteristics. A statistic of $M = 500$ measurements was performed. For each time index n , mean value and variance were calculated. The time-domain ensemble signal-to-noise ratio SNR_E is the average value of the single $\text{SNR}_{n,E}$,

$$\text{SNR}_{n,E} = \frac{1}{M} \sum_{m=1}^M \frac{|\underline{x}_m[n]|^2}{|1 - \underline{x}_m[n]|^2}. \quad (5.5)$$

In Figure 5.7, the mean value (blue) and standard deviation (gray surroundings) are depicted as functions of the time indices n . Their values are determined by the left y-axis. The respective quotient of squared mean value and variance resulted

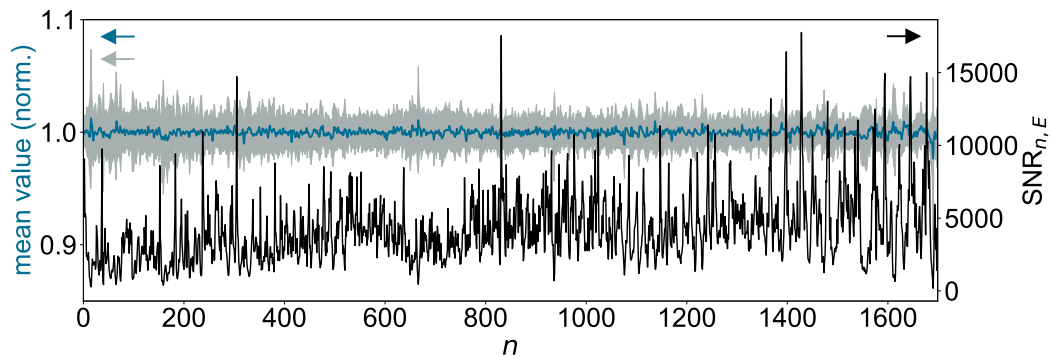


Figure 5.7: Left y-axis: ensemble average (blue) and standard deviation (gray), right y-axis: $\text{SNR}_{n,E}$ (black) using 500 individual measurements of a conducting plate

in the $\text{SNR}_{n,E}$ (right y-axis). An average value of $\text{SNR}_E = 4133$ was evaluated, based on it. The mean values of all ensembles approached a value of one.

To analyze the noise distribution, Figure 5.8 *left* depicts the histogram of one randomly chosen and representative example, the 1301st time index, indicating the Gaussian bell shape. A quantile-quantile plot to test the hypotheses of normal distribution in Figure 5.8 *right* can be used to graphically analyze the data. It compares a theoretical normal distribution with the one of the data. For this purpose, the single amplitude values are ordered and plotted according to the theoretical quantity of a Gaussian distribution. The linear rise indicated that the distributions are likely to be equal strengthening the assumption.

To avoid individual graphic tests for each time index, the p values introduced in section 5.2 was calculated for each point. Their average was calculated afterwards. Even though the average of p values does not necessarily conform to a p value [93] anymore, it enables to indicate an overall tendency. Testing for a normal distribution, it resulted in a value of 0.27 applying the SciPy hypothesis testing [90]. The p value indicates the assumption of AWGN, because for such high levels, the hypotheses cannot be rejected.

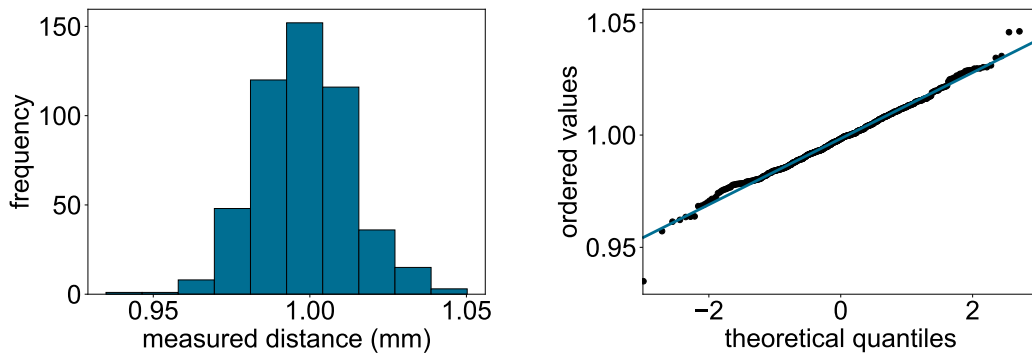


Figure 5.8: *left* histogram and *right* quantile-quantile plot of the real part of the measured signal for the 1301st time index using hypothesis testing [90], tested for normal distribution

Generating an analytic representation of a measurement signal within the pre-processing procedure, the noise is inevitable transformed as well. Figure 5.9 depicts the quantile-quantile plot of the calculated imaginary part, which due to the linear rise appears to be normal-distributed as well. The average p value equaled 0.55. However, real and imaginary parts of the noise are dependent: their Fourier-transformed are $\frac{\pi}{2}$ phase shift versions of each other corresponding to the requirement for the generation of the analytic representation of section 2.4. Therefore, the time-domain representations are related by the Hilbert transform. Table 5.1 summarizes the estimates of the evaluated quantities.

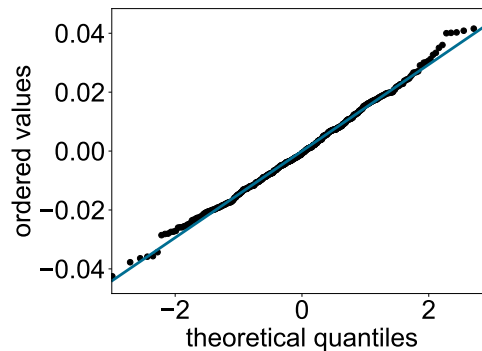


Figure 5.9: Quantile-quantile plot of the imaginary part, tested for normal distribution

Table 5.1: Analysis of Ensemble Characteristic of the Resulting Noise

SNR_E	4133 (36.2 dB)
mean value	$1 (\pm 3.34 \cdot 10^{-4})$
average p value for AWGN	0.27 (real part) 0.55 (imaginary part)

5.3.2 Sample Function Characteristic

Based on the set of measurements of the conducting plate, also the sample function characteristic was analyzed. For the m^{th} sample function x_m , the corresponding time-domain signal-to-noise ratio SNR_S is calculated as the average value of $\text{SNR}_{m,S}$ with

$$\text{SNR}_{m,S} = \frac{1}{N} \sum_{n=0}^{N-1} \frac{|\underline{x}_m[n]|^2}{|1 - \underline{x}_m[n]|^2}. \quad (5.6)$$

Figure 5.10 depicts the single observations. The mean values of the single sample functions are determined by the left y-axis. They approached a value of one.

A hypothesis test [90] was performed testing for normal distribution resulting in an average p value of 0.0094, which is smaller than the one of the ensemble. Since it is close to the typical significant levels of 0.01, it is classified as not rejected in this context. The quantile-quantile plot of the randomly chosen 5th sample function is depicted in Figure 5.11 representing a conformity with AWGN as well. The results are summarized in Table 5.2.

One variant of ergodicity, the ergodicity of the means, requires sample functions and ensembles to exhibit the same mean values [94]. Both approaching a value of 1 for all single observations, indicates this characteristic. In addition, the variances are approaching similar values of $3.3 \cdot 10^{-4}$ and $3.4 \cdot 10^{-4}$ for ensembles and sample functions, respectively.

Based on the evaluated SNR, the theoretical precision is analyzed next.

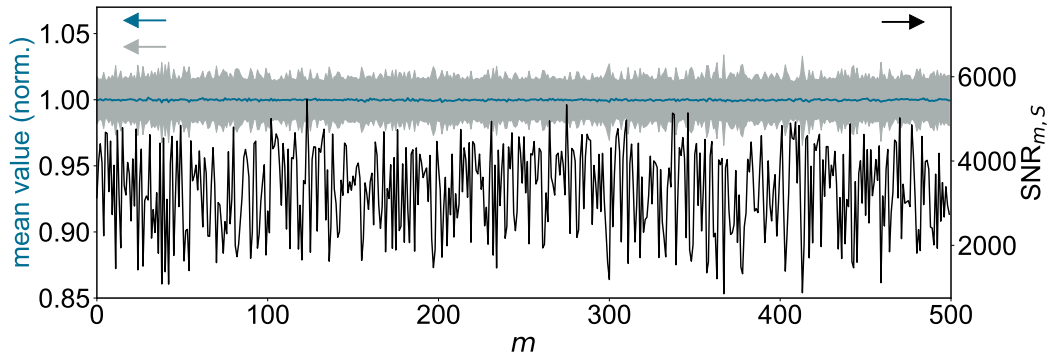


Figure 5.10: left y-axis: average value (blue) and standard deviation (gray), right y-axis: $\text{SNR}_{m,s}$ (black) of each measured sample function

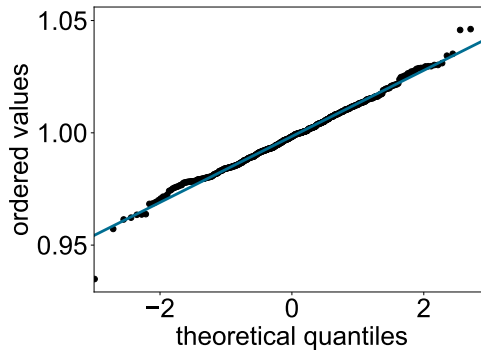


Figure 5.11: Quantile-quantile plot of the 5th measurement signal tested for normal distribution

Table 5.2: Analysis of Sample Function Characteristic of the Resulting Noise

SNR_S	3310 (35.2 dB)
mean value	$1 (\pm 3.42 \cdot 10^{-4})$
average p value for AWGN	0.0094 (real part) 0.0094 (imaginary part)

5.4 Limitation of Precision

For nondestructive testing, the reproducibility or precision of measured values is an important aspect for reliable results. The term is related to standard deviation or variance. Estimation theory allows a theoretical analysis. One quantity is the Cramér-Rao lower bound (CRLB), which describes the theoretical minimum of the variance for all unbiased estimators. In [53], [95], an estimation of the bound is used, which is not considering the dependency of beat frequency and zero phase of a reflection (represented in equation 2.8). Since both quantities are processed

sequentially, the evaluated limitation nevertheless may result in rather appropriate estimates. In [96], a CRLB is estimated for two-tone FMCW reflectometry including this dependency.

For FMCW thickness measurements, the bound is derived in the following section considering the relation of beat frequency and zero phase as well, because both quantities are simultaneously processed [6]. For simplicity, in the first step, distance evaluations are examined. Afterwards the results are extended for thickness determinations. It is assumed, that the exact amplitudes of the reflections are a priori given. For other cases, they have to be classified as variable, which can affect the bound in a way that higher variances will be observed. Furthermore, multiple reflections are not considered to simply the deviation. Due to their low amplitudes, they often can be neglected. However, their influence is discussed in the end of this chapter.

5.4.1 Distance Measurements

For simplicity, the real representation of the measured signal is used. This variant is justified because the actually measured signal is a real quantity. A distance which has to be evaluated depends on the time delay τ , which is proportional to the optical path length between reflector and reference plane. The ideal measured signal² results in

$$s_{IF}[n, \tau] = a \cos\left(2\pi \frac{B}{T f_s} \tau n + 2\pi F_1 \tau\right) \quad \text{for } 0 < \tau < \frac{T}{2B} f_s \quad (5.7)$$

with amplitude a . However, the signal interferes with noise. Under the assumption of AWGN $\omega[n]$ with the variance σ_n^2 , the resulting signal $x[n]$ equals

$$x[n] = s_{IF}[n, \tau] + \omega[n]. \quad (5.8)$$

Subtracting $s_{IF}[n, \tau]$ from both sides, the PDF yields:

$$p_x(\mathbf{x}, \tau) = \frac{1}{(2\pi\sigma_n^2)^{\frac{N}{2}}} \exp\left(-\frac{1}{2\sigma_n^2} \sum_{n=0}^{N-1} (x[n] - s_{IF}[n, \tau])^2\right) \quad (5.9)$$

with $\mathbf{x} = (x[0], x[1], \dots, x[N-1])^T$.

One requirement for the CRLB is the regularity condition, which is used in the derivation in [91]. In case it is fulfilled, an integration and derivative process can be substituted by each other simplifying the calculation. The expectation value \mathbf{E} of the logarithmic derivative of the PDF with respect to the PDF has to equal

²The signal $s_{IF}[n, \tau]$ corresponds to $s_{IF}[n]$ of equation 2.8 in case of a single reflection. Since the dependency on τ is significant in the following sections, this notation is preferred.

0,

$$\begin{aligned}
& \mathbf{E}\left\{\frac{\partial \ln(p(\mathbf{x}, \tau))}{\partial \tau}\right\} \\
&= -\frac{1}{\sigma_n^2} \sum_{n=0}^{N-1} (\mathbf{E}\{x[n]\} - a \cos(2\pi \frac{B\tau}{Tf_s} n + 2\pi F_1 \tau)) \\
&\quad \cdot ((2\pi \frac{B}{Tf_s} n + 2\pi F_1) \cdot a \sin(2\pi \frac{B}{Tf_s} \tau n + 2\pi F_1 \tau)) \\
&= 0,
\end{aligned} \tag{5.10}$$

which is guaranteed, since the expectation value $\mathbf{E}\{x[n]\}$ equals $s_{IF}[n, \tau]$. The CRLB for an arbitrary signal is derived in [91]:

$$\text{var}(\hat{\tau}) \geq \frac{\sigma_n^2}{\sum_{n=0}^{N-1} (\frac{\partial s_{IF}[n, \tau]}{\partial \tau})^2}, \tag{5.11}$$

resulting in

$$\text{var}(\hat{\tau}) \geq \frac{1}{4\pi^2 \frac{a^2}{\sigma_n^2} \sum_{n=0}^{N-1} (\frac{B}{Tf_s} n + F_1)^2 \sin^2(2\pi \frac{B}{Tf_s} \tau n + 2\pi F_1 \tau)} \tag{5.12}$$

for the present problem [6]. The notation $\hat{\cdot}$ highlights that the respective quantity is estimated. The parameters of the setup influence the bound as well as the ratio a^2/σ_n^2 . The maximum value of a equals 1. It can be observed when measuring the conducting plate. Then, the ratio a^2/σ_n^2 equals the ensemble signal-to-noise ratio SNR_E and the lowest value for the variance is observed. The condition $0 < \tau < Tf_s/(2B)$ is required, because, otherwise the influence of the frequency is lower and more difficult to identify. Therefore, positions close to 0 as well as 3.19 m are excluded.

In Figure 5.12, the CRLB is depicted as a function of the distance for different numbers of samples N . The relation can be interpreted as follows: with increasing N , the amount of received information is grown and hence, the variance is reduced. Moreover, Figure 5.12 shows that the variance is assumed to vary more strongly in approximation of the excluded positions 0 and 3.19 m than for points in between them. The calibration procedure, which results in positions close to zero, might therefore not be optimal, because rather high fluctuation can be expected in approximation of the reference plate position which then equals zero. On the one hand, larger distances could shift the values to a region with a rather constant precision. On the other hand, such a shift would significantly downgrade the accuracy of the results.

5.4.2 Thickness Measurements

For thickness measurements and for neglecting multiple reflections, the number of significant reflections $L + 1$ can be determined based on the number of layers L . The sum $x[n, \boldsymbol{\tau}]$ of AWGN $\omega[n]$ and ideal signal $s_{IF}[n, \boldsymbol{\tau}]$ equals

$$x[n, \boldsymbol{\tau}] = s_{IF}[n, \boldsymbol{\tau}] + \omega[n] = \sum_{l=0}^L a_l \cdot \cos(2\pi \frac{B}{Tf_s} \tau_l n - 2\pi F_1 \tau_l) + \omega[n]. \tag{5.13}$$

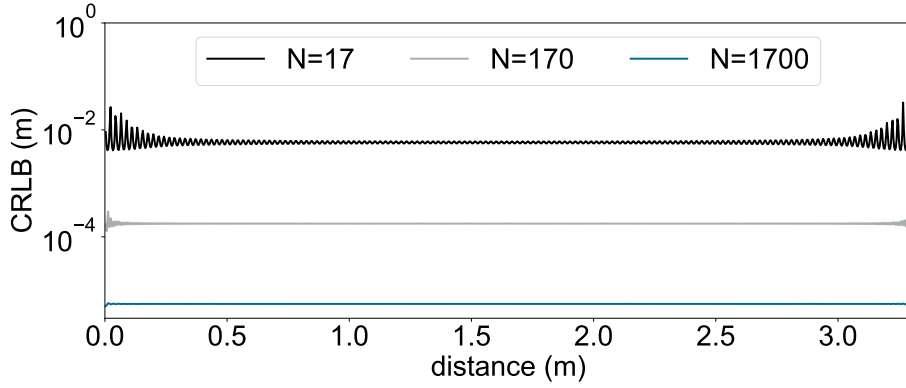


Figure 5.12: CRLB (standard deviation) as a function of the optical path length between object and calibration plane, number of samples N varies

The term $\boldsymbol{\tau} = (\tau_0, \tau_1, \dots, \tau_L)^T$ should be estimated while the amplitudes a_l are again assumed to be given. Analog to equations 5.9 and 5.10, the regularity condition is fulfilled for each $\tau_0, \tau_1, \dots, \tau_L$.

In case that more than one quantity is estimated the Fischer information matrix $\mathbf{I}(\boldsymbol{\tau})$ has to be calculated [91]. The diagonal elements of the inverted matrix correspond to the variances of the estimated quantities. The $(l_1, l_2)^{\text{th}}$ element of $\mathbf{I}(\boldsymbol{\tau})$ is defined by

$$[\mathbf{I}(\boldsymbol{\tau})]_{l_1 l_2} = \frac{1}{\sigma_n^2} \sum_{n=0}^{N-1} \frac{\partial s_{IF}[n, \boldsymbol{\tau}]}{\partial \tau_{l_1}} \cdot \frac{\partial s_{IF}[n, \boldsymbol{\tau}]}{\partial \tau_{l_2}} \quad (5.14)$$

for $l_1, l_2 \in \{0, 1, \dots, L\}$. For the calculation, two cases can be separated: diagonal $l_1 = l_2$ and nondiagonal $l_1 \neq l_2$ elements.

For the diagonal entries, the partial derivation with respect to the delay τ_{l_1} was squared similar to equation 5.11:

$$\begin{aligned} [\mathbf{I}(\boldsymbol{\tau})]_{l_1 l_1} &= \frac{1}{\sigma_n^2} \sum_{n=0}^{N-1} (a_{l_1} (2\pi \frac{B}{T f_s} n + 2\pi F_1) \\ &\quad \cdot (-\sin(2\pi \frac{B}{T f_s} \tau_{l_1} n + 2\pi F_1 \tau_{l_1})))^2 \\ &= \frac{1}{2\sigma_n^2} \sum_{n=0}^{N-1} (a_{l_1}^2 (2\pi \frac{B}{T f_s} n + 2\pi F_1)^2 \\ &\quad \cdot (1 - \cos(4\pi \frac{B}{T f_s} \tau_{l_1} n + 4\pi F_1 \tau_{l_1}))) \\ &\stackrel{\text{(A)}}{\approx} \frac{1}{2\sigma_n^2} \sum_{n=0}^{N-1} a_{l_1}^2 \left(2\pi \frac{B}{T f_s} n + 2\pi F_1 \right)^2 \\ &\stackrel{\text{(B)}}{\approx} \frac{2\pi^2 a_{l_1}^2}{\sigma_n^2} \left(\frac{1}{3} \left(\frac{B}{T f_s} \right)^2 N^3 + \frac{B}{T f_s} F_1 N^2 \right). \end{aligned} \quad (5.15)$$

Approximation (A) was based on the observation, that the sum of cosines is significantly smaller than the remaining sum terms. Therefore, the estimate from [91], [97] was used:

$$\frac{1}{N} \sum_{n=0}^{N-1} n^m \cos(4\pi f_0 n + 2\phi) \approx 0 \quad (5.16)$$

for $m \in \{0, 1, 2\}$ and digital frequency f_0 , which is not located close to 0 or 0.5. Therefore, again the approximation of positions 0 and 3.19 m are excluded. After factoring out and applying sum formulas, the insignificant terms were neglected for approximation (B).

For nondiagonal elements, the partial derivatives with respect to the delay τ_{l_1} and τ_{l_2} were multiplied:

$$\begin{aligned} [\mathbf{I}(\boldsymbol{\tau})]_{l_1 l_2} &= \frac{1}{\sigma_n^2} \sum_{n=0}^{N-1} (a_{l_1} a_{l_2} (2\pi \frac{B}{T} f_s n + 2\pi F_1)^2 \\ &\quad \cdot \sin(2\pi \frac{B}{T f_s} \tau_{l_1} n + 2\pi F_1 \tau_{l_1}) \\ &\quad \cdot \sin(2\pi \frac{B}{T f_s} \tau_{l_2} n + 2\pi F_1 \tau_{l_2})) \\ &\stackrel{(C)}{\approx} 0. \end{aligned} \quad (5.17)$$

For (C), the multiplication of two sine terms resulted in a cosine term, which again was negligible in comparison to the diagonal elements with higher values (as in equation 5.16).

The combined Fischer matrix was approximated as:

$$\mathbf{I}(\boldsymbol{\tau}) \approx \begin{pmatrix} [\mathbf{I}(\boldsymbol{\tau})]_{00} & 0 & \dots & 0 \\ 0 & [\mathbf{I}(\boldsymbol{\tau})]_{11} & \dots & 0 \\ \vdots & \ddots & \ddots & \vdots \\ 0 & 0 & \dots & [\mathbf{I}(\boldsymbol{\tau})]_{LL} \end{pmatrix}. \quad (5.18)$$

For a diagonal matrix, its inverse is diagonal as well. The diagonal entries are the inverted elements of $\mathbf{I}(\boldsymbol{\tau})$:

$$[\mathbf{I}(\boldsymbol{\tau})^{-1}]_{ll} \approx 1/[\mathbf{I}(\boldsymbol{\tau})]_{ll}. \quad (5.19)$$

The approximated minimum variance of the l^{th} reflection equals

$$\text{var}(\hat{\tau}_l) \geq 1/[\mathbf{I}(\boldsymbol{\tau})]_{ll} \approx \frac{1}{\frac{2\pi^2 a_l^2 N^2}{\sigma_n^2} (\frac{1}{3} (\frac{B}{T f_s})^2 N + \frac{B}{T f_s} F_1)}. \quad (5.20)$$

For thickness measurements, the variance of the difference $\tau_{l_2} - \tau_{l_1}$ is relevant. Under the assumption that both positions are stochastic independent, the combined variance $\text{var}(\hat{\tau}_{l_2-l_1})$ results in

$$\text{var}(\hat{\tau}_{l_2-l_1}) = \text{var}(\hat{\tau}_{l_1}) + \text{var}(\hat{\tau}_{l_2}). \quad (5.21)$$

The transformation of time delay $\tau_{l_1 l_2}$ to optical path length $d_{l_1 l_2}$ is linear, and hence, the factor is squared in terms of variance [91]

$$\text{var}(\hat{d}_{l_2-l_1}) = \text{var}(\hat{\tau}_{l_2-l_1}) \cdot \frac{c_0^2}{4}. \quad (5.22)$$

Then, the assumed minimum variance for FMCW thickness measurements, the CRLB, corresponds to $\frac{\text{var}(\hat{d}_{l_2-l_1})}{\eta^2}$.

The amplitudes of multiple reflections are usually much smaller than the ones of the main portions. Since the amplitudes are included in equation 5.20 as squares, their influence is further reduced. However, in case they are significant, they would increase the amount of processed information, which is assumed to reduce the variance.

5.5 Precision of Simulations and Measurements

The previously evaluated CRLB for the precision is validated by simulations and measurements in the following sections. The analysis is separated into distance and thickness measurements. Besides the model-based approach, alternative signal-processing techniques are applied to compare the respective standard deviations to identify the most precise method and to compare the values with the bound.

5.5.1 Distance Measurements

For both simulations and measurements, a statistic of 500 individual signals was generated. Three different signal-processing algorithms to evaluate distances were compared: Fourier transform-based peak detection introduced in section 2.5, the model-based approach of chapter 4, and an additional variant based on the current phase [53] of the signal. Peak detection solely processes the beat frequency information. The phase evaluation variant utilizes this peak as an initial value to approach the frequency by phase information. Since the modeled signals depend on both, the model-based approach uses the complete amount of information and, therefore is expected to result in the highest precision.

For simulations and measurements, a conducting sheet reflector at the optical path length 0 mm was analyzed. This position was chosen, because potential influences such as a nonlinear slope of the frequency modulation are compensated by the predistortion and preprocessing. Moreover, not any adjustment is required, because the plate is already positioned in the reference plane after the calibration. The evaluated distances³ are depicted in Figure 5.13.

For peak detection and the phase evaluation, the Chirp-Z transform [62] was applied, to calculate the frequency spectrum. Instead of adding zeros to the time-domain signal and computing the discrete Fourier transform, the Chirp-Z

³The values vary from the ones in [6] because a different value of the SNR was used.

transform enables to determine only a part of this interpolated spectrum for instance the region-of-interest. Thus, a small distance between calculated frequency points can be achieved without exceeding the available storage. The chosen distance of 0.075 Hz corresponded to an optical path length of 50 nm. Such small values are required to accurately determine small variations and to reduce the effect of rasterization.

For the model-based approach, the same step size of 50 nm was chosen to enable a comparison of the results. The search interval was -1 mm to 1 mm. The evaluated values of the simulations in Figure 5.13 *left* fluctuate much lower in amplitude than the ones of the measurements in 5.13 *right*. As a result, the variances of the simulations in Table 5.3 are lower than the ones of the measurements in Table 5.4.

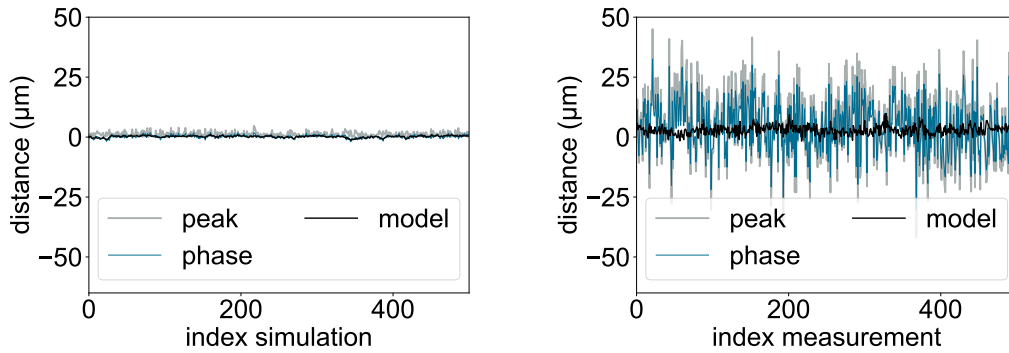


Figure 5.13: Statistic of 500 distances based on *left*: simulated, *right*: measured signals, peak detection (peak), additional phase evaluation (phase), model-based approach (model)

For simulations and measurements, the model-based approach resulted in the lowest standard deviation, and hence, the highest precision. The accuracy of evaluating simulated signal is higher than the one of the measured data. While the peak detection results in the lowest bias for the simulations, the method showed the highest value for the measurements.

Table 5.3: Precision of Distance Evaluations based on Simulations at Optical Path Length 0 mm

	mean value	standard deviation
distance and CRLB	0 mm	0.22 μm
model-based approach	316 nm	0.28 μm
peak detection	34 nm	1.51 μm
phase evaluation	303 nm	0.56 μm

Table 5.4: Precision of Distance Evaluations based on Measurements at Optical Path Length 0 mm

	mean value	standard deviation
model-based approach	2.91 μm	1.91 μm
peak detection	5.39 μm	14.80 μm
phase evaluation	3.89 μm	10.70 μm

Originally, the model-based approach was introduced to expand the thickness evaluation for thinner layers. Nevertheless, it shows that it also improves the accuracy and precision of distance measurements. In terms of the evaluated CRLB, the estimated value serves as a lower limit for both measurement and simulation, even though the distance of 0 mm was excluded for the derivation.

5.5.2 Thickness Measurements

In order to keep the influence of the side lobes on the result of the evaluation low, an SUT with a thickness that is significantly larger than the Rayleigh limit of 3.9 mm was selected. Figure 5.14 shows the chosen Pertinax layer with a thickness of 6.28 mm. Based on the frequency spectrum, amplitude values of $a_1 = 0.31$ and $a_2 = -0.13$ were obtained. The model-based approach estimated a refractive index of 1.8.

**Figure 5.14:** Photograph of the Pertinax sample-under-test

Then, an SUT with an optical path length of 11.34 mm and the determined amplitudes was simulated and evaluated based on the different algorithms. The resulting thicknesses are depicted in Figure 5.15. The phase evaluation method of [53] solely supports one reflector and hence was not processed for this thickness analysis. In contrast to the distance measurements, the differences between simulations and measurements are insignificant. Thicknesses evaluated by peak detection tend to be slightly higher than the ones of the model-based approach. The results⁴ are summarized in Tables 5.5 and 5.6.

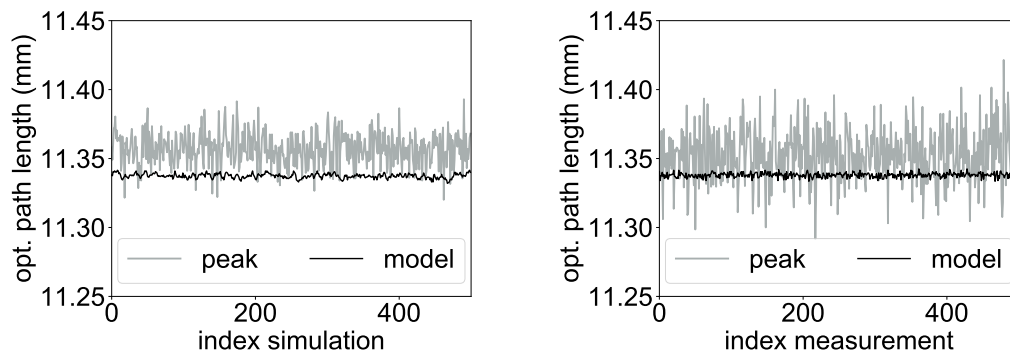


Figure 5.15: Statistic of 500 optical path lengths *left*: simulated, *right*: measured signals, peak detection (peak), model-based approach (model)

Table 5.5: Precision of Thickness Evaluations based on Simulations of Optical Path Length 11.34 mm

	mean value	standard deviation
optical path length and CRLB	11.34 mm	1.85 μm
model-based approach	11.34 mm	1.93 μm
peak detection	11.36 mm	11.9 μm

Table 5.6: Precision of Thickness Evaluations based on Measurements of Optical Path Length 11.34 mm

	mean value	standard deviation
model-based approach	11.34 mm	1.68 μm
peak detection	11.35 mm	19.76 μm

Comparing the values resulting from simulated and measured data, the model-based approach resulted in a lower standard deviation and a higher accuracy.

⁴In [6], the value of the SNR differs which leads to different results.

At the expense of a higher computational load, this method not only expands the resolution, but also improves these two aspects. Even though the thickness is clearly larger than the Rayleigh limit of 3.9 mm, the mean value of peak detection is slightly biased.

It is notable, that the standard deviation of the measured thicknesses of 1.68 μm is slightly lower than the evaluated CRLB of 1.85 μm for the model-based approach. To analyze this observation, it has to be considered, that the bound was derived in equation 5.21 under the assumption of independent reflector positions. For that case, the variance of the difference should equal the sum of the single variances. The comparison

$$\begin{aligned} \text{var}(\hat{d}_{l_2-l_1}) &= 2.83 \cdot 10^{-12} \text{ m}^2 \\ \text{var}(\hat{d}_{l_1}) + \text{var}(\hat{d}_{l_2}) &= 8.63 \cdot 10^{-12} \text{ m}^2 + 4.16 \cdot 10^{-12} \text{ m}^2 \end{aligned} \quad (5.23)$$

indicates inequality and hence a certain degree of stochastic dependency. For simulation instead, an approximate equality

$$\begin{aligned} \text{var}(\hat{d}_{l_2-l_1}) &= 3.81 \cdot 10^{-12} \text{ m}^2 \\ \text{var}(\hat{d}_{l_1}) + \text{var}(\hat{d}_{l_2}) &= 0.55 \cdot 10^{-12} \text{ m}^2 + 3.33 \cdot 10^{-12} \text{ m}^2 \end{aligned} \quad (5.24)$$

can be observed. Therefore, stochastic independence is indicated.

The reasons for the obtained discrepancy cannot be clearly determined. One aspect may be multiple reflections. They were neglected but are in fact functions of both positions. However, even for measurements, the derived CRLB is a rather accurate estimate of the standard deviation. For comparison, in [53], the value determined by measurements was approximately 5 times larger than their evaluated bound.

The CRLB delivers an estimate of the precision depending on the amplitude of the signal portions or rather refractive indices of the corresponding materials. Therefore, it enables an estimation of the minimum variances of different layer composition. For future applications, it could be a basis to estimate in advance, whether a required precision can be theoretically fulfilled for novel applications. Moreover, it allows monitoring the measured results, since far higher variances than the CRLB may indicate the presence of error sources.

For industrial applications, not only accurate and precise results are necessary. Often specific timing requirements are given by the production lines. Hence, an option to substitute the computationally intensive exhaustive search might be beneficial. For this purpose, different optimization algorithms are analyzed in the next chapter. Since besides the SNR of the setup, also the signal processing was shown to determine the quality of the results, both the accuracy and the precision are also important criteria to compare the potential of respective optimization approaches.

6. Optimization

To evaluate the propagation times of the respective beam portions and hence thicknesses of layers, the beat frequencies of the frequency-modulated continuous-wave (FMCW) signal's oscillations have to be determined. In the previous chapters, a signal-processing approach was presented to resolve thicknesses below the Rayleigh resolution limit by fitting a model to conform the measured signal. The model parameters then indicate estimates of the frequencies of the oscillations. To quantify the conformity between measured and modeled signals, the Pearson correlation coefficient has been calculated. An exhaustive search was applied and thus, the entire multitude of modeled signal within a predefined search interval had to be calculated. To counteract the high computing effort, they were computed in parallel on graphics processors. However, often millions of signals are required. Then, in case of graphics processing units, sets of hundreds of them have to be iteratively computed increasing the calculation time.

To reduce the computation load, different optimization procedures are discussed next. One difficulty is the presence of a significant amount of local optima in exemplary solution spaces. Such a characteristic complicates the search for different optimization methods such as the gradient descent, which benefit in case of convex spaces. Instead of maximizing the correlation coefficient, the cost function is minimized in the following to reduce the amount of required arithmetic operations. In terms of reliability, an optimization strategy is required with results of similar accuracy and precision as exhaustive search.

In this chapter, the cost function is analyzed first. Since it depends on the choice of a distance norm, different options are compared. Solution spaces of representative measurement scenarios are simulated, which are invariably characterized by numerous local rather equidistant minima. Their average distance is observed to be a function of the phases of the signal's oscillations. Based on Fourier transform equivalences, this distance is then calculated. It represents the foundation of an optimization procedure, which is introduced specifically for FMCW thickness evaluations: a set of equidistant initial points is generated each enabling to approach the closest optimum by the use of the gradient descent or Nelder-Mead algorithm. For validation, simulations and measurements are performed. The results are compared to the ones of an alternative established stochastic optimization method, a genetic algorithm. Finally, an overview of the characteristics of the different algorithms is given.

6.1 Cost Functions

For the comparison of modeled and measured signals in the previous chapters, the Pearson correlation coefficient of equation 4.1 has been used to quantify their conformity. It normalizes the signals and simultaneously compares them. However, in case amplitude variations are not expected, the conformity of two signals can also be maximized by minimizing the distance between them. At the same time, the computational load can be decreased due to the reduced number of arithmetic operations.

A real value p has to be chosen, which defines a p -norm distance and the cost function,

$$g_{\ell^p}(\boldsymbol{\tau}) = \left(\sum_{n=0}^{N-1} |\underline{s}_{ref}[n] - \underline{s}_{\boldsymbol{\tau}}[n]|^p \right)^{\frac{1}{p}} \quad (6.1)$$

with $p \geq 1$. The reference \underline{s}_{ref} corresponds to the calibrated representation of the measured signal. However, for validation of the following algorithms, also simulated signals can be used. Operator $|\cdot|$ denotes the calculation of the absolute value function.

Unless denoted differently, the reference $\underline{s}_{ref}[n]$ and modeled signal $\underline{s}_{\boldsymbol{\tau}}[n]$ are restricted to main reflections in the first place. They then correspond to the approximated analytic representation

$$\underline{s}_{\boldsymbol{\tau}}[n] = \sum_{l=0}^L a_l \exp \left(j2\pi \frac{B}{T f_s} \tau_l n + j2\pi F_1 \tau_l \right) \quad (6.2)$$

with number of layers L , time index $n \in \{0, 1, \dots, N-1\}$, requested time delay τ_l , amplitude a_l of the l^{th} reflection of L , start frequency F_1 , bandwidth B , and measurement duration T . In case that multiple reflections are significant, the signals can be calculated efficiently by the modified transfer matrix method (TMM) of section 4.3.

The optimization problem is defined by

$$\text{minimize } g_{\ell^p}(\boldsymbol{\tau}), \quad (6.3)$$

with $\boldsymbol{\tau} = (\tau_0, \tau_1, \dots, \tau_L)$.

In this section, special consideration is taken on the Euclidean ℓ^2

$$g_{\ell^2}(\boldsymbol{\tau}) = \sqrt{\sum_{n=0}^{N-1} |\underline{s}_{ref}[n] - \underline{s}_{\boldsymbol{\tau}}[n]|^2}, \quad (6.4)$$

the taxicab ℓ^1 ,

$$g_{\ell^1}(\boldsymbol{\tau}) = \sum_{n=0}^{N-1} |\underline{s}_{ref}[n] - \underline{s}_{\boldsymbol{\tau}}[n]|, \quad (6.5)$$

and for the limit $p \rightarrow \infty$, the maximum ℓ^∞ norm distance,

$$g_{\ell^\infty}(\boldsymbol{\tau}) = \max_{n=0, \dots, N-1} (|\underline{s}_{ref}[n] - \underline{s}_{\boldsymbol{\tau}}[n]|) \quad (6.6)$$

as cost functions. The operation $\max(\cdot)$ represents the calculation of the maximum value. In the following, the solution space of the correlation coefficient is compared to the ones of the different cost functions for one representative example. Depending on convergence and practicability, one option of the distance norms is then chosen for the evaluation of additional data.

For the following simulations, an acrylic glass sample-under-test (SUT) depicted in Figure 4.7 was used as well as $T = 170 \mu\text{s}$, $f_s = 10 \text{ MHz}$, $F_1 = 71.1 \text{ GHz}$, $B = 39.5 \text{ GHz}$, and $N = 1700$. A refractive index¹ of $\eta = 1.56$ [5] was assumed. Unless denoted differently, the amplitudes of the first and second reflections were 0.22 and -0.21 according to Fresnel equations neglecting absorption. Along the x-axis as well as the y-axis, the positions of the reflectors of the modeled signal are varied. For each combination (pixel), the simulated data was compared with the reference signal. The real part of correlation coefficient r_P of equation 4.1 is represented in Figure 6.1. The grayscale indicates the conformity between measured and simulated signals. The maximum for the x-value 2.34 mm and the y-value 0 mm indicated an optical path length of the sample of 2.34 mm. After dividing by the refractive index, the exact thickness of 1.5166 mm could be determined.

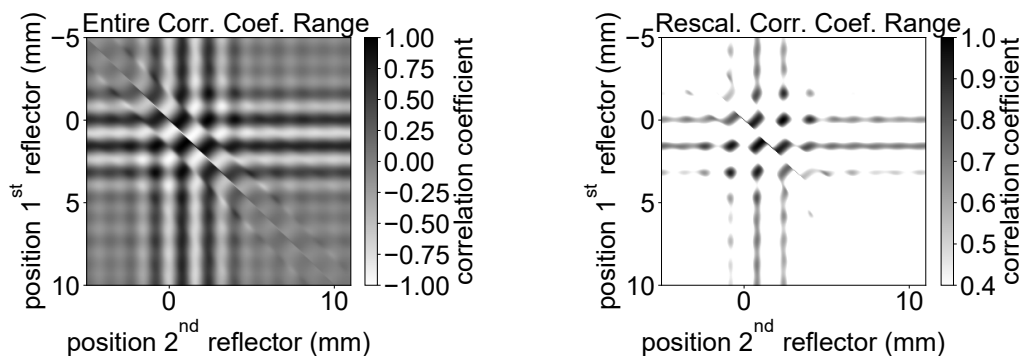


Figure 6.1: Solution space of the correlation coefficient: reference signal of SUT of optical path length $1.5166 \text{ mm} \cdot 1.56 = 2.34 \text{ mm}$, from *left to right* the depicted range of the correlation coefficient is rescaled to intensify the visibility of the significant maxima

The characteristic of numerous local optima besides the global maximum complicates the optimum search. Several optimization algorithms such as gradient approach are not efficient in case of nonconvex spaces: for small step sizes, the values may be stuck to a local optimum. If the size is chosen as too high, however, the values are likely to jump between the partial convex spaces in approximation of the different optima. The probability that the global maximum can be found is therefore reduced. Apart from that, it is notable, that the distance between adjacent optima is rather equidistant apart from interference effects.

The solution space applying the ℓ^2 norm is depicted in Figure 6.2 with a high similarity to the one in Figure 6.1. However, in this case, the minimum indicates the highest conformity. The high similarity shows that the cost function is an

¹The value varies from 1.58 evaluated in chapter 4, because a different (4.9 mm) plate for the reference measurement has been used.

appropriate substitute for the correlation coefficient. In case the refractive indices or rather amplitudes were not accurately given and normalization was necessary, the signal could be divided by their maximum values before calculating the cost function.

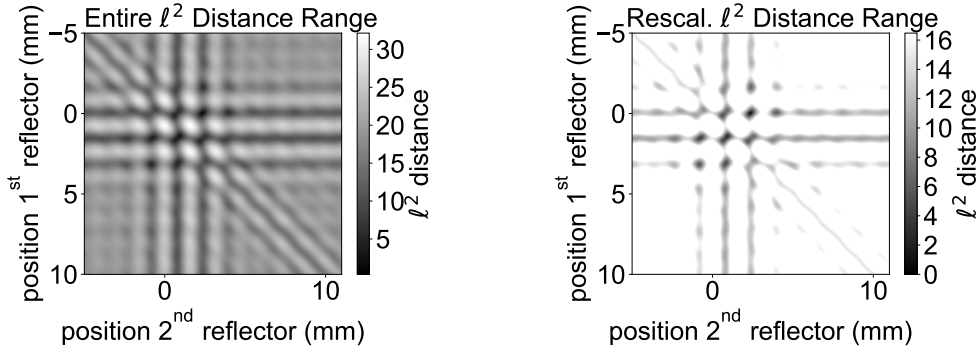


Figure 6.2: Solution space of the ℓ^2 distance, reference signal of SUT of optical path length 2.34 mm, from *left to right* the maximum depicted distance is reduced to its half, to enhance the visibility of the significant optima

Figure 6.3 presents the solution space of the ℓ^1 norm. In comparison to ℓ^2 , the contrast between maxima and minima is slightly reduced: the complete space is darker in shade in average. The representation in *right* indicates that the ℓ^1 norm resulted in additional minima with rather high values, which are slightly lower for ℓ^2 . This effect could be interpreted as a slower convergence.

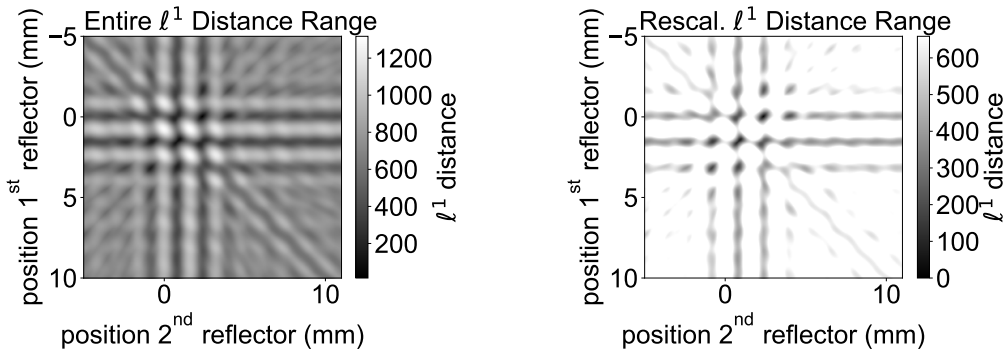


Figure 6.3: Solution space of the ℓ^1 distance, variation of maximum depicted value from *left to right* to intensify the visibility of significant minima, reference signal of SUT of optical path length 2.34 mm

Figure 6.4 is based on the maximum norm ℓ^∞ . It is characterized by a higher contrast between the minima and the rest of the solution space in comparison to other norms: the total area of light shades is increased. Therefore, in 6.4 *right* a reduced amount of optima is visible. The decrease of areas of low cost function values (dark shades) could simplify the minimum search, because it could lead to

faster convergence for methods, which are based on the calculation of the derivative. Moreover, the area of interest is reduced and the difference between global and local minima is enhanced which simplifies their distinction.

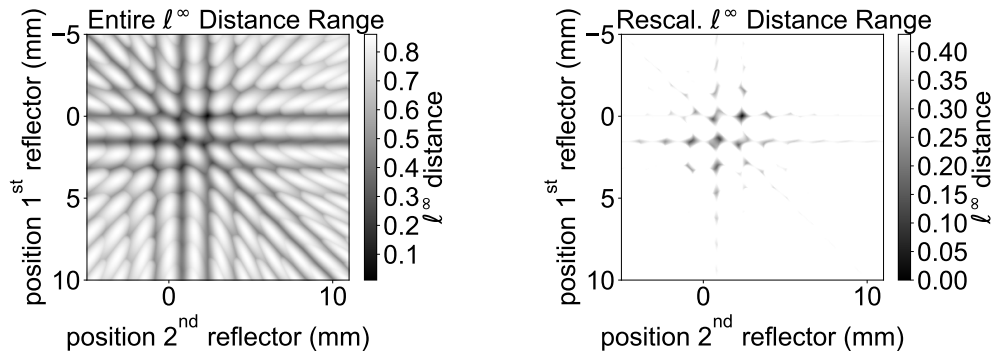


Figure 6.4: Solution space of the ℓ^∞ distance, variation of maximum depicted value from *left to right*, reference signal of SUT of optical path length 2.34 mm

Due to the higher contrast, the ℓ^∞ norm seems to be the most promising choice. However, the position of the minimum and hence corresponding distance could be affected in the presence of statistical outliers. In case of additional influences besides additive white Gaussian noise such as a nonlinear frequency ramp, the ℓ^∞ norm distance may be more prone to false results, because only the maximum deviation between the measured and modeled signals is determined. Other norms that summarize the values such as ℓ^1 and ℓ^2 are assumed to be more robust.

The slightly increased contrast of ℓ^2 values in comparison the ones the of ℓ^1 could be beneficial due to the reduced amount of significant local minima. Moreover, the square of the ℓ^2 cost function $g_{\ell^2}(\boldsymbol{\tau})$ is differentiable in case of real signals because the calculation of the absolute value can be omitted, which is not the case for ℓ^1 . This is an advantage for derivation-based optimization algorithms. For these reasons, the ℓ^2 norm is chosen for the following sections.

The choice of the ℓ^2 norm can also be motivated by the method used when detecting specific signals in the presence of additive white Gaussian noise (AWGN) with minimum error probability. The maximum-likelihood solution has to consider the conditional PDFs, which in case of AWGN result in normal distributions. Using the logarithm of PDFs, the error probability can be minimized by choosing the signal from all potential variants, that has the smallest ℓ^2 norm distance between it and the received signal. In the same way for the present thickness measurements, the probability of errors is expected to be minimized for the model-based variant when the ℓ^2 norm distance is used to indicate the conformity of measured and modeled signals.

Although different functions for comparison (cost functions and correlation coefficient) as well as parameters were used for the presented simulations, all of the solution spaces have shown a significant amount of local optima. These are largely equidistantly distributed except for interference effect. In the following section,

the influences on the average distance between adjacent minima are analyzed to determine the reasons for this characteristic.

6.2 Influences on Solution Space

The equidistant characteristic of the solution space could be influenced by the refractive indices and hence the amplitudes of the signal portions as well as the thicknesses of the SUT layers. Both are varied in comparison to Figure 6.2 next. Firstly, the thickness of the simulated acrylic plate is changed from 1.5166 mm to 3.0332 mm and 6.0664 mm in Figure 6.5. The position of the global optima of the cost function as well as significant local ones close to it are shifted but the equidistant characteristic remains.

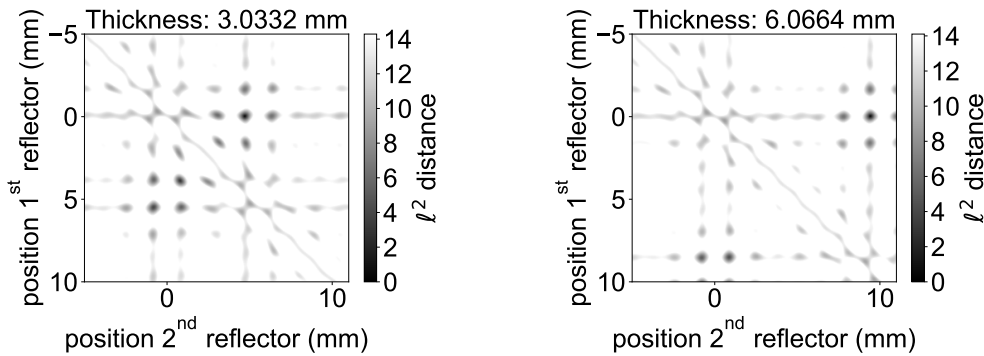


Figure 6.5: Solution space varying the optical path length of the SUT to *left*: $1.56 \cdot 3.0332 \text{ mm} = 4.68 \text{ mm}$, *right*: $1.56 \cdot 6.0664 \text{ mm} = 9.36 \text{ mm}$

In Figure 6.6, the thickness is changed back to 1.5166 mm but the amplitude of the second reflection is reduced to its half and fourth. This reduction decreases the influence of the corresponding signal portion. However, the equidistant characteristic remains for changing to position of the first reflector.

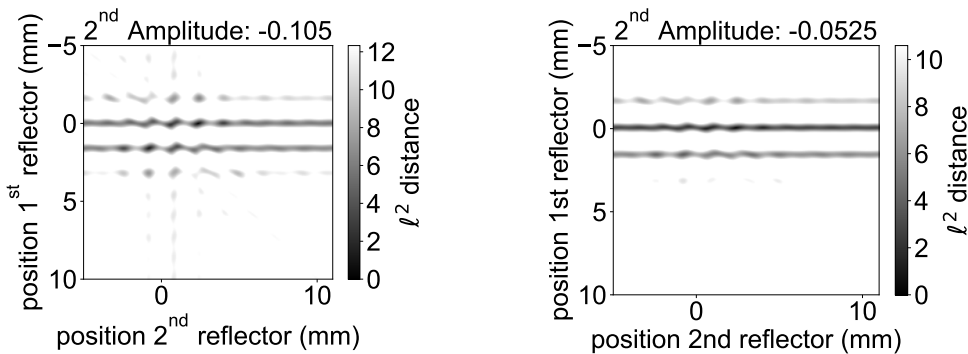


Figure 6.6: Solution space of an SUT of the optical path length $1.5166 \cdot 1.56 \text{ mm} = 2.34 \text{ mm}$ varying the amplitude of the second reflection to *left*: -0.105 , *right*: -0.0525

Hence, the amplitudes and the thicknesses determine the positions of the optima. In case of their variation, interference effects are simultaneously changing. However, the equidistant characteristic always remains and the average distance appears to be constant.

To evaluate this average distance, a single reflection is analyzed. An oscillation according to equation 6.2 can be rewritten considering the inherent measurement window:

$$\underline{s}[n] = \exp\left(j2\pi\frac{B}{Tf_s}\tau_l n + j2\pi F_1\tau_l\right) \cdot \text{rect}\left(\frac{n - \frac{N-1}{2}}{N}\right) \quad (6.7)$$

with the rectangular function $\text{rect}(n)$, which equals 1 for $n \in \{0, 1, \dots, N-1\}$ and 0, otherwise. Its discrete Fourier-transformed results in

$$\underline{S}[k] = N \exp\left(j2\pi F_1\tau_l - j\pi\frac{N-1}{N}(k - m_l)\right) \frac{\sin(\pi(k - m_l))}{\sin(\frac{\pi(k - m_l)}{N})} \quad (6.8)$$

with substitution $m_l = \frac{f_{b,l}}{f_s} = \frac{B\tau_l}{Tf_s}$. The argument of the exponential function determines the phase of $\underline{S}[k]$ and the quotient of sinusoids the amplitude of it. In case the optical path length varies, the signal's phase changes as well.

If two oscillations show the same reflector positions, their correspondence is the highest and the distance is the smallest. If the optical path length for a reflector changes, the distance changes accordingly and becomes larger. After the phase has reached the value π , the conformity increases again until it again reaches a maximum at 2π . Hence, the optical path length which corresponds to a phase shift of $\Phi_i = 2\pi$ is calculated based on the phase term of equation 6.8. The distance between an optimum and the closest neighbor then corresponds to a time delay shift of τ_l to τ'_l and an optical path length difference of $d'_l - d_l$

$$\begin{aligned} 2\pi F_1\tau'_l - 2\pi F_1\tau_l + \frac{\pi(N-1)m'_l}{N} - \frac{\pi(N-1)m_l}{N} &\stackrel{!}{=} 2\pi \\ \Leftrightarrow 2F_1(\tau'_l - \tau_l) + \frac{(N-1)}{f_s} \left(\frac{B}{T}(\tau'_l - \tau_l)\right) &= 2 \\ \Leftrightarrow \frac{(2d'_l - 2d_l)}{c_\eta} \left(2F_1 + \frac{B(N-1)}{f_s T}\right) &= 2 \\ \Rightarrow d'_l - d_l &= \frac{c_\eta}{2F_1 + \frac{B(N-1)}{f_s T}} \end{aligned} \quad (6.9)$$

with medium speed of light c_η .

The distance only depends on the setup and material parameters. Figure 6.7 indicates a rather high conformity between a signal and its 2π -shifted variant which is the reason for the equidistant characteristic. However, for a second, third etc. reflector superposition effects may occur between the peaks, which appears to be the reason for the interference effects.

This average distance can be used for the optimization process. A corresponding approach is presented in the next section.

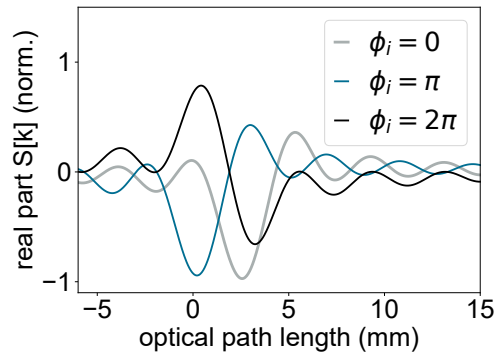


Figure 6.7: Real parts of signals shifting the phase

6.3 Optimization Algorithms

Within the spectrum of millimeter waves and terahertz applications, different optimization approaches have already been applied such as for model-based signal processing. For terahertz time-domain spectroscopy (TDS), determinations of material parameter [98] and layer thicknesses [38] have been optimized in terms of calculation load. Different schemes of optimization approaches can be identified: stochastic and gradient-based methods. One example for stochastic variants are genetic algorithms based on a set of randomly distributed initial values, which are stacked corresponding to their cost function values. In each iteration, the current points are combined to novel ones, which ideally have lower values. For gradient approaches, an initial value is moved towards the direction of its negative gradient resulting in a novel value closer to the respective minimum.

For network analysis, genetic algorithms have been applied in [46], [79] to extract material quantities based on reflection or transmission (S-parameter) measurements. For a convex solution space, gradient-based methods such as in [99] can be applied. Even a combination is presented in [100], utilizing gradient descent and genetic algorithm, sequentially. For FMCW, an alternation of Gauss-Newton and finite differences method allows characterizing single layers [101].

In this work, typical solution spaces are characterized by numerous equidistant local optima. Based on the calculation of their average distance, an equidistant set of initial values such as in Figure 6.8 is generated. Each point then enables approaching the closest local minimum, respectively [7]. Besides others, this can be achieved either by gradient descent or by Nelder-Mead algorithm, which are presented in the following. The approach based on this equidistant set is then compared to a genetic algorithm. In the first step, multiple reflections are not considered for simplicity. Afterwards, the adaptive steps are discussed which are necessary to integrate them.

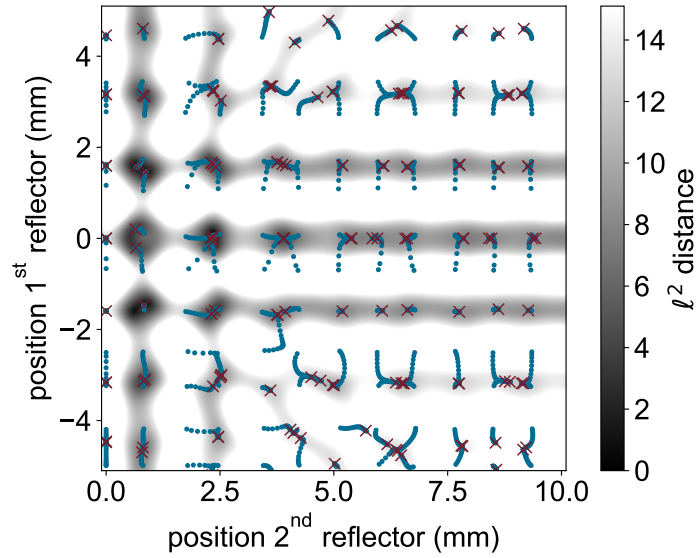


Figure 6.8: Optimization based on a set of equidistant initial points, population of each iteration (blue dots) and after 25 iterations (burgundy crosses)

6.3.1 Gradient Descent

The gradient descent approach is based on the derivative of the cost function. In a convex space, the minimum is approached by shifting an initial value toward the direction of its negative gradient. By choosing a set of equidistant initial points, each one can converge the closest minimum within the respective monotonous section of the space.

For the presented norms and for observing the complex representation of the signals in equation 6.1, the calculation of the absolute value function is required, which is not differentiable in all points. Therefore, the real representation is analyzed instead in this section. The square of g_{ℓ^2} ,

$$\begin{aligned}
 g_{GD}(\boldsymbol{\tau}) &= \sum_{n=0}^{N-1} |s_{ref}[n] - s_{\boldsymbol{\tau}}[n]|^2 \\
 &= \sum_{n=0}^{N-1} (s_{ref}[n] - s_{\boldsymbol{\tau}}[n])^2,
 \end{aligned} \tag{6.10}$$

exhibits the same minima as g_{ℓ^2} , due to the strictly increasing monotony of the square function. However, the calculation of the square root and absolute value function can be avoided for $g_{GD}(\boldsymbol{\tau})$.

For the algorithms, a local minimum can be found by shifting the current value towards the direction of the negative gradient (steepest descent). An initial value of $\boldsymbol{\tau}^0$ generates a sequence $\boldsymbol{\tau}^i$ corresponding to

$$\boldsymbol{\tau}^{i+1} = \boldsymbol{\tau}^i + \alpha^i \cdot \mathbf{d}^i, \quad i = 0, 1, \dots, I \tag{6.11}$$

with the step size α^i of the i^{th} iteration of I . The descent direction \mathbf{d}^i is calculated by

$$\mathbf{d}^i = -\mathbf{D}^i \cdot \nabla g_{GD}(\boldsymbol{\tau}^i) \quad (6.12)$$

with a positive definite matrix \mathbf{D}^i and the gradient $\nabla g_{GD}(\boldsymbol{\tau}^i)$,

$$\nabla g_{GD}(\boldsymbol{\tau}^i) = \left(\frac{\partial g_{GD}(\boldsymbol{\tau}^i)}{\partial \tau_0}, \frac{\partial g_{GD}(\boldsymbol{\tau}^i)}{\partial \tau_1}, \dots, \frac{\partial g_{GD}(\boldsymbol{\tau}^i)}{\partial \tau_L} \right)^T. \quad (6.13)$$

For \mathbf{D}^i , the unity matrix is chosen in this work to reduce the amount of arithmetic operations. Then, the procedure corresponds to the steepest descent. However, a different choice could improve convergence.

The gradient entries consist of the partial derivatives of the cost function with respect to $\tau_0, \tau_1, \dots, \tau_L$. For a τ_{l_1} with $l_1 \in \{0, 1, \dots, L\}$, it equals,

$$\begin{aligned} \frac{\partial g_{GD}(\boldsymbol{\tau}^i)}{\partial \tau_{l_1}} = & 4\pi \sum_n a_{l_1} \left(\frac{B}{Tf_s} n + F_1 \right) \sin \left(2\pi \left(\frac{B}{Tf_s} n + F_1 \right) \tau_{l_1} \right) \\ & \cdot \left(s_{ref}[n] - \sum_l a_l \cos \left(2\pi \left(\frac{B}{Tf_s} n + F_1 \right) \tau_l \right) \right). \end{aligned} \quad (6.14)$$

The choice of step size α^i influences the convergence of the algorithm significantly, as shown in Figure 6.9 *left*. On the one hand, if the chosen value is too small such as α_{small} , a large amount of iterations is required. On the other hand, for rather large values α_{large} , the calculated point can exceed the approximation of the local minimum. In case of α_{opt} , the amount of required iterations is the lowest.

The optimal value of the step size can be found by the exact line search: for each iteration, the term $g_{GD}(\boldsymbol{\tau}^i - \alpha^i \nabla g_{GD}(\boldsymbol{\tau}^i))$ is minimized. However, this method is beneficial in case of applications for which solving this equation is cost-efficient in comparison to the descent direction [102], which is not the case for the present problem.

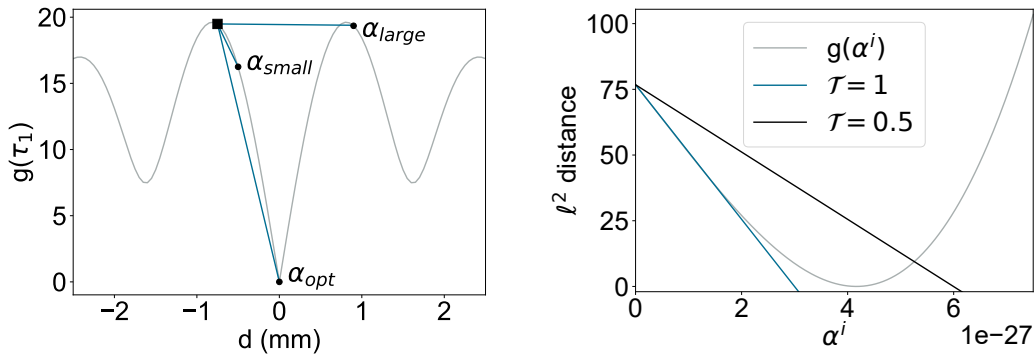


Figure 6.9: Steepest descent *left*: variation of step size α^i , square: start point, circular marker: potential points of next iteration *right*: backtracking line search, ℓ^2 norm distance cost function g as function of α^i (gray), tangents scaled by $\mathcal{T} = 1$ (black) and $\mathcal{T} = 0.5$ (blue)

A more practicable alternative is the backtracking line search, which is inexact but less complex [102]. The procedure is summarized in Algorithm 1. Instead of the optimum size, each value, that minimizes the function value fulfilling

$$g_{GD}(\boldsymbol{\tau}^i + \alpha^i \mathbf{d}^i) \leq g_{GD}(\boldsymbol{\tau}^i) + \alpha^i \mathcal{T} \nabla g_{GD}(\boldsymbol{\tau}^i)^T \cdot \mathbf{d}^i \quad (6.15)$$

with $\mathcal{T} \in [0, 0.5]$, is classified as appropriate. Figure 6.9 *right* depicts the tangents² for $\mathcal{T} = 1$ and $\mathcal{T} = 0.5$. For small \mathcal{T} , the probability of hitting a valid value is increased, while for larger ones the cost value reduction is usually more significant. In case the equation cannot be fulfilled, the step size α^i is reduced by factor $\beta \in [0, 1]$.

Algorithm 1 Backtracking Line Search

Require: descent direction $\nabla g_{GD}(\boldsymbol{\tau}^i)$, parameters $\mathcal{T} \in [0, 0.5]$ and $\beta \in [0, 1]$
 step size of the i^{th} iteration α^i
while equation 6.15 is TRUE, **do**
 $\alpha^i := \beta \cdot \alpha^i$
end while

For the present optimization problem, small starting values such as $\alpha^0 = 5 \cdot 10^{-26} \text{s}^2$ have been chosen instead of the typical value 1 to not exceed the convex area. Such small values have been determined heuristically using rough estimates of 1 GHz for descent and 10 fs for time delay. Figure 6.10 depicts an example for steepest descent with the initial point $(-1.5 \text{ mm}, -10 \text{ mm})$ comparing backtracking line search with choosing a constant step size of $5 \cdot 10^{-26} \text{s}^2$. After 20 iterations, the accuracy of approaching the optimum (determined by exhaustive search) was comparable. Therefore, and to reduce the computation load with regard to a fast implementation, a constant step size was chosen.

One remarkable advantage of the gradient descent methods is that the second order derivative, the Hessian matrix $\mathbf{H}_{g_{GD}}$, guarantees the presence of a minimum instead of saddle point or maximum in case of nonconvex spaces: the diagonal elements of it are

$$\begin{aligned} \frac{\partial^2 g_{GD}(\boldsymbol{\tau}^i)}{\partial \tau_{l_1}^2} &= 8\pi^2 a_{l_1} \sum_n \left(\frac{B}{Tf_s} + F_1 \right)^2 \cdot \left(\sin \left(2\pi \left(\frac{B}{Tf_s} n + F_1 \right) \tau_{l_1} \right) \right)^2 \\ &\quad - \left(s_{ref}[n] \sum_l a_l \cos \left(2\pi \left(\frac{B}{Tf_s} n + F_1 \right) \tau_l \right) \right. \\ &\quad \left. \cdot \cos \left(2\pi \left(\frac{B}{Tf_s} n + F_1 \right) \tau_{l_1} \right) \right) \end{aligned} \quad (6.16)$$

²The value $\mathcal{T} = 1$ is excluded.

for the entry (l_1, l_1) and nondiagonal ones equal,

$$\frac{\partial^2 g_{GD}(\boldsymbol{\tau}^i)}{\partial \tau_{l_1} \partial \tau_{l_2}} = 8\pi^2 a_{l_1} a_{l_2} \sum_n \left(\frac{B}{T f_s} n + F_1 \right)^2 \sin \left(2\pi \left(\frac{B}{T f_s} n + F_1 \right) \tau_{l_1} \right) \cdot \sin \left(2\pi \left(\frac{B}{T f_s} n + F_1 \right) \tau_{l_2} \right) \quad (6.17)$$

for entry (l_1, l_2) with $l_1, l_2 \in \{0, 1, \dots, L\}$. In case $\mathbf{H}_{g_{GD}}$ is positive definite, which is the case for positive eigenvalues or positive minorants, the present extreme value is proven to be a minimum.

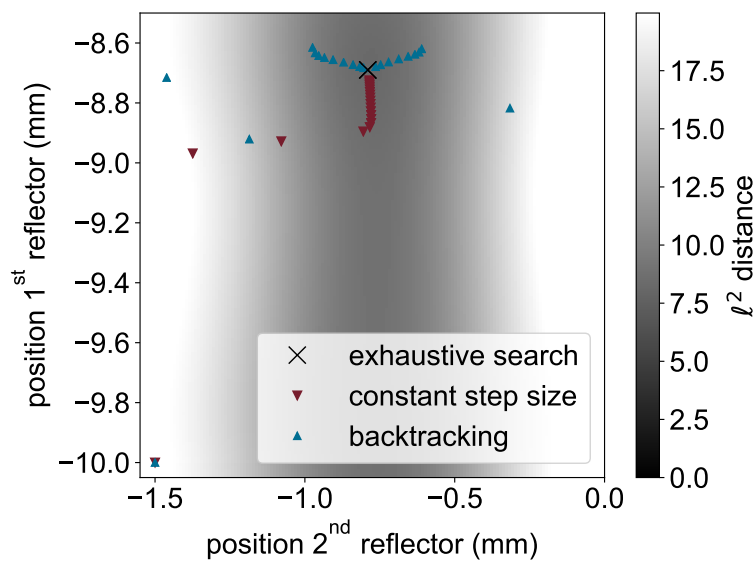


Figure 6.10: Comparison of steepest descent including backtracking line search with utilizing a constant step size, optimum of exhaustive search

One disadvantage of gradient descent in terms of FMCW thickness measurements is the adaptation for multiple reflections. In case they have to be considered, the complexity increases significantly. The equivalent transfer function of equation 4.11 has to be calculated for the general case and differentiated afterwards for gradient and Hessian matrix. Since the following Nelder-Mead algorithm solely requires cost function values, only the transfer function for the specific cases have to be determined. Through this, the calculation load might be distinctively lower in case of multiple reflections.

6.3.2 Nelder-Mead Algorithm

In convex spaces, the Nelder-Mead (downhill simplex) algorithm [103] is based on points within the solution space, which create a simplex. Iteratively, one or more of these vertices is replaced by a novel point with a lower function value to approach the minimum such as in Figure 6.11. It requires neither calculating a

derivative nor solving a second optimization problem such as exact line search of gradient descent.

Based on the set of equidistant initial points, a simplex is generated for each of them. The distance of its vertices is chosen to be smaller than half of the average minima spacing estimated in equation 6.9. The simplex is shifted to approach the closest minimum. Iteratively, the vertex with highest cost function value is replaced by a novel point (with a lower value). For its determination, the algorithm provides the options reflection, expansion, contraction, and shrinking. They are processed successively until an appropriate novel point is found: firstly, the vertex with the highest cost function τ^2 is mirrored around the centroid $\bar{\tau}$ of the remaining points as depicted in Figure 6.12 resulting in τ_r . If the cost function of the novel point is below the previous values, the distance is expanded to τ_e . For higher values, it is reduced to τ_c referred to as contraction. If the cost

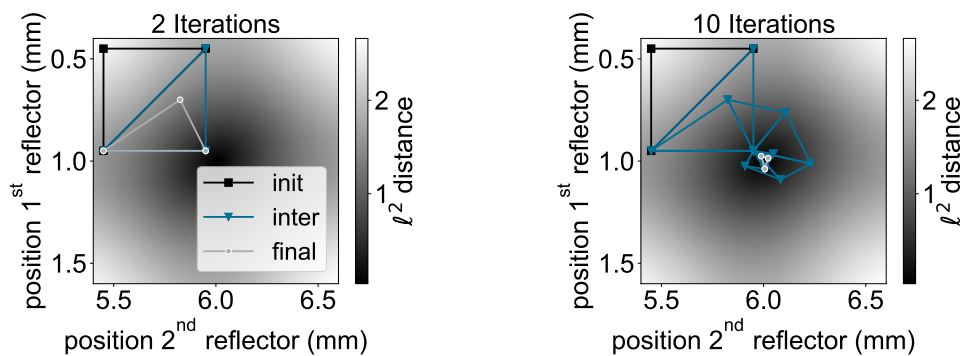


Figure 6.11: Adaption of simplex within the solution space *left*: 2 iterations, *right*: 10 iterations, initial (init) simplex (black), intermediate (inter) simplices (blue), final simplex (gray)

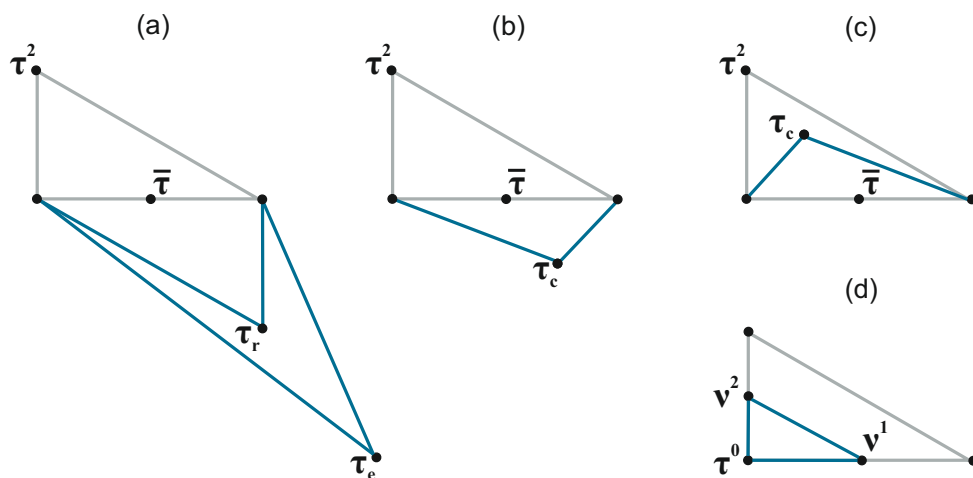


Figure 6.12: Adaptation of simplex (a) reflection and expansion (b) outside contraction (c) inside contraction (d) shrink, initial simplex (blue), novel simplex (gray)

function value of the previous vertex is higher than the centroid, a value within the old simplex is calculated and otherwise outside of it. In case all calculated points exhibit higher function values, the simplex is shrunk. While keeping the point with the lowest value, the other points are moving towards it by replacing τ^1 and τ^2 with ν^1 and ν^2 .

The procedure and the required equations are summarized in Algorithm 2. Typical choices for the parameters are $\rho = 1$ for reflection, $\chi = 2$ for expansion, $\gamma = \frac{1}{2}$ for contraction, and $\sigma = \frac{1}{2}$ for shrinking [104]. The algorithm terminates either when a maximum number of iterations is reached or when the deviation of the values as well as function values are getting smaller than chosen thresholds.

Algorithm 2 Nelder-Mead Algorithm

Require: $L + 2$ initial points $\tau^0, \tau^1, \dots, \tau^{L+1}$ for L layers

scaling parameters: $\rho = 1, \chi = 2, \gamma = \frac{1}{2}, \sigma = \frac{1}{2}$

1: **Order** $\tau^0, \tau^1, \dots, \tau^{L+1}$ according to the function values

$$g(\tau^0) \leq g(\tau^1) \leq \dots \leq g(\tau^{L+1}).$$

Calculate the centroid $\bar{\tau}$ of the L best values τ^0, \dots, τ^L .

2: **Reflect** the worst point τ^{L+1} :

$$\tau_r = (1 + \rho)\bar{\tau} - \rho\tau^{L+1}$$

Function value $g(\tau_r)$ between function values of best and worst value?

Replace worst value with τ_r and go to step 1.

3: Function value $g(\tau_r)$ smaller than best function value?

Expand

$$\tau_e = (1 + \rho\chi)\bar{\tau} - \rho\chi\tau^{L+1}.$$

Replace worst value with τ_r or τ_e depending on the smaller function value and go back to step 1.

4: Chose $\bar{\tau}$ or τ^{L+1} depending on the smaller function value.

$\bar{\tau}$?

Outside contraction: $\tau_c = (1 + \rho\gamma)\bar{\tau} - \rho\gamma\tau^{L+1}$
 τ^{L+1} ?

Inside contraction: $\tau_c = (1 - \gamma)\bar{\tau} + \gamma\tau^{L+1}$

Function value smaller than worst function value?

Replace worst value with τ_c and go back to step 1.

5: **Shrink:** Replace $\tau^1, \dots, \tau^{L+1}$ with ν^1, \dots, ν^{L+1} with

$$\nu^l = \tau^0 + \sigma_s (\tau^l - \tau^0)$$

and go back to step 1.

One disadvantage of Nelder-Mead algorithm is the absence of a minimum guarantee as the Hessian matrix of gradient approach. However, using the standard parameter, the algorithm does not require the calculation of a step size, even

though the width of the initial simplex and the choice of the parameters have a certain regulation characteristic. Since not any time derivation is required, the TMM can be directly adapted to observe multiple reflections.

For the novel optimization approach based on the equidistant set of initial points, both gradient descent and Nelder-Mead algorithm are used in the following. In order to compare the results with a classical optimization method, a genetic algorithm is presented next.

6.3.3 Genetic Algorithm

Genetic algorithms [105] are stochastic optimization methods. As depicted in Figure 6.13 *left*, they are based on randomly distributed initial values in the solution space, which are combined to create a novel population in each iteration. Ideally, some of the novel points are lower in their cost function values. The complete procedure is summarized in Figure 6.13 *right*. For all presented optimization algorithms, a stop criterion has to be chosen, e.g., value variations are below a certain threshold. For each iteration, the steps selection, crossover, and mutation are performed. The steps are illustrated in the following using a small

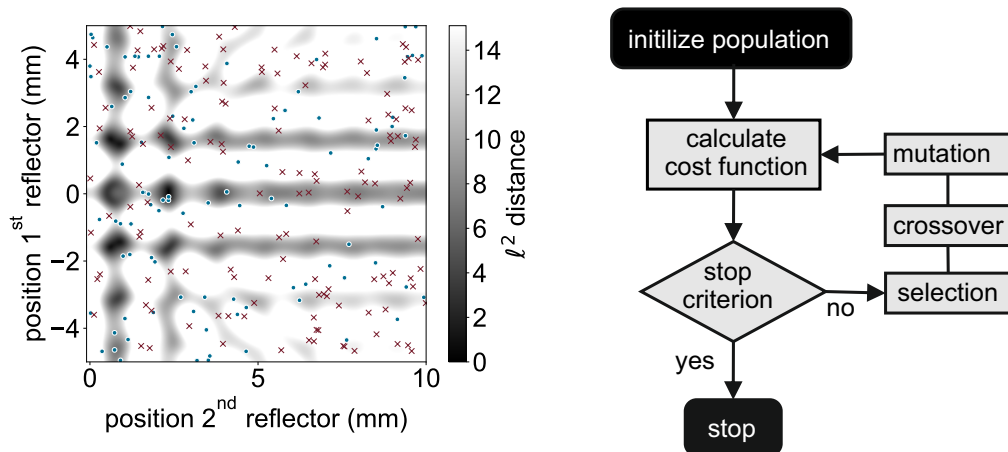


Figure 6.13: Genetic algorithm *left*: solution space with population of the first iteration (burgundy crosses) and of the 20th iteration (blue dots), *right*: float diagram of the genetic algorithm

population as an example. Six randomly distributed points in the search space are chosen. The corresponding cost function values are calculated. Afterwards, the points are encoded as binary strings (chromosomes) such as in Table 6.1.

Selection

Based on the initial population in Table 6.1, a set of chromosomes for the next iteration is generated. Depending on the cost function value, different options are operated.

- The chromosome with the lowest value is selected and transferred to the population of the next iteration: chromosome 5.
- The chromosome with the highest cost function value is discarded: chromosome 4.
- Chromosomes are randomly chosen for the following crossover depending on the choice of a crossover probability. Exemplarily, for a probability of 0.5, two of the four remaining chromosomes are required. In this case, the chromosomes 2 and 6 are chosen.
- The remaining chromosomes 1 and 3 are transferred to the novel set.

Table 6.1: Example of Initial Population of a Genetic Algorithm

index	chromosome	cost function value	decision
1	10000010001 10001110111	64.57	new population
2	11010100111 01110010001	231.95	crossover
3	01001010110 10101001001	295.18	new population
4	00100100110 00101011001	408.78	discard
5	10000001111 00111001010	5.92	new population
6	10100001010 11010011000	172.54	crossover

The blue and gray coloring highlights the sections which are recombined for the following crossover.

Crossover and Mutation

For the next population, two novel chromosomes, the children, are created by combining portions of the binary codes of respectively two parents such as the blue and gray sections of the chromosomes 2 and 6 of Table 6.1. Table 6.2 represents the resulting children. This procedure is referred to as crossover. According to a mutation probability, few bits of all chromosome structures are varied. The children are then transferred to the novel population.

Table 6.2: Exemplary Set of Children before and after Mutation

	child 1	child 2
before mutation	11010100111 11010011000	10100001010 01110010001
after mutation	01010100111 11010011001	10100001010 11110010011

The new population combines mutated chromosome of previous population (such as 1, 3, and 5), the mutated children, and an additional random chromosome such as the one in Table 6.3. The set is used as the initial population of the next iteration.

Table 6.3: Random Chromosome

chromosome	00100111000 01111110001
------------	-------------------------

Since genetic algorithms are stochastic methods, it cannot be guaranteed whether the global minimum can be found. The probability of a hit however depends on the various parameters: the probability is higher if a sufficiently large start population is chosen. Moreover, the crossover and the mutation probability have to be chosen in a way that they correspond to the solution space. If the number of crossovers increases, the global optimum can be found within a smaller number of iterations in some cases. For other problems, values close to the global minimum can be discarded and the population then may be stuck to a fraction of the space. The mutation induces a certain degree of randomness, which can be advantageous in widely varying spaces.

For the following simulations and measurements, the size of the population equaled the set size of the other algorithms to simplify their comparison. Probabilities of 0.8 for crossover and 0.1 in terms of mutation were selected to prevent limiting the candidates to a section of the solution space and allow novel candidates.

6.4 Comparison of Algorithms

The functionality of all presented algorithms are compared in the following. Firstly, they are tested for validation. Afterwards, a static of simulations is performed to compare the computation time of the different methods as well as the accuracy and precision of their results. Then, measurement results are shown for thin single layers. To present the potential for multilayers, a two-layered SUT is simulated and evaluated by the different algorithms. Finally, a discussion of the characteristics of all approaches is given.

6.4.1 Validation of Algorithms

The presented algorithms were tested for validations based on simulations. The acrylic glass SUT (Figure 4.7) with a thickness of 1.5166 mm and optical path length of 2.34 mm was simulated. The variance of additive white Gaussian noise was modeled as $1/3309.57$ according to the SNR_S of Table 5.2. To apply the presented algorithms, a stop criterion had to be chosen. For the comparing exhaustive search, a step size of $10 \mu\text{m}/1.56$ was used. Therefore, the optimization algorithms were stopped either if the variations were smaller than this value or after a maximum number of 50 iterations. For the Nelder-Mead algorithm, the MATLAB implementation [106] was utilized. For steepest descent, a constant step size of $\alpha^i = 3 \cdot 10^{-27} \text{s}^2$ was heuristically determined considering estimates for each gradient entry of THz, while the τ_l were estimated as 1 fs. Additionally, the step size had to be chosen even smaller to restrict novel points to the convex

areas, respectively.

Figure 6.14 depicts the final populations. The values of the genetic algorithm tended to accumulate to the left side. Such an accumulation could prevent hitting the global optimum. If the population is restricted to a section of the solution space, then the probability of approaching the global minimum by the crossover procedure is very low. The steepest descent and the Nelder-Mead algorithm have identified almost all local minima evaluated by exhaustive search. For this example, all algorithms approached the global minimum.

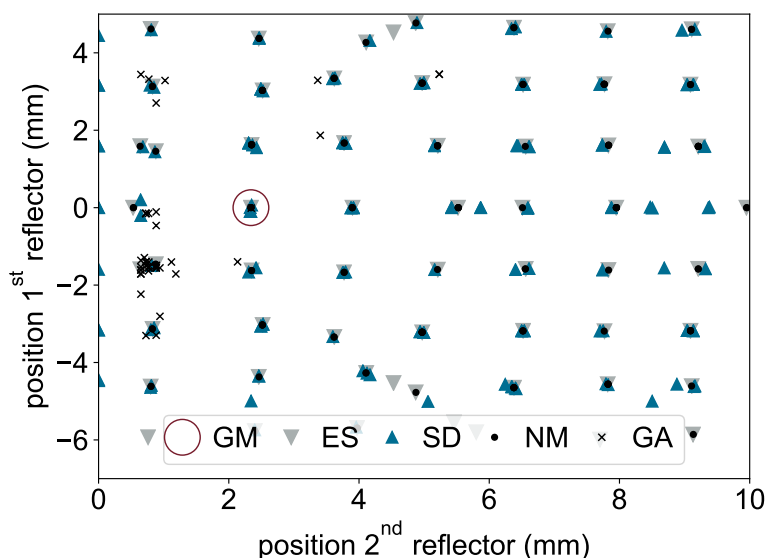


Figure 6.14: Comparison of final values of different optimization algorithms exhaustive search (ES), steepest descent (SD), Nelder-Mead algorithm (NM), and genetic algorithm (GA), global minimum (GM)

6.4.2 Computation Time, Precision, and Accuracy

In order to create a statistic, the simulation for the previous section was repeated 100 times utilizing different noise sample functions. Figure 6.15 presents the evaluated values of each algorithm and repetition as well as the expected global optimum for this SUT. Several times, the genetic algorithm approached a local minimum instead of the global one, while steepest descent and Nelder-Mead approached the exact value each time.

The results are summarized in Table 6.4 with the highest accuracy of Nelder-Mead algorithm. The corresponding variance approaching zero is assumed to not represent the actual precision but to be influenced by the choice of the stop criterion. Steepest descent required the lowest average calculation time of 418 ms in MATLAB³ which may be influenced by the lowest amount of iterations. The

³Intel Core i7-8565U central processing unit, 1.80 GHz, 4 physical cores, MATLAB R2019a

accuracy of genetic algorithm is insufficient for reliable results, since the bias almost equaled 10 % of the reference value. The variations of its results depicted in Figure 6.15 transfer to a high standard deviation of 492 μm , which is unreliable as well.

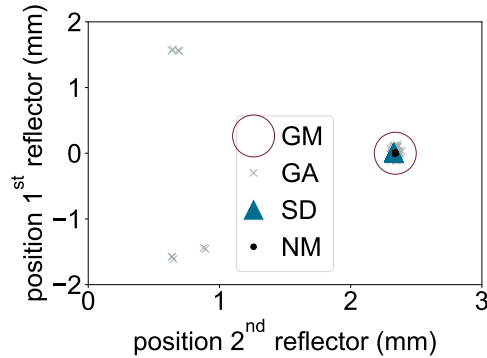


Figure 6.15: Evaluated global optima of 100 independent simulations using genetic algorithm (GA), steepest descent (SD), and Nelder-Mead algorithm (NM), global minimum (GM) of the SUT

Table 6.4: Results of Optimization Algorithms Steepest Descent, Nelder-Mead, and Genetic Algorithm Evaluating Simulated Data

	steepest descent	Nelder- Mead	genetic algorithm
mean value	1.49 mm	1.50 mm	1.36 mm
standard deviation	77 nm	556 fm	492 μm
calculation time MATLAB	418 ms	1.45 s	1.01 s
average number of iterations	19.9	29.3	50

With regard to time-efficient implementations of the algorithms, an alternative approach is substituting the previous criterion of small variations of the cost function value by a constant amount of repetitions to prevent queries. An appropriate value can be evaluated heuristically, since solution spaces do not vary significantly as shown in Figures 6.1 – 6.6. An amount of 100 simulations was performed and discontinued after 25 iterations.

Table 6.5 represents the results with reduced computation time for all variants. For Nelder-Mead and genetic algorithm, the value is less than half of the previous one. Even though the number of iteration was increased for gradient descent, the calculation time was decreased presumably just due to the prevention of the queries. The results of steepest descent and Nelder-Mead are again accurate and their variances were low: below 1 μm . Hence, their results are classified as reliable. The bias of the genetic algorithm is larger than 20 %.

Table 6.5: Values of Optimization Algorithms Steepest Descent, Nelder-Mead, and Genetic Algorithm after 25 Iterations Evaluating Simulated Data

	steepest descent	Nelder- Mead	genetic algorithm
mean value	1.50 mm	1.51 mm	1.17 mm
standard deviation	0.16 μm	0.25 μm	745.75 μm
calculation time MATLAB	305 ms	712 ms	408 ms

6.4.3 Measurement Results

Then, the algorithms have also been tested using measured signals. For this purpose, well-defined calibration samples consisting of acrylic with different thicknesses were utilized. Figure 6.16 shows the samples-under-test, which have also been measured for [5], [7], [11]. The thickest plate of 4.9 mm was used as a reference to calculate the refractive index of 1.56. The optimization algorithms have been discontinued after 25 iterations again to take into account that this variant would be advantageous for later implementations by preventing queries. For steepest descent, a constant step size of $3 \cdot 10^{-27} \text{s}^2$ was again heuristically evaluated. The distance between the initial values however was assessed conservatively as a quarter of the expected distance between optima. A search interval of 3.2 mm to 6.4 mm was used for exhaustive search.

**Figure 6.16:** Photograph of acrylic samples-under-test

Table 6.6 summarizes the results of five individual measurements for each SUT. For comparison, TDS-evaluated values are provided as well. Since it determined slightly larger values particularly for the 1.5166 mm plate, it indicates, that the refractive indices of the different samples could be marginally different.

The genetic algorithm resulted in a bias of more than 20% for the 1.5166 mm

SUT. Additionally, its values are imprecise with high standard deviations of up to $864\ \mu\text{m}$, while to ones of exhaustive search, steepest descent and Nelder-Mead algorithm were below $2\ \mu\text{m}$. Steepest descent yielded a bias of roughly 7% but only for the thinnest SUT of $773\ \mu\text{m}$. Results of Nelder-Mead algorithm highly conform to the ones of exhaustive search and are therefore the most promising.

Table 6.6: Results of Steepest Descent, Nelder-Mead, Genetic Algorithm, Exhaustive Search, and TDS Evaluating Measurements of Acrylic Sheets

thickness	TDS	search interval	exhaustive search	steepest descent	Nelder-Mead	genetic algorithm
4.9 mm $\pm 1\%$	4.9 mm	3.2 mm – 6.4 mm	4.9 mm $\pm 0.6\ \mu\text{m}$	4.9 mm $\pm 0.3\ \mu\text{m}$	4.9 mm $\pm 1.2\ \mu\text{m}$	5.1 mm $\pm 501.4\ \mu\text{m}$
1.5166 mm $\pm 0.4\%$	1.53 mm	0 mm – 3.2 mm	1.55 mm $\pm 0.6\ \mu\text{m}$	1.61 mm $\pm 1.4\ \mu\text{m}$	1.55 mm $\pm 0.0\ \mu\text{m}$	1.18 mm $\pm 863.9\ \mu\text{m}$
959 μm $\pm 1\%$	964 μm	0 mm – 3.2 mm	976 μm $\pm 0.0\ \mu\text{m}$	978.7 μm $\pm 0.1\ \mu\text{m}$	975.5 μm $\pm 0.6\ \mu\text{m}$	978.7 μm $\pm 13.2\ \mu\text{m}$
773 μm $\pm 1\%$	776 μm	0 mm – 3.2 mm	775 μm $\pm 0.8\ \mu\text{m}$	825.3 μm $\pm 0.4\ \mu\text{m}$	779.5 μm $\pm 0.5\ \mu\text{m}$	749.1 μm $\pm 42.5\ \mu\text{m}$

6.4.4 Multilayers

Exemplarily, for multilayers, a two-layered SUT was simulated. Thicknesses and refractive indices were 1.5 mm and 2.034 mm as well as 1.56 and 1.8, respectively. The search intervals of each boundary surface had optical path length widths of 10 mm and the step size equaled $10\ \mu\text{m}$. The exhaustive search required a calculation time of roughly 66 h in MATLAB.

The results of 10 repetitions are shown in Table 6.7 for the optimization algorithms. For steepest descent, a constant step size of $5 \cdot 10^{-27}\ \text{s}^2$ was used. The algorithms have been discontinued for value changes of less than an optical path length of $10\ \mu\text{m}$ or after finishing 250 iterations. In comparison to exhaustive search, the calculation time was significantly reduced for all cases. The evaluated thicknesses of Nelder-Mead and genetic algorithm were accurate, while the values of steepest descent were biased. The offset for instance equaled 37% for the second layer. Due to the combination of accurate and precise results, the Nelder-Mead algorithm is again determined as the most promising approach.

For each additional layers, the difference between exhaustive search and its alternatives is expected to be even more significant. However, for inline measurements, the implementation has to be further optimized such as by parallel computing on graphic processors. Alternatively, the width of the search intervals could be reduced.

Table 6.7: Results of Optimization Algorithms Steepest Descent, Nelder-Mead, and Genetic Algorithm Evaluating Two-Layered SUT

	steepest descent	Nelder- Mead	genetic algorithm
layer 1 (1.56 mm)	1.75 mm ± 5 nm	1.50 mm ± 1.56 μ m	1.50 mm ± 20.13 μ m
layer 2 (2.034 mm)	3.20 mm ± 6 nm	2.03 mm ± 154 nm	2.04 mm ± 9.49 μ m
calculation time	10 s	37 s	93 s

6.4.5 Discussion of Algorithms

The optimization approach based on an equidistant set of initial points and applying gradient descent or Nelder-Mead algorithm was presented and compared to exhaustive search and a genetic algorithm. Each approach exhibited individual advantages and disadvantages. The exhaustive search required a high computation time utilizing MATLAB, but evaluated all local minima for a sufficiently small step size. Especially for additional layers and more complex solution spaces with a higher degree of interference of peaks in the frequency domain, the detection of a significant amount of local optima appears to be an important criterion for comparison. Steepest descent and Nelder-Mead algorithm detected almost all of the local optima for the presented example of the acrylic layer. For genetic algorithm, values tended to accumulate in a section of the solution space which could result in inaccurate values. The accuracy and precision of Nelder-Mead algorithm highly conformed to the ones of the exhaustive search for all presented examples.

All optimization algorithms enabled to compute the results much faster than for exhaustive search such as less than 2 min instead of 66 h for the two-layered samples. However, in terms of real-time applications, even faster implementations might be required. One method to further reduce the calculation time is parallel processing. Usually the exhaustive search is ideal for parallelization since it conforms to a single instruction multiple data operation. However, since often several million of modeled signal have to be calculated, typical numbers of parallel processors or graphic processing units are exceeded which increases the calculation time due to sequential processing. Steepest descent and Nelder-Mead algorithm based on equidistant initial values are suitable for parallelization as well, since each candidate can be individually processed. However, the genetic algorithm recombines values after each iteration, which would avoid any computational advantage of parallel computing.

Multiple reflections for a varying number of layers have not been completely described by an iterative formula, but by the modified TMM. For exhaustive search, Nelder-Mead, and genetic algorithms, this method can be directly applied to calculate the respective signal of the current parameters. Since steepest descent is

based on the calculation of the first and optional second order derivative, it requires to determine the matrix and transfer function for the general case, which results in a significant increase of complexity. Nevertheless, gradient methods can guarantee for the presence of a minimum instead of other stationary points for positive definite Hessian matrices. Such a criterion is not inherently given for the other variants. However, the solution spaces of the different examples have been rather similar and such a guarantee has not been required, yet.

Table 6.8 summarizes all discussed aspects. It should be noted that the determined properties were influenced by the choice of parameters. For instance in case of the genetic algorithm, different configurations such as with an increased number of individuals could lead to results that are more accurate. However, genetic algorithms still tend to be rather slow optimization variants [105] in general.

Table 6.8: Summarizing Comparison of Exhaustive Search, Steepest Descent, Nelder-Mead, and Genetic Algorithm

	exhaustive search	steepest descent	Nelder- Mead	genetic algorithm
hit local optima	++	+	+	-
accuracy	++	+	++	-
precision	++	++	++	-
potential for parallel computing	+	++	++	-
modified transfer matrix method	++	-	++	++
minimum guarantee	-	++	-	-
calculation time MATLAB	-	++	+	+

For a complete analysis, the convergence properties of the algorithms also has to be discussed. Since the genetic algorithm is a stochastic method, it cannot be guaranteed that the global minimum can be found. The steepest descent method is proven to approach the corresponding optimum [107] at least for special requirements such as using direct line search and analyzing convex spaces⁴. The Nelder-Mead algorithm was observed to converge towards a nonstationary point even in convex areas [108]. However, for all examples presented in this work, it always approached the global minima. Since the solution spaces do not significantly vary, convergence can be expected for further measurements.

With increasing number of reflections, and for considering the multiple reflections, solution spaces are assumed to get more divers, particularly, the interference effects. It cannot be guaranteed, that in approximation of the convex section of the global minimum, an initial point is located to approach it. For these cases however, the distance of the initial points could be reduced. For thickness measurements, resolution, accuracy, and precision appear to be the most important

⁴Both requirements have not been fulfilled for the presented examples.

criteria. It is therefore recommended to focus on the Nelder-Mead algorithms in future works.

Based on the findings of the previous chapters, the potential of the model-based approach for being used in future applications is discussed in the following one. Measurements of industrial samples are presented and the minimum measurable layer thickness is heuristically determined.

7. Applications

In the previous chapters, a model-based approach was presented for an accurate determination of layer thicknesses below the Rayleigh limit for frequency-modulated continuous-wave (FMCW) systems. The method was validated based on well-defined plane-parallel samples-under-test. Based on the previous findings, this chapter presents additional thickness results illustrating the potential of the approach for evaluating measurements of industrial samples and hence being used in future applications.

For this purpose, a rotation-based setup is presented for the inspection of tube walls in this chapter. Promising circumference measurement results of a multi-layered section are shown and validated by terahertz time-domain spectroscopy (TDS). The influence of discontinuities is analyzed based on an additional measurement series of a tube section with a stepped profile. The minimum measurable thickness is determined exemplarily for polyethylene terephthalate sheets. Since compact transceivers such as monolithic microwave integrated circuits and commercial systems-on-chip usually provide lower bandwidths, their potential for future setups in combination with the model-based approach is demonstrated by virtually reducing the bandwidth of measured signals.

7.1 Measurement Setup

The rotation measurement setup of Figure 7.1 *left* enables the analysis of cylindrical samples-under-test such as tube walls. The object can be positioned on rollers and rotated to measure along the circumference. The rectangular cut out in the metal rack enables the illumination by the beam. A combination of a 2 inch (5.08 cm) collimator lens and a parabolic mirror in Figure 7.1 *right* are guiding the beam in a way that its focus approaches the center of the sample-under-test (SUT). The high frequency components of the measurement head such as antenna, directional coupler, and frequency multiplier are produced by RPG Radiometer Physics GmbH. For data acquisition, the board NI PCI 6115 [109] of National Instruments is utilized. Table 7.1 summarizes the parameters of the setup.

The measurement head can be activated by a graphical user interface based on LabVIEW. This interface can be used either to save the data or to directly process them. Different modes are available for signal processing. The peak detection

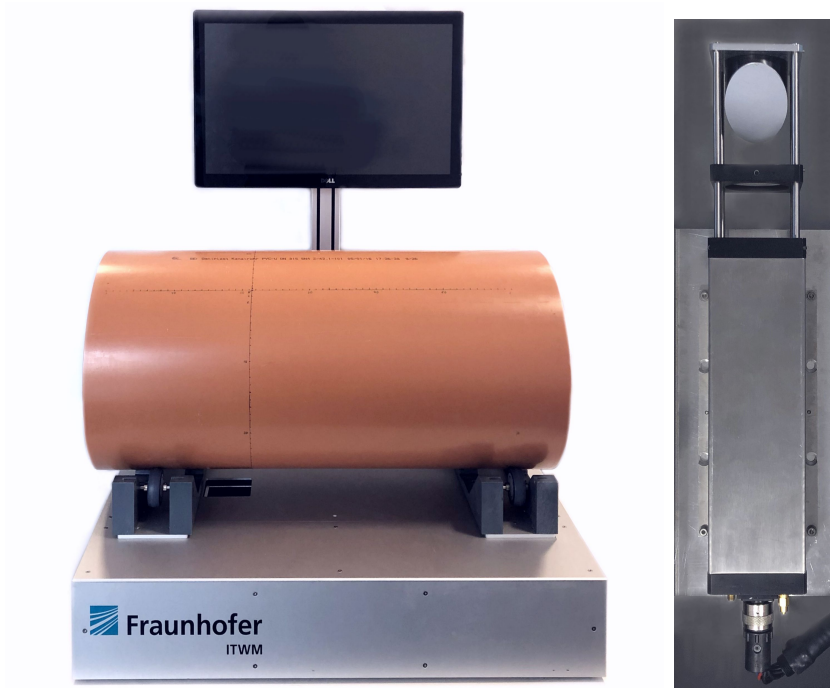


Figure 7.1: *left:* reflection mode setup for rotation measurements, *right:* focusing unit of collimating lens and parabolic mirror

Table 7.1: Parameters of the Rotation Measurement Setup

quantity	symbol	value
duration of frequency modulation	T	$170 \mu\text{s}$
sampling frequency	f_s	10 MHz
number of samples	N	1700
start frequency of frequency modulation	F_1	71.1 GHz
bandwidth of frequency modulation	B	39.5 GHz
Rayleigh depth resolution limit	Δr_R	3.9 mm

variant including a Hamming window for rather thick layers enables a fast evaluation. Instead of a zero-padded [67] discrete Fourier transform, which calculates many data samples for equidistant frequency points in the complete range, the Chirp-Z transform [62] is utilized. It enables to solely determine a predefined section such as the region-of-interest. The second option, the model-based processing, activates the dynamic-link library to operate the general-purpose graphics processing unit (GP-GPU) to compute modeled signal in parallel. The setup configuration includes an NVIDIA GeForce GTX 980¹. For each potential combination of boundary surface positions required for exhaustive search, a new thread is activated on it. In case all of them are processing, the different sets of models

¹4096 MBytes global memory, 2048 CUDA Cores, 1.3 GHz maximum clock rate, CUDA 10.2

are scheduled, sequentially.

7.2 Measurement Results

Polyvinyl chloride tubes are used for water transport for instance. In order to guarantee safety, their production is regulated by different norms [110], [111]. The millimeter and terahertz waves technology represents a novel method to test them without requiring any contact. Corresponding setups show the potential to be integrated into the extrusion process to instantly inspect the product requirements such as achieving a minimum thickness. Simultaneously, by controlling the input parameters of the production, material resources could be saved. Based on the setup presented in the previous section, the wall thickness of a tube is measured in the following as a first example.

7.2.1 Tube Wall Inspection

Some light-weight polyvinyl chloride tube variants are filled with a foam instead of a solid core. Electromagnetic radiation of the W band has a rather high penetration depth in these materials, which is the reason for the selection of this frequency band. Exemplarily, the tube of Figure 7.2 is analyzed in this section. It consists of three individual layers. Outer and inner polyvinyl chloride layers in orange are solid and thinner than 1 mm, while the recycle foam core between them has a rough thickness of 6 mm. The measurement was performed along its circumference.

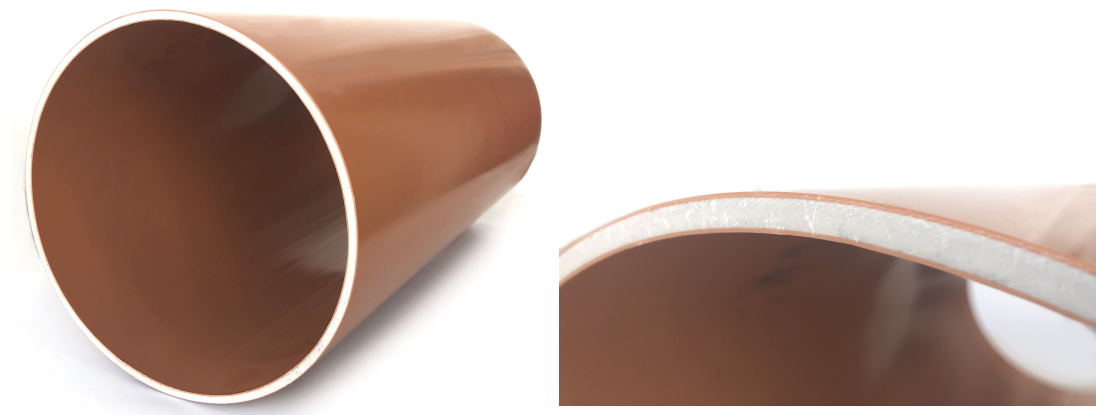


Figure 7.2: Photographs of a multilayered tube SUT

The evaluated optical path lengths are presented in Figure 7.3. In terms of search intervals, the memory of the GPU restricted the number of modeled signals, which can be processed in one iteration. The amplitudes of the first to fourth reflection have been fitted as 0.25, -0.06, 0.04, and -0.19. Utilizing a step size of 50 μm , in case of 3 layers or rather 4 boundary surfaces, interval widths of optical path lengths of 1.5 mm guaranteed a stable processing for the exhaustive search within

less than 2 s.

Due to the excentricity of the tube, the first boundary surface was moving up and down by the rotation on the rollers, which exceeded constant search intervals. To compensate for that, the peak detection was used to adapt the intervals according to the first resulting peak. Even though this maximum does not accurately identify the position of the first boundary surface, it correspondingly varies. The resulting intervals are depicted in Figure 7.3 indicated by the gray surroundings of the resulting positions (rfl.). They were chosen as disjoint.

Instead of thicknesses, solely optical path lengths are presented. The determination of the refractive indices exhibited difficulties, because single-layered test samples of the different materials have not been available². Moreover, the measured positions are also not accessible for a caliper gauge. The resulting values for the refractive indices were therefore not sufficiently accurate. However, thickness variations, which can be even more important than absolute values for several applications, are also indicated by optical path length variations.

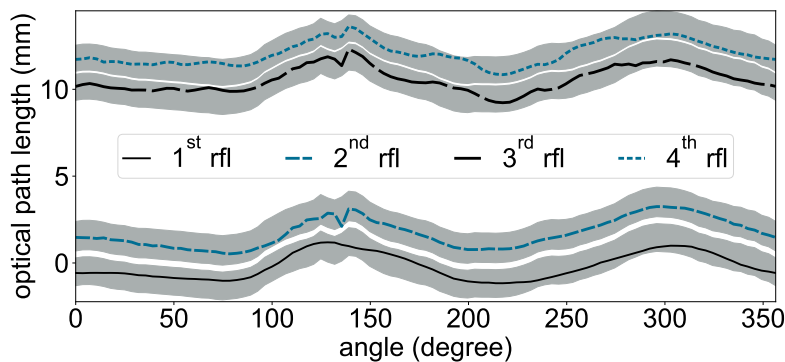


Figure 7.3: Adapted search intervals (gray) of circumference measurement, rfl: reflector

For Figure 7.4, the optical path lengths are represented as distances between the corresponding reflector and the first boundary surface. This conversion allows the comparison with values evaluated by TDS. For the TDS measurement system, the distance between sensor and first boundary surface had to be constant due to the length of the delay line. The high conformity of the evaluated positions by both methods validates the FMCW results. The slight differences of the values may be caused by positioning inaccuracies when rotating the tube. For an angle of 138° , the conformity between modeled and measured signal is low for both, TDS and FMCW. This deviation is assumed to be caused by a feature of the SUT such as a weld.

Using a millimeter gauge, the optical path length between the center of the wall

²An attempt to cut the SUT into different single-material section resulted in stripes which were thinner than the beam width. In case of the solid material, these were highly convex due to the tension of the surface affecting the accuracy of any kind of reference measurement. For the foam core, the material sections were expanding and therefore not representative for the compressed material.

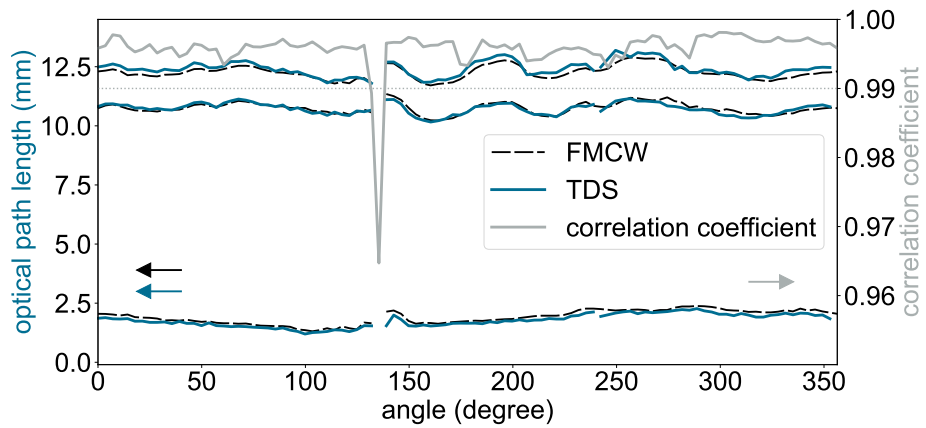


Figure 7.4: Circumference measurement of tube section: optical path length evaluated by FMCW and TDS (left y-axis), correlation coefficient in case of FMCW (right y-axis), threshold (dotted) of 0.99

and the inner boundary surface has been evaluated as well, which is the basis for the polar representation in Figure 7.5. The lower layer in the Figures 7.3 and 7.4 then corresponded to the outer one. All representations show that the optical path lengths and hence thicknesses fluctuate. Detecting such variations appears to be beneficial to control the safety of the tube.

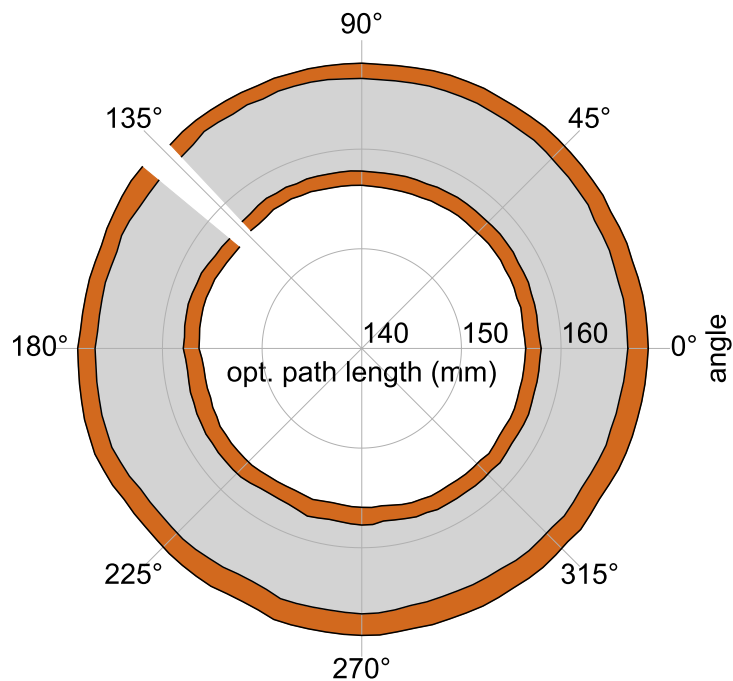


Figure 7.5: Polar representation of circumference measurement results

For the presented SUT, the boundary surfaces have been continuous. However, for different application, discontinuities may occur. Since the measurement spot

is roughly few millimeters in size, such features can have an influence on the evaluation of points in their approximation.

7.2.2 Stepped Tube Wall Section

To analyze the effect of discontinuities, stepped wedges were cut into a tube section depicted in Figure 7.6 *left*. This SUT is thicker than the one of Figure 7.2. The height of such a step equaled $300\ \mu\text{m}$. Figure 7.6 *right* represents the evaluated optical path lengths. Each point corresponds to a mean value of five single measurements. Search intervals of 1.6 mm to 3.7 mm, 11.5 mm to 14.9 mm, and 0.5 mm to 4.5 mm for the lower, center, and upper layers have been chosen, respectively. The edges of the steps are indicated by black squares. The amplitudes of the first to the fourth reflections have been fitted as 0.26, -0.045, 0.095, and -0.16.

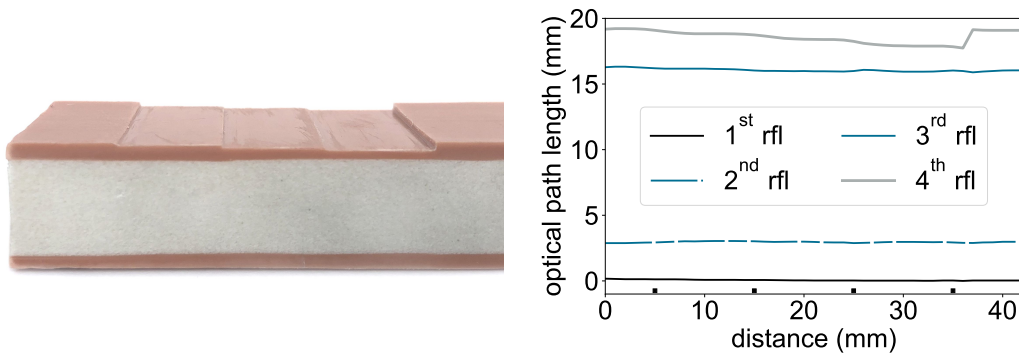


Figure 7.6: Photograph and evaluation of the stepped tube section measurement, ref.: reflector

Figure 7.7 depicts a magnified rescale on the range in approximation of the 4th boundary surface. It indicates that points close to the edges of the steps could not be accurately evaluated. For these points, sinc functions with different center frequencies were interfering in the frequency domain. They were weighted corresponding to the intensity of the Gaussian beam profile. Solely average frequency values could be determined for such positions. The correlation coefficient is lower at these points. For reliable results, a threshold of 0.99 indicated by the dotted line could be implemented to validate the results. For lower values, the evaluation could be classified as not valid.

In terms of future implementations of the measurement software, the optimization method of chapter 6 based on equidistant initial points could be applied to reduce the calculation load. Those were based on minimizing the ℓ^2 norm distance between modeled and measured signal. For such discontinuities, the correlation coefficient might be more suitable, since the resulting amplitudes vary in approximation of the step edges due to the superposition of sinc functions with different center frequencies. The normalization, which is inherently executed for the calculation of the correlation coefficient, can compensate for a certain degree of such

variations. However, in case the ℓ^2 was preferred, an additional normalization of the measured signal could be beneficial as well.

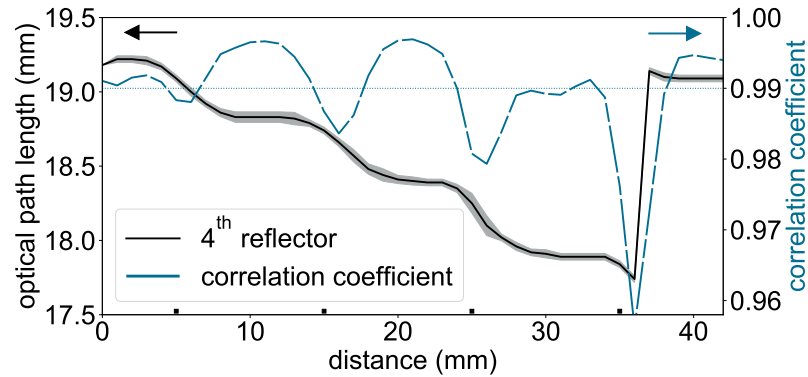


Figure 7.7: Optical path length of 4th reflector (left y-axis) and correlation coefficient (right y-axis), gray area corresponds to measurement uncertainty, dotted line indicates threshold of 0.99

7.2.3 Minimum Thickness

The previous chapters have shown, that the model-based approach enabled the evaluation of layers below the Rayleigh limit. However, the minimum measurable thickness has not been determined. Since this value is an important criterion for characterizing measurement processes and compare them to other methods, it is analyzed in the following.

Since the Rayleigh limit depends on the bandwidth and the approximate real part of the refractive index, the minimum measurable thickness is expected to be influenced by those values as well. An additional impact might be attenuation. It is assumed, that a reflection with a small amplitude cannot be as accurately separated by a second one as a stronger reflection: the distinction between a side lobe of a high peak and a second main lobe becomes more difficult when the amplitude decreases. A single layer is assumed to have a different resulting resolution limit than a composition of layers, because the amplitudes of the reflections are usually higher. Moreover, additional main and multiple reflections may interfere for multilayers.

However, to heuristically identify the order of the minimum measurable thickness in case of the model-based approach, a set of biaxially-oriented polyethylene terephthalate sheets has been measured. Their thicknesses are represented in Table 7.2 and vary from 291 μm to 72.7 μm . The thickest sample is depicted in Figure 7.8. It has been used as a reference to determine the refractive index. For both, TDS and FMCW, it resulted in 1.9. Hence, the Rayleigh limit equaled 2.03 mm. A step size of 1 μm for layers thicker or equal to 121 μm was used and a value of 0.5 μm for thinner sheets.

The measured thicknesses are presented in Table 7.2. In case of FMCW, a statistic of five single signals was measured for each thickness. For TDS, only one

measurement per sheet was performed. However, the uncertainty is estimated as $0.2\ \mu\text{m}$ corresponding to typical empirical values. The TDS results indicate that the refractive index could slightly vary between the different sheets.

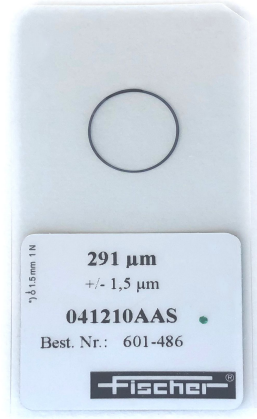


Figure 7.8: Biaxially-oriented polyethylene terephthalate reference sample-under-test

Table 7.2: Evaluated Thicknesses of Biaxially-Oriented Polyethylene Terephthalate Sheets

thickness (μm)	FMCW (μm)	TDS (μm)	search interval (μm)
291 ± 1.5	291 ± 4	291 ± 0.2	0 – 370
248 ± 1.5	240 ± 3	248.1 ± 0.2	0 – 370
243 ± 1.5	230 ± 3	246.8 ± 0.2	0 – 370
186 ± 1.5	195 ± 3	189.1 ± 0.2	0 – 370
186 ± 1.5	185 ± 3	189 ± 0.2	0 – 370
184 ± 1.5	180 ± 2	186 ± 0.2	0 – 370
125 ± 1.5	129 ± 3	126.9 ± 0.2	0 – 370
124 ± 1.5	120 ± 3	125.2 ± 0.2	0 – 370
121 ± 0.5	125 ± 2	122 ± 0.2	0 – 370
100.6 ± 0.5	111 ± 2	100.4 ± 0.2	0 – 190
100.4 ± 1	107 ± 2	100.5 ± 0.2	0 – 190
99.7 ± 1	109 ± 2	99.7 ± 0.2	0 – 190
72.7 ± 1	80 ± 3	73.9 ± 0.2	0 – 190

For FMCW, layers down to $121\ \mu\text{m}$ could be determined accurately with deviations of less than 4% in case of the model-based approach. For these values,

the measurement uncertainty equals roughly 1 – 2 %. Thinner layers were biased with offsets up to 10 %. Hence, it can be summarized, that thicknesses of down to roughly 6 % of the Rayleigh resolution limit could be determined.

7.2.4 Towards Lower Bandwidths

For industrial applications, in-line testing is the most effective inspection method to save costs and material resources. Therefore, it is beneficial to design measurement systems in way that they can be integrated into production lines. In dependency of the available space, compact sensors might be required for instance. FMCW radars are already available as monolithic microwave integrated circuits [112]–[114]. In this section, the potential of the model-based approach for such sensors is demonstrated.

While the monolithic microwave integrated circuit in [114] provides a bandwidth of up to 60 GHz, chips of 25.6 GHz [112] or only 6 GHz [113] tend to be less complex. They also show a tendency to enable faster rates due to the reduced bandwidth. Even commercial options such as cost-efficient and low power radars-on-chip and radars-in-package [115] are already available such as in automotive driver assistance systems with bandwidth of 4 GHz [116], [117]. Further sensors of 2 GHz [118] and 5 GHz [119] are announced to be launched in the near future. Due to the current developments towards autonomous vehicles [120], a further reduction of the costs as well as more flexible designs with regard to the bandwidth can be expected [115].

To analyze the impact of reduced bandwidths, the measurement signals of the tube section of Figure 7.6 are evaluated again. The parameters discussed in section 7.2.2 have been used. By cutting off samples at the origin and the end of the signal, the bandwidth is accordingly decreased. Evaluated thicknesses are represented in Figure 7.9 and 7.10 indicating that half of the bandwidth, 19.8 GHz, is sufficient for accurate results in case of this SUT. This result is remarkable, because cutting off the samples not only decreases the bandwidth but also reduces the ratio of signal and noise power. For a value of 9.9 GHz, the second and third boundary surfaces were determined with offsets for several distances.

To determine the reason for this bias, the measured signals for the distances 8 mm and 11 mm are exemplarily compared. For 8 mm, the accurate thickness could be determined, while for 11 mm an offset was observed for the second boundary surface. The corresponding signals are presented in Figure 7.11 indicating amplitude differences between the resulting peaks: the right peak in Figure 7.11 *left* is lower for 11 mm than for 8 mm. Such differences can be caused by any kind of nonidealities within the SUT such as variations of boundary surfaces. It seems as if small deviations from the ideal of homogeneous materials and plane-parallel interfaces are more significant for this case.

In case of reducing the bandwidth, the width of the peaks increased. For 9.9 GHz, the resulting Rayleigh limit even equals 15.2 mm. The amplitudes of the second and third peak appear to be lower than the first and fourth one: the contrast between the refractive indices of the single sample materials appears to be lower

than the contrast between outer layers and air. Therefore, the evaluation of second and third peaks may be more prone to the discussed influences on precision and accuracy.

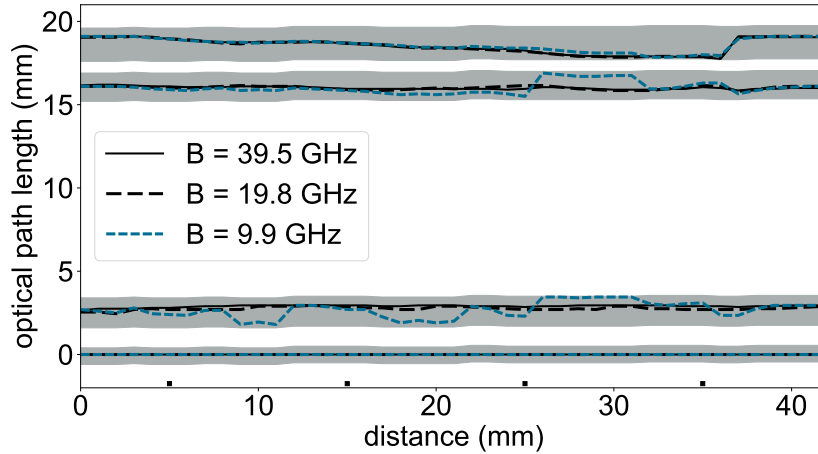


Figure 7.9: Optical path lengths of stepped tube section for reduced bandwidths, markers correspond to step edges

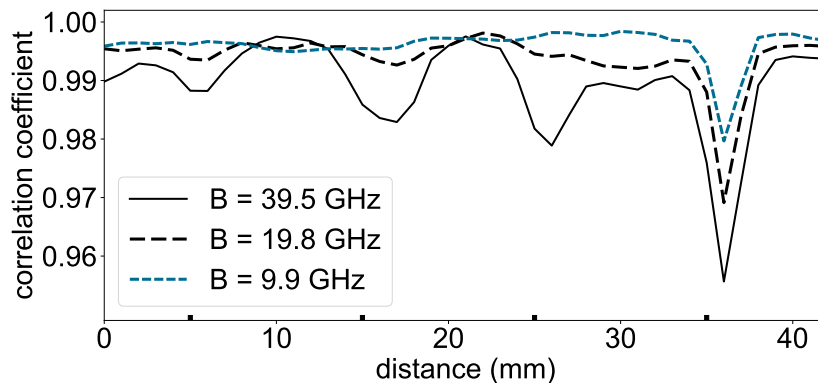


Figure 7.10: Correlation coefficient of stepped tube section for reduced bandwidths, marker correspond to step edges

Figure 7.10 depicts the calculated correlation coefficients. For some of the inaccurately evaluated positions for $B = 9.9$ GHz, the values are larger than the previously mentioned threshold of 0.99. Since the amplitudes of the second and third main reflections are rather low, the corresponding positions only have a minor influence on the correlation coefficient. In particular, for cases below the resolution limit, the remaining sum peak can also be modeled by a single reflection. Therefore, a coefficient above 0.99 cannot automatically serve as a quantity to guarantee an accurate result.

As described, Figure 7.9 shows that accurate results were observed for 19.8 GHz, while biased values occurred for 9.9 GHz. The difference between these two cases

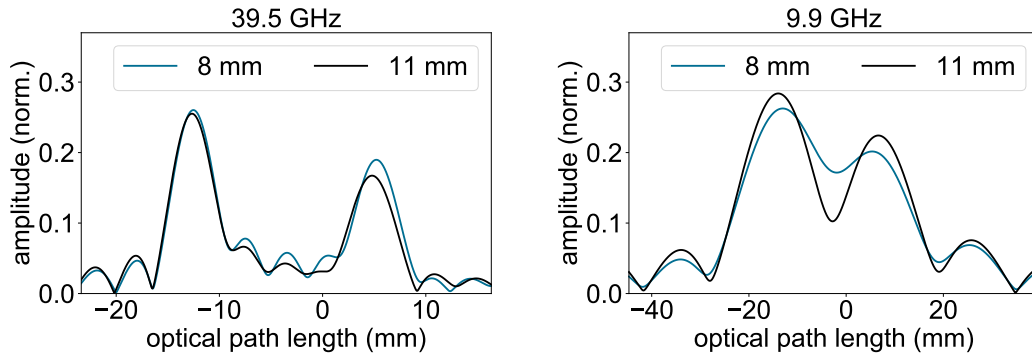


Figure 7.11: Measured signals corresponding to distances of 8 mm and 11 mm of Figure 7.9, from *left to right*, the bandwidth is reduced from 39.5 GHz to 9.9 GHz

is examined in the following. Figure 7.12 depicts measured signals for different bandwidths. For 19.8 GHz in *left*, two reflections respectively interfere to one separate peak resulting in 2 peaks for 4 reflections. In *right*, even the resulting peaks are interfering. The distance between one peak and its zero, the Rayleigh limit, equaled 15.2 mm for a bandwidth of for 9.9 GHz. For instance, for the second reflection, both the first and the third main peak are superposed. Therefore, the interference of three reflections appears to be a novel kind of resolution limit for multilayers applying the presented model-based signal processing: positions of boundary surfaces resulting in reflections with low amplitudes are likely to be inaccurately evaluated, if more than two peaks are closer than the Rayleigh limit.

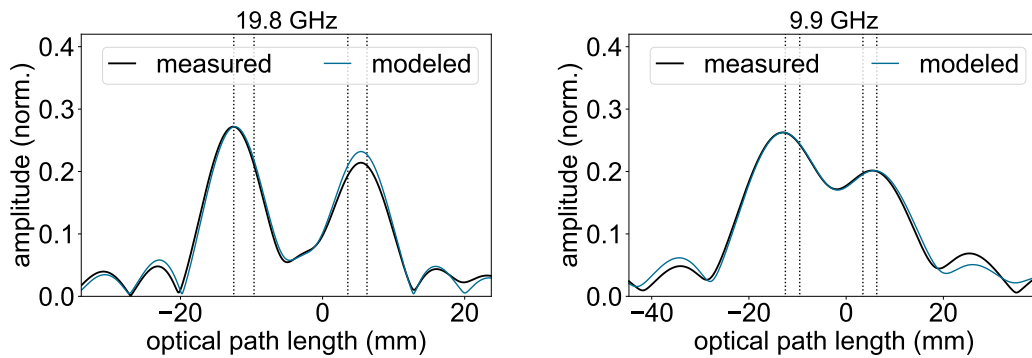


Figure 7.12: Measured and modeled signal at distances of 8 mm in case of reducing the bandwidth, reflector positions indicated by the modeled signal correspond to dotted lines, from *left to right* the processed bandwidth was reduced from 19.8 GHz to 9.9 GHz

However, the model-based approach enabled to accurately resolve layers of industrial samples in approximation and below the Rayleigh resolution limit as long as only two main peaks are superposed. Its potential for different industrial applications such as tube wall measurement has been illustrated and validated. For single-layered biaxially-oriented polyethylene terephthalate sheets,

thicknesses down to 120 μm were evaluated, which corresponds to only 6% of the Rayleigh resolution limit.

8. Summary and Outlook

The aim of this work has been to analyze the potential of frequency-modulated continuous-wave (FMCW) millimeter and terahertz waves for nondestructive thicknesses testing of multilayered dielectrics. For each boundary surfaces, additive oscillations with characteristic frequencies can be observed. The previous signal-processing method based on a frequency analysis using the Fourier transform was limited by the width of the peaks in the frequency domain. In this work an alternative model-based approach was therefore introduced, validated and applied.

The FMCW measurement principle and setup operating in the W band were presented. Based on the focusing unit, the lateral resolution was estimated as few millimeters. To prepare the signal for the processing, a calibration technique based on empty room and conducting plate standards was presented, e.g., to compensate for spurious reflections such as by the setup. It required analytical representations of the signals, which were calculated by a specifically designed finite-impulse response filter. In case of a Fourier transform frequency analysis, the width of one peak or rather the distance between the maximum and its zero was introduced as the Rayleigh depth resolution limit. It was determined by the bandwidth as well as the refractive index of the layer and typically equals few millimeters.

To determine layers below the Rayleigh limit spectral estimation algorithms were introduced. Based on a predefined model, they enable approaching the power spectral density of the measured signal based on few parameters, which have to be determined. Two algorithms, the modified covariance method and multiple signal classification (MUSIC), were chosen and analyzed for this application. The resulting peaks of the power spectral densities were observed to be thinner than the ones of the Fourier transform. However, the calibration of data and the noise level of the setup affected the required model order, which usually corresponds to the number of significant reflections. Hence, inaccurate results have been observed.

A promising alternative model-based method was introduced. It utilized a priori given thickness intervals and estimates of the refractive indices. A modeled signal is fitted to conform the measured data. Then, the parameters of the model indicate the requested thicknesses. For the most accurate calculation, the influence of multiple reflections was analyzed. In particular, for high refractive indices contrasts and for conducting substrates, their impact was significant. To calcu-

late multiple reflections efficiently, a modification of a transfer matrix method was introduced, which solely observed the propagation effects on the measured signal instead of calculating the complete electromagnetic wave propagation. A comparison of the different signal-processing methods indicated, that the model-based approach was the only solution for reliable thickness evaluation below the Rayleigh depth resolution limit.

To characterize the quality of the results, the terms accuracy and precision were introduced, which respectively describe the bias and the repeatability of results. The different setup influences and their effect on these quantities have been discussed. The theoretical minimum of the variance, the Cramér-Rao lower bound, was derived and validated particularly for FMCW distance and thickness measurements. Depending on the signal-to-noise ratio of the setup and the refractive indices of the layers, it typically equaled a standard deviation of several micrometers. The comparison to other frequency or phase evaluation [53] algorithms indicated, that the highest precision for distance and thickness measurements was achieved by the model-based approach.

The calculation load of the model-based approach was significantly higher than the ones of other methods because the first implementation utilized exhaustive search for the fitting process. For compensation, in the first step, parallel computing on a general-purpose graphics processing unit was utilized exemplarily reducing the calculation time to less than 2s for a presented three-layered tube section instead of hours for a central processing unit. However, optimization algorithms were analyzed as more efficient alternatives for future setups. Unlike promising results for time-domain spectroscopy [38] or vector network analysis [46], genetic algorithms have been observed to deliver biased thickness values for FMCW due to approaching local minima. Hence, typical solution spaces were analyzed. Numerous, apart from interference effects, equidistant local minima were observed. For a novel specific optimization strategy, the average distance of two adjacent minima was derived for the presented system using Fourier transform equivalences, which resulted in a value of 1.7 mm. Then, a set of equidistant initial points enabled approaching the respectively closest optimum based on the steepest descent or Nelder-Mead algorithm. The procedure has been validated by measurements. The strategy enabled to identify almost all local minima determined by exhaustive search for the presented examples. The most accurate and precise results could be achieved by the Nelder-Mead algorithm.

Finally, the potential of the model-based approach for being used in future applications was presented including measurements of industrial samples such as multilayered tube wall sections. The bandwidths of the measured signals was also virtually reduced to replicate measurement conditions of compact radars (with usually lower bandwidth), which could be used for future systems.

To resolve thicknesses below the respective limits, utilizing model-based signal processing has been applied before such as for ultrasonic [28], terahertz time-domain spectroscopy [38], and vector network analysis [46] systems. However, a combination of different findings is novel and promoted researching distinctive

aspects published in [1]–[22].

- The Cramér-Rao lower bound was derived for FMCW thickness measurements [6] taking a special consideration on the dependency of frequency and zero phase of the signal's oscillations. Both quantities are processed simultaneously in case of the model-based approach and their relation can therefore not be neglected. Unlike former work [53], [95], more accurate estimates of the minimum variance could be provided.
- A modification of a transfer matrix method was derived particularly for FMCW to efficiently calculate multiple reflections. Due to the significantly reduced calculation load, the modified transfer matrix method is an important step towards the requirements of industrial applications: instead of millions solely 1700 data points had to be calculated for the presented setup.
- A novel method for optimizing the adaptation of the model has been presented, based on the observation of numerous rather equidistant minima of representative solution spaces. The calculation time for a central processing unit was significantly reduced, e.g., from 66 h to less than 1 min for a two-layered sample-under-test. The obtained results were more precise and accurate than the ones for a comparing genetic algorithm.
- Different dielectric materials such as ceramics [9], acrylics, and recycle foams have been tested, which validated the model-based approach. Besides ideal plane-parallel objects, industrial samples such as multilayer tube walls have been measured identifying thickness variations. The minimum measurable thickness of the model-based approach depends on the refractive indices of the materials. However, for single-layered biaxially-oriented polyethylene terephthalate sheets, a value of 120 μm was evaluated, which corresponds to 6 % of the Rayleigh resolution limit. For multilayers, the superposition of three peaks was heuristically determined to be an additional limitation: for closer peaks, biased values can be observed.

While the model-based approach of this work is a significant step towards reliable thickness measurements based on FMCW, additional process is required for industrial applications. To reduce the computation time, the presented optimization procedure could be implemented for the graphic processors, which have already been used for exhaustive search. This step could be the basis to enhance the usability of the processing software. So far, estimates of the refractive indices have been required for the evaluation. In case the optimization algorithm expands for additional variables, the material parameters could be fitted simultaneously with the thicknesses requiring less a priori information or additional measurements.

Accurate results have been obtained, by approaching the refractive indices by constant values. However, measuring the frequency dependency of them should further increase the accuracy and potentially expand the approach for even thinner layers. Such measurements could be performed by vector network analysis,

by FMCW reference measurements using a priori information of the thicknesses, or by measuring different angles of incidence.

In terms of future setup configurations, it had been shown, that even a bandwidth of 20 GHz is sufficient for samples such as the presented tube walls. The model-based approach could be implemented for one of the available monolithic microwave integrated circuit solutions [112]–[114] to step toward the realization of compact measurement systems. For the processing, developments in terms of computers are expected to offer more time and cost-efficient solution in the near future: on the one hand, for graphics processing units, sizes and costs are continuously reducing. Simultaneously, the computation performance increases: the number of operations has roughly doubled within 4 years [121]. On the other hand, the increasing number of cores of central processing units [122] could be sufficient for a fast parallel implementation of the optimization approach within the next years. Developments of multicore embedded chips [123] might even enable the realization of fully integrated radar and signal-processing solutions.

List of Abbreviations

ADC	analog-to-digital converter
AWGN	additive white Gaussian noise
AWGPN	additive white Gaussian phase noise
CPU	central processing unit
CRLB	Cramér-Rao lower bound
DAC	digital-to-analog converter
DFT	discrete Fourier transform
FIR	finite impulse response, digital filter
FMCW	frequency-modulated continuous-wave
GP-GPU	general-purpose graphics processing unit
MUSIC	multiple signal classification
PDF	probability density function
SNR	signal-to-noise ratio
SUT	sample-under-test
TDS	time-domain spectroscopy
TMM	transfer matrix method

List of Variables, Symbols, and Operators

The physical quantities conform to the International System of Units (SI) [58].

\cdot^*	complex conjugate
$\{\cdot\}^T$	transpose of matrix or vector
$\hat{\cdot}$	estimated value
$\bar{\cdot}$	arithmetic mean
$ \cdot $	calculation of absolute value
$\mathbf{E}\{\cdot\}$	expectation value
$\mathcal{H}\{\cdot\}$	discrete Hilbert transform
$\max(\cdot)$	calculation of maximum
$\Re\{\cdot\}$	extraction of real part of a complex value
$\text{var}(\cdot)$	variance
α^i	step size of the i^{th} iteration
β	scaling coefficient of the backtracking line search algorithm
$\gamma = \frac{1}{2}$	contraction parameter of Nelder-Mead algorithm
$\delta[n]$	digital Dirac distribution
$\underline{\eta} = \eta + j \cdot \kappa$	complex refractive index
η	real part of refractive index $\underline{\eta}$
θ	focal length
$\Theta[n]$	Heaviside function
$\iota(d, r)$	intensity of axial distance d and radial distance from the center axis r
κ	imaginary part of refractive index $\underline{\eta}$
λ	wavelength
ξ	amplitude ratio
$\rho = 1$	reflection parameter of Nelder-Mead algorithm
$\sigma = \frac{1}{2}$	shrinking parameter of Nelder-Mead algorithm
σ_n	variance of noise
σ_R	scale parameter of Rayleigh distribution

σ_x	variance of random variable X
τ	time delay of one reflection
$\boldsymbol{\tau} = (\tau_1, \tau_2, \dots, \tau_L)$	vector of time delays
τ_l	time delay of the l^{th} reflection
$\varphi_n(t)$	phase noise
ϕ	zero phase
$\chi = 2$	expansion parameter of Nelder-Mead algorithm
$\omega[n]$	sample function of noise
a	amplitude of a reflection
$\underline{a}_1, \underline{a}_2, \dots, \underline{a}_p$	spectral estimation coefficient
$\mathbf{a} = (a_1, a_2, \dots, a_L)$	vector of amplitudes
a_l	amplitude of the l^{th} reflection
b	zeros of filters or pseudo spectra
B	bandwidth of frequency modulation
c_0	vacuum speed of light
d	axial distance
\mathbf{d}^i	descent direction of i^{th} iteration of gradient descent
\mathbf{D}^i	positive definite matrix for calculation of \mathbf{d}^i
d_N	Nyquist distance
d_R	Rayleigh length
F_1	start frequency of frequency modulation
f_b	beat frequency
$f_{b,l}$	beat frequency of the l^{th} reflection
f_s	sampling frequency
g	cost function
g_{ℓ^p}	cost function of ℓ^p norm
\mathbf{H}_g	Hessian matrix of cost function g
i	index of the iteration
I	total number of iterations
$\mathbf{I}(\boldsymbol{\tau})$	Fischer information matrix
j	imaginary unit

k	index of digital frequency
l	index of the reflection
L	total number of reflections
ℓ^p	norm of order p
M	rank of auto-correlation matrix
n	index of time sample
N	total number of time samples
p	order of norm, order of frequency estimation model
p_x	probability density function of X
q	order of FIR filter
r	radial distance
Δr_R	Rayleigh depth resolution limit
r_P	Pearson correlation coefficient
$\underline{r}_{l,l+1}$	Fresnel reflection coefficient
$r_{l,l+1}$	real approximation of $\underline{r}_{l,l+1}$
$r_x[v]$	auto-correlation function
$r_x(v, \nu)$	(modified) covariance function for time samples v and ν
\mathbf{R}_x	auto-correlation matrix of signal x
$\underline{s}[n]$	analytic representation of signal $s[n]$
$s[n]$	real representation of signal
SNR_E	time-domain ensemble signal-to-noise ratio
SNR_S	time-domain sample function signal-to-noise ratio
t	continuous time
T	duration of frequency modulation
$\underline{t}_{l,l+1}$	Fresnel transmission coefficient
$t_{l,l+1}$	real approximation of $\underline{t}_{l,l+1}$
w	beam radius
w_0	beam waist
X	random variable
x	value of random variable
$x[n]$	superposition of ideal signal and noise, real representation

$\underline{x}[n]$	superposition of ideal signal and noise, analytic representation
$\underline{x}_m[n]$	m^{th} sample function

List of Figures

2.1	Schematic of multilayered sample-under-test and relation of frequency-modulated continuous-wave quantities	9
2.2	Schematic of a frequency-modulated continuous-wave setup	10
2.3	Schematic of focused Gaussian beam	12
2.4	Schematic of reflections by plane and curved boundary surfaces	13
2.5	Preprocessing procedure	13
2.6	FIR-based preprocessing procedure	15
2.7	Frequency response of a finite impulse response Hilbert filter	15
2.8	Influence of calculating an analytic representation of an ideal signal	16
2.9	Empty room and conducting plate calibration standards	16
2.10	Interference of simulated signal portions and thickness error by peak detection	18
2.11	Example of high conformity between modeled signals of different thicknesses	19
3.1	Pseudo spectra of modified covariance method using different model orders	26
3.2	Evaluated positions of MUSIC algorithm and modified covariance method	26
3.3	Evaluated distance error without the presence of noise	28
3.4	Evaluated distance error in the presence of additive white Gaussian noise	28
4.1	Comparison of reference and modeled signal, solution space	33
4.2	Influence of the first one of the multiple reflections on peak detection varying the refractive indices	34
4.3	Influence of the first one of the multiple reflections on peak detection results varying the bandwidth	35
4.4	Thickness error by interference using peak detection	36
4.5	Notation of transfer matrix method, each layer corresponds to a quadrupole	37
4.6	Comparison of classical and modified transfer matrix method for an FMCW setup	37
4.7	Photograph of acrylic sample-under-test	40
5.1	Accuracy and precision of a random variable	44

5.2	Block diagram of measurement system and processing indicating noise sources	45
5.3	Simulated signal disturbed by additive white Gaussian phase noise	46
5.4	Comparison of peaks in the presence of Rayleigh and Brownian motion noise	47
5.5	Histogram of amplitude differences caused by phase noise and histogram of evaluated distances	48
5.6	Ensembles and sample functions	48
5.7	Ensemble average, standard deviation and signal-to-noise ratio . .	49
5.8	Histogram and quantile-quantile plot of real part of the measured signal for single time index	50
5.9	Quantile-quantile plot of the imaginary part of the measured signal for single time index	51
5.10	Average values and signal-to-noise ratio of sample functions . . .	52
5.11	Quantile-quantile plot of a single measured signal	52
5.12	Cramér-Rao lower bound as a function of the optical path length	55
5.13	Statistic distances evaluation based on simulated and measured signal	58
5.14	Photograph of the Pertinax sample-under-test	59
5.15	Statistic of 500 optical path lengths based on simulated and measured signals	60
6.1	Solution space of the correlation coefficient	65
6.2	Solution space of the ℓ^2 distance	66
6.3	Solution space of the ℓ^1 distance	66
6.4	Solution space of the ℓ^∞ distance	67
6.5	Solution space varying the optical path length	68
6.6	Solution space varying the amplitude of second reflection	68
6.7	Real parts of signals shifting the phase	70
6.8	Optimization based on a set of equidistant initial points	71
6.9	Step size of steepest descent and principle of backtracking line search	72
6.10	Comparison of steepest descent including backtracking line search with utilizing a constant step size	74
6.11	Adaption of simplex within the solution space	75
6.12	Adaptation of a simplex of Nelder-Mead algorithm	75
6.13	Float diagram and solution space of the genetic algorithm	77
6.14	Comparison of final values of different optimization algorithms . .	80
6.15	Evaluated global optima of 100 independent simulations	81
6.16	Photograph of acrylic samples-under-test	82
7.1	Reflection mode setup for rotations measurements	88
7.2	Photographs of a multilayered tube sample-under-test	89
7.3	Adapted search intervals of circumference measurement	90
7.4	Circumference measurement of tube section	91
7.5	Polar representation of circumference measurement results	91
7.6	Photograph and evaluation of the stepped tube section measurement	92

7.7	Correlation coefficient of stepped tube section	93
7.8	Biaxially-oriented polyethylene terephthalate reference sample-under-test	94
7.9	Optical path lengths of stepped tube section for reduced bandwidths	96
7.10	Correlation coefficient of stepped tube section for reduced bandwidths	96
7.11	Measured signals utilized for Figure 7.9	97
7.12	Measured and modeled signal in case of reducing the bandwidth .	97

List of Tables

2.1	Estimated Upper Limit of Rayleigh Length and Beam Waist . . .	12
4.1	Evaluated Thickness of Acrylic Sheet	40
4.2	Evaluated Optical Path Lengths of Different Signal-Processing Algorithms	41
4.3	Characteristics of Signal-Processing Algorithms	42
5.1	Analysis of Ensemble Characteristic of the Resulting Noise	51
5.2	Analysis of Sample Function Characteristic of the Resulting Noise	52
5.3	Precision of Distance Evaluations based on Simulations	58
5.4	Precision of Distance Evaluations based on Measurements	59
5.5	Precision of Thickness Evaluations based on Simulations	60
5.6	Precision of Thickness Evaluations based on Measurements	60
6.1	Example of Initial Population of a Genetic Algorithm	78
6.2	Exemplary Set of Children before and after Mutation	78
6.3	Random Chromosome	79
6.4	Results of Optimization Algorithms Evaluating Simulated Data .	81
6.5	Values of Optimization Algorithms after 25 Iterations Evaluating Simulated Data	82
6.6	Results of Optimization Algorithms Evaluating Measurements of Acrylic Sheets	83
6.7	Results of Optimization Algorithms Evaluating Two-Layered Sample	84
6.8	Summarizing Comparison of Optimization Algorithms	85
7.1	Parameters of the Rotation Measurement Setup	88
7.2	Evaluated Thicknesses of Biaxially-Oriented Polyethylene Terephthalate Sheets	94

List of Publications

Scientific Articles

- [1] N. Schreiner, W. Sauer-Greff, R. Urbansky, G. von Freymann, and F. Friederich, "Multilayer Thickness Measurements below the Rayleigh Limit Using FMCW Millimeter and Terahertz Waves," *Sensors*, vol. 19, no. 18, Sep. 2019.
- [2] N. Schreiner, A. Keil, W. Sauer-Greff, R. Urbansky, and F. Friederich, "Comparison of Signal Processing Algorithms for High-Resolution FMCW Terahertz Thickness Measurements," *Journal of Physics: Conference Series*, vol. 1537, Jun. 2020.
- [3] J. Klier, G. Torosyan, N. Schreiner, D. Molter, F. Ellrich, W. Zouaghi, E. Peytavit, J. Lampin, R. Beigang, J. Jonuscheit, and G. von Freymann, "Influence of Substrate Material on Radiation Characteristics of THz Photoconductive Emitters," *International Journal of Antennas and Propagation*, Sep. 2015.
- [4] F. Ellrich, M. Bauer, N. Schreiner, A. Keil, T. Pfeiffer, J. Klier, S. Weber, J. Jonuscheit, F. Friederich, and D. Molter, "Terahertz Quality Inspection for Automotive and Aviation Industries," *Journal of Infrared, Millimeter, and Terahertz Waves*, Nov. 2019.

Peer-Review Conference Contributions

- [5] N. Schreiner, B. Baccouche, W. Sauer-Greff, R. Urbansky, and F. Friederich, "High-Resolution FMCW Millimeter-Wave and Terahertz Thickness Measurements," in *Proceedings of the 47th European Microwave Conference*, Nuremberg, Germany, Oct. 2017, pp. 1187–1190.
- [6] N. Schreiner, W. Sauer-Greff, R. Urbansky, and F. Friederich, "Analyzing the Precision of Frequency Modulated Continuous Wave Distance and Thickness Measurements," in *Proceedings of the 16th European Radar Conference*, Paris, France, Oct. 2019, pp. 45–48.

- [7] N. Schreiner, M. Bortz, W. Sauer-Greff, R. Urbansky, and F. Friederich, "Optimization Algorithms for Accurate FMCW Millimeter Wave and Terahertz Thickness Measurements," in *Proceedings of the 50th European Microwave Conference*, Poster Pitch Award, Utrecht, the Netherlands, Jan. 2021.

Conference Proceedings

- [8] N. Schreiner, B. Baccouche, W. Sauer-Greff, R. Urbansky, and F. Friederich, "Fast Thickness Measurements with Frequency Modulated Continuous Wave Terahertz Radiation," in *Proceedings of the 41st International Conference on Infrared, Millimeter, and Terahertz Waves*, Copenhagen, Denmark, Sep. 2016.
- [9] N. Schreiner, B. Baccouche, D. Molter, W. Sauer-Greff, R. Urbansky, and F. Friederich, "A Transfer Matrix Modification for Accurate Terahertz FMCW Thickness Measurements," in *Proceedings of the 10th UK-Europe-China Workshop on Millimetre Waves and Terahertz Technologies*, Best Student Paper, Liverpool, UK, Sep. 2017.
- [10] N. Schreiner, W. Sauer-Greff, R. Urbansky, and F. Friederich, "All-Electronic High-Resolution Terahertz Thickness Measurements," in *Proceedings of the 43rd International Conference on Infrared, Millimeter, and Terahertz Waves*, Nagoya, Japan, Sep. 2018.
- [11] N. Schreiner, S. Weber, A. Keil, and F. Friederich, "Mobile Handheld FMCW Terahertz Multilayer Thickness Inspection," in *Proceedings of the 44th International Conference on Infrared, Millimeter, and Terahertz Waves*, Paris, France, Sep. 2019.
- [12] A. Keil, N. Schreiner, and F. Friederich, "Thickness Measurements with Multistatic Sparse Arrays," in *Proceedings of the 43rd International Conference on Infrared, Millimeter, and Terahertz Waves*, Nagoya, Japan, Sep. 2018.

Other Contributions

- [13] N. Schreiner, and F. Friederich, *Thickness Measurements of Tube Walls Using Frequency-Modulated Continuous-Wave Terahertz-Systems*, 7th International Workshop on Terahertz Technology and Applications, Kaiserslautern, Germany, Mar. 2016.
- [14] N. Schreiner, B. Baccouche, W. Sauer-Greff, R. Urbansky, and F. Friederich, *An Accurate Frequency-Modulated Continuous-Wave Method for Fast Terahertz Thickness Measurements*, Photonics West, San Francisco, California, USA, Jan. 2017.

-
- [15] N. Schreiner, and F. Friederich, *Dickenmessungen mittels Terahertz-Radar*, DGZfP Jahrestagung, Koblenz, Germany, May 2017.
 - [16] N. Schreiner, W. Sauer-Greff, R. Urbansky, and F. Friederich, *Multilayer Thickness Inspection with Millimeter-Waves*, Photonics West, San Francisco, California, USA, Mar. 2018.
 - [17] N. Schreiner, R. Hussung, C. Cappel, W. Sauer-Greff, R. Urbansky, and F. Friederich, *Accurate Terahertz FMCW Thickness Measurements*, 8th International Workshop on Terahertz Technology and Applications, Kaiserslautern, Germany, Mar. 2018.
 - [18] N. Schreiner, W. Sauer-Greff, R. Urbansky, and F. Friederich, *Multilayer Thickness Measurements below the Rayleigh Limit Using FMCW Millimeter and Terahertz Waves*, Kleinheubacher Tagung, Miltenberg, Germany, Sep. 2018.
 - [19] N. Schreiner, A. Keil, and F. Friederich, *Mobile Handheld FMCW Terahertz Multilayer Thickness Inspection*, French-German Terahertz Conference, Kaiserslautern, Germany, Apr. 2019.
 - [20] N. Schreiner, S. Weber, A. Keil, and F. Friederich, *FMCW Thickness Evaluation with a Mobile Hand-Held Terahertz System*, Photonics West, San Francisco, California, USA, Feb. 2020.
 - [21] N. Schreiner, and F. Friederich, *Multilayer Thickness Inspection with W Band FMCW-Radar*, 9th International Workshop on Terahertz Technology and Applications, Kaiserslautern, Germany, Mar. 2020.
 - [22] F. Friederich, C. Cappel, and N. Schreiner, *FMCW Terahertz Multilayer Thickness Determination below the Resolution Limit*, Photonics West, San Francisco, California, USA, Feb. 2019.

Bibliography

- [23] C. Lebowitz, and L. Brown, “Ultrasonic Measurement of Pipe Thickness,” *Review of Process in Quantitative Nondestructive Evaluation*, vol. 12, pp. 1987–1994, 1993.
- [24] J. Moulder, E. Uzal, and J. Rose, “Thickness and Conductivity of Metallic Layers from Eddy Current Measurements,” *Review of Scientific Instrument*, vol. 63, pp. 3455–3465, Jun. 1992.
- [25] W. Yin, and A. Peyton, “Thickness Measurement of Non-Magnetic Plates Using Multi-Frequency Eddy Current Sensors,” *NDT&E International*, vol. 40, pp. 43–48, Sep. 2006.
- [26] A. Sagalakov, S. Dmitriev, and V. Malikov, “Superminiature Eddy-Current Transducers for Thickness Studies,” *IOP Conference Series: Materials Science and Engineering*, vol. 262, Nov. 2017.
- [27] J. Park, J. Kim, H. Ahn, J. Bae, and J. Jin, “A Review of Thickness Measurements of Thick Transparent Layers Using Optical Interferometry,” *International Journal of Precision Engineering and Manufacturing*, vol. 20, pp. 463–477, Mar. 2019.
- [28] A. Abbate, N. Nguyen, S. LaBreck, and T. Nelligan, “Ultrasonic Signal Processing Algorithms for the Characterization of Thin Multilayers,” *NDT.net*, vol. 7, no. 10, pp. 23–30, Oct. 2002.
- [29] G. Hayward, and J. Lewis, “Comparison of Some Non-Adaptive Deconvolution Techniques for Resolution Enhancement of Ultrasonic Data,” *Ultrasonics*, vol. 27, pp. 155–164, May 1989.
- [30] O. Lenoir, J. Izbicki, M. Rousseau, and F. Coulouvrat, “Subwavelength Ultrasonic Measurement of a Very Thin Fluid Layer Thickness in a Tri-layer,” *Ultrasonics*, vol. 35, no. 7, pp. 509–515, Nov. 1997.
- [31] Balluff, *Products for Efficient Automation, Products and Services, Sensors 2*, Neuhausen auf den Fildern, Germany, 2020.
- [32] A. Koelpin, F. Lurz, S. Linz, S. Mann, C. Will, and S. Lindner, “Six-Port Based Interferometry for Precise Radar and Sensing Applications,” *Sensors*, vol. 16, no. 10, Sep. 2016.
- [33] M. Bhardwaj, “High Transduction Piezoelectric Transducers and Introduction of Non-Contact Analysis,” *NDT.net*, vol. 5, no. 1, Jan. 2000.

-
- [34] D. Bohn, "Environmental Effects on the Speed of Sound," *Journal of the Audio Engineering Society*, vol. 36, no. 4, Apr. 1988.
- [35] *VDI/VDE 5590, Terahertz Systems: Terms and Definitions*, Dusseldorf, Germany: VDI/VDE, Mar. 2018.
- [36] B. Hu, and M. Nuss, "Imaging with Terahertz Waves," *Optics Letters*, vol. 20, no. 16, pp. 1716–1718, Aug. 1995.
- [37] H. Auston, P. Lavallard, N. Sol, and D. Kaplan, "An Amorphous Silicon Photodetector for Picosecond Pulses," *Applied Physics Letters*, vol. 66, no. 36, pp. 66–68, Oct. 1980.
- [38] S. Krimi, J. Klier, J. Jonuscheit, G. von Freymann, R. Urbansky, and R. Beigang, "Highly Accurate Thickness Measurement of Multi-Layered Automotive Paints Using Terahertz Technology," *Applied Physics Letters*, vol. 109, pp. 021105–1 – 021105–4, Jul. 2016.
- [39] G. Walker, J. Bowen, J. Labaune, J. Jackson, S. Hadjiloucas, J. Roberts, G. Mourou, and M. Menu, "Terahertz Deconvolution," *Optics Express*, vol. 20, no. 25, pp. 27 230–27 241, Nov. 2012.
- [40] J. Dong, A. Locquet, and D. Citrin, "Depth Resolution Enhancement of Terahertz Deconvolution by Autoregressive Spectral Extrapolation," *Optics Letters*, vol. 42, no. 9, pp. 1828–1831, May 2017.
- [41] A. Pourkazemi, W. Ranson, J. Stiens, M. Becquaert, and M. Vandewal, "Novel Illumination and Parameter Extraction Technique for the Characterization of Multilayer Structures in the GHz Range with Deep Sub-Wavelength Resolution," in *15th Mediterranean Microwave Symposium*, Lecce, Italy, Nov. - Dec. 2015.
- [42] TeraView. "TeraPulse Lx." (Jan. 2021), [Online]. Available: <https://teraview.com/terapulselx/>.
- [43] *Millimeter Wave Propagation: Spectrum Management Implications*, Washington, District of Columbia, USA: Federal Communications Commission Office of Engineering and Technology, 1997.
- [44] S. Mann, C. Will, T. Reissland, F. Lurz, S. Lindner, S. Linz, R. Weigel, and A. Koelpin, "High-Precision Interferometric Radar for Sheet Thickness Monitoring," *IEEE Transactions on Microwave Theory and Techniques*, vol. 66, no. 6, pp. 3153–3166, Jun. 2018.
- [45] D. Pozar, *Microwave Engineering*, 4th ed. Hoboken, New Jersey, USA: John Wiley & Sons, 2012.
- [46] T. Zwick, J. Haala, and W. Wiesbeck, "A Genetic Algorithm for the Evaluation of Material Parameters of Compound Multilayered Structures," *IEEE Transactions on Microwave Theory and Techniques*, vol. 50, no. 4, pp. 1180–1187, Apr. 2002.

-
- [47] T. Tosaka, K. Fujii, K. Fukunaga, and A. Kasamatsu, "Development of Complex Relative Permittivity Measurement System Based on Free-Space in 220–330-GHz Range," *IEEE Transactions on Terahertz Science and Technology*, vol. 5, no. 1, pp. 102–109, Jan. 2015.
- [48] N. Gagnon, J. Shaker, P. Berini, L. Roy, and A. Petosa, "Material Characterization Using a Quasi-Optical Measurement System," *IEEE Transactions on Instrumentation and Measurement*, vol. 52, no. 2, pp. 333–336, Apr. 2003.
- [49] D. Ellerbruch, and D. Belsher, "Electromagnetic Technique of Measuring Coal Layer Thickness," *IEEE Transactions on Geoscience Electronics*, vol. GE-16, no. 2, pp. 126–133, Apr. 1978.
- [50] J. Holmgren, M. Sturm, N. Yankielun, and G. Koh, "Extensive Measurements of Snow Depth Using FM-CW Radar," *Cold Regions Science and Technology*, vol. 27, pp. 17–30, Feb. 1998.
- [51] S. Gütgemann, C. Krebs, A. Küter, D. Nüßler, B. Fischer, and H. Krauthäuser, "Radar-Based High Precision Thickness Measurements for Rolling Mills," in *Proceedings of the 15th European Radar Conference*, Madrid, Spain, Sep. 2018, pp. 122–125.
- [52] M. Skolnik, *Introduction to Radar Systems*, 2nd ed. Singapore, Republic of Singapore: McGraw-Hill, Inc, 1988.
- [53] S. Scherr, S. Ayhan, B. Fischbach, A. Bhutani, M. Pauli, and T. Zwick, "An Efficient Frequency and Phase Estimation Algorithm with CRB Performance for FMCW Radar Applications," *IEEE Transactions on Instrumentation and Measurement*, vol. 64, no. 7, pp. 1868–1875, Jul. 2015.
- [54] R. Ebel, D. Shmakov, and M. Vossiek, "The Effect of Phase Noise on Ranging Uncertainty in FMCW Secondary Radar-Based Local Positioning Systems," in *Proceedings of the 9th European Radar Conference*, Amsterdam, Netherlands, Oct.–Nov. 2012, pp. 258–261.
- [55] K. Thurn, R. Ebel, and M. Vossiek, "Noise in Homodyne FMCW Radar Systems and Its Effects on Ranging Precision," in *International Microwave Symposium Digest*, Seattle, Washington, USA, Jun. 2013.
- [56] A. Stelzer, M. Jahn, and S. Scheiblhofer, "Precise Distance Measurement with Cooperative FMCW Radar Units," in *IEEE Radio and Wireless Symposium*, Orlando, Florida, USA, Jan. 2008, pp. 771–774.
- [57] A. Stelzer, and M. Pichler, "Resolution Enhancement with Model-Based Frequency Estimation Algorithms in Radar Signal Processing," *Subsurface Sensing Technologies and Applications*, vol. 4, no. 3, pp. 241–261, Jul. 2003.
- [58] Bureau International des Poids et Mesures, *The International System of Units*, 9th ed, Sèvres, France, 2019.
- [59] E. Hecht, *Optik*, 5th ed. Oldenbourg, Germany: De Gruyter, 2009.

-
- [60] J. Detlefsen, A. Dallinger, S. Schelkshorn, and S. Bertl, "UWB Millimeter-Wave FMCW Radar Using Hilbert Transform Methods," in *IEEE 9th International Symposium on Spread Spectrum Techniques and Applications*, Manaus-Amazon, Brazil, Aug. 2006, pp. 46–48.
- [61] H. Pickett, J. Hardy, and J. Farhoomand, "Characterization of a Dual-Mode Horn for Submillimeter Wavelengths," *IEEE Transactions on Microwave Theory and Techniques*, vol. MTT-32, no. 8, pp. 936–937, Aug. 1984.
- [62] A. Oppenheim, and R. Schafer, *Digital Signal Processing*. Englewood Cliffs, New Jersey, USA: Prentice-Hall, Inc., 1975.
- [63] MATLAB. "Design Digital Filters." (Jul. 2020), [Online]. Available: <https://de.mathworks.com/help/signal/ref/designfilt.html>.
- [64] F. Smith, B. Chambers, and J. Bennett, "Calibration Techniques for Free Space Reflection Coefficient Measurements," *IEE Proceedings A*, vol. 139, no. 5, pp. 247–253, Sep. 1992.
- [65] F. Harris, "On the Use of Windows for Harmonic Analysis with the Discrete Fourier Transform," *Proceedings of the IEEE*, vol. 66, no. 1, pp. 51–83, Jan. 1978.
- [66] J. Proakis, and D. Manolakis, *Digital Signal Processing: Principles, Algorithms, and Applications*, 3rd ed. Upper Saddle River, New Jersey, USA: Prentice-Hall, Inc., 1996.
- [67] S. Kay, and S. Marple, "Spectrum Analysis — A Modern Perspective," *Proceedings of the IEEE*, vol. 69, no. 11, pp. 1380–1419, 1981.
- [68] G. Brooker, "Understanding Millimetre Wave FMCW Radars," in *1st International Conference on Sensing Technology*, Palmerston North, New Zealand, Nov. 2005, pp. 152–157.
- [69] M. Hayes, *Statistical Digital Signal Processing and Modeling*. Hoboken, New Jersey, USA: John Wiley & Sons, 1996.
- [70] S. Olbrich, and C. Waldschmidt, "New Pre-Estimation Algorithm for FMCW Radar Systems Using the Matrix Pencil Method," in *Proceedings of the 12th European Radar Conference*, Paris, France, Sep. 2015, pp. 177–180.
- [71] M. Abou-Khousa, D. Simms, S. Kharkovsky, and R. Zoughi, "High-Resolution Short-Range Wideband FMCW Radar Measurements Based on MUSIC Algorithm," in *Instrumentation and Measurement Technology Conference*, Singapore, Republic of Singapore, May 2009.
- [72] P. Gulden, M. Vossiek, E. Storck, and P. Heide, "Application of State Space Frequency Estimation Techniques to Radar Systems," in *International Conference on Acoustics, Speech, and Signal Processing*, Salt Lake City, Utah, USA, May 2001, pp. 2877–2880.

-
- [73] D. Oh, and J. Lee, “Low-Complexity Range-Azimuth FMCW Radar Sensor Using Joint Angle and Delay Estimation without SVD and EVD,” *IEEE Sensors Journal*, vol. 15, no. 9, pp. 4799–4811, Sep. 2015.
- [74] T. Ulrych, and R. Clayton, “Time Series Modeling and Maximum Entropy,” *Physics of the Earth and Planetary Interiors*, vol. 12, pp. 188–200, Aug. 1976.
- [75] S. Shon, and K. Mehrotra, “Performance Comparisons of Autoregressive Estimation Methods,” in *International Conference on Acoustics, Speech, and Signal Processing*, Mar. 1984, pp. 14.3.1–14.3.4.
- [76] R. Schmidt, “Multiple Emitter Location and Signal Parameter Estimation,” *IEEE Transactions on Antennas and Propagation*, vol. AP-34, no. 3, pp. 276–280, Mar. 1986.
- [77] M. Pichler, P. Gulden, M. Vossiek, and A. Stelzer, “A 24-GHz Tank Level Gauging System with State-Space Frequency Estimation and a Novel Adaptive Model Order Selection Algorithm,” in *International Microwave Symposium Digest*, Philadelphia, Pennsylvania, USA, Jun. 2003, pp. 1953–1956.
- [78] MATLAB. “Spectral Analysis.” (Jul. 2020), [Online]. Available: <https://de.mathworks.com/help/signal/spectral-analysis.html>.
- [79] M. Baginski, D. Faircloth, and M. Deshpande, “Comparison of Two Optimization Techniques for the Estimation of Complex Permittivities of Multilayered Structures Using Waveguide Measurements,” *IEEE Transactions on Microwave Theory and Techniques*, vol. 53, no. 10, pp. 3251–3259, Oct. 2005.
- [80] J. Jebramcik, J. Barowski, and I. Rolfes, “Characterization of Layered Dielectric Materials Using Ultra-Wideband FMCW-Radar Measurements,” in *Asia-Pacific Microwave Conference*, Kyoto, Japan, Nov. 2018, pp. 1327–1329.
- [81] C. Balanis, *Advanced Engineering Electromagnetics*, 2nd ed. Hoboken, New Jersey, USA: John Wiley & Sons, 2012.
- [82] A. Vasicek, “Sur la réflexion de la lumière sur des verres supportant des couches minces multiples,” *Journal de Physique et le Radium*, vol. 11, no. 7, pp. 342–345, Jul. 1950.
- [83] C. Katsidis, and D. Siapkias, “General Transfer-Matrix Method for Optical Multilayer Systems with Coherent, Partially Coherent, and Incoherent Interference,” *Appl. Opt.*, vol. 41, no. 19, pp. 3978–3983, Jul. 2002.
- [84] O. Heavens, “Optical Properties of Thin Films,” *Reports on Progress in Physics*, vol. 23, no. 1, pp. 1–65, Jan. 1960.
- [85] J. Jebramcik, I. Rolfes, N. Pohl, and J. Barowski, “Millimeterwave Radar Systems for In-Line Thickness Monitoring in Pipe Extrusion Production Lines,” *IEEE Sensors Letters*, vol. 4, no. 5, May 2020.

-
- [86] A. Ludloff, *Praxiswissen Radar und Radarsignalverarbeitung*, 4th ed. Wiesbaden, Germany: Vieweg+Teubner Verlag, 2009.
- [87] M. El-Shennawy, B. Al-Qudsi, N. Joram, and F. Elinger, “Fundamental Limitations of Phase Noise on FMCW Radar Precision,” in *International Conference on Electronics, Circuits and Systems*, Monte Carlo, Monaco, Dec. 2016, pp. 444–447.
- [88] S. Ayhan, S. Scherr, A. Bhutani, B. Fischbach, M. Pauli, and T. Zwick, “Impact of Frequency Ramp Nonlinearity, Phase Noise, and SNR on FMCW Radar Accuracy,” *IEEE Transactions on Microwave Theory and Techniques*, vol. 64, no. 10, pp. 3290–3301, Oct. 2016.
- [89] R. Nuzzo, “Statistical Errors,” *Nature*, vol. 506, pp. 150–152, Feb. 2014.
- [90] “SciPy.” (Jul. 2020), [Online]. Available: <https://docs.scipy.org/doc/scipy/reference/generated/scipy.stats.kstest.html>.
- [91] S. Kay, *Fundamentals of Statistical Signal Processing: Estimation Theory*. Upper Saddle River, New Jersey, USA: Prentice-Hall, Inc., 1993.
- [92] “SciPy.” (Jul. 2020), [Online]. Available: <https://docs.scipy.org/doc/scipy/reference/generated/scipy.stats.normaltest.html>.
- [93] V. Vovk and R. Wang, “Combining p-values via averaging,” *Biometrika*, vol. 107, no. 4, Jun. 2020.
- [94] A. Papoulis, *Signal Analysis*. New York City, New York, USA: McGraw-Hill, 1977.
- [95] S. Scherr, S. Ayhan, M. Pauli, and T. Zwick, “Accuracy Limits of a K-Band FMCW Radar with Phase Evaluation,” in *Proceedings of the 9th European Radar Conference*, Amsterdam, Netherlands, Oct.–Nov. 2012, pp. 246–249.
- [96] F. Bao, “Sparse Overcomplete Representation Applied to FMCW Reflectometry for Non-Uniform Transmission Lines,” Ph.D. dissertation, Technical University of Munich, Munich, Germany, Oct. 2015.
- [97] P. Stoica, R. Moses, B. Friedlander, and T. Söderström, “Maximum Likelihood Estimation of the Parameters of Multiple Sinusoids from Noisy Measurements,” *IEEE Transactions on Acoustics, Speech, and Signal Processing*, vol. 37, no. 3, pp. 378–392, Mar. 1989.
- [98] I. Pupeza, R. Wilk, and M. Koch, “Highly Accurate Optical Material Parameter Determination with THz Time-Domain Spectroscopy,” *Optics Express*, vol. 15, no. 7, pp. 4336–4350, Apr. 2007.
- [99] P. Queffelec, P. Gelin, J. Gieraltowski, and J. Loäec, “A Microstrip Device for the Broad Band Simultaneous Measurement of Complex Permeability and Permittivity,” *IEEE Transactions on Magnetics*, vol. 30, no. 2, pp. 224–231, Mar. 1994.

-
- [100] M. Requena-Pérez, A. Albero-Oritz, J. Monzó-Cabrera, and A. Díaz-Morcillo, “Combined Use of Genetic Algorithms and Gradient Descent Optimization for Accurate Inverse Permittivity Measurements,” *IEEE Transactions on Microwave Theory and Techniques*, vol. 56, no. 2, pp. 615–624, Feb. 2006.
- [101] J. Barowski, M. Zimmermanns, and I. Rolfes, “Millimeter-Wave Characterization of Dielectric Materials Using Calibrated FMCW Transceivers,” *IEEE Transactions on Microwave Theory and Techniques*, vol. 66, no. 8, pp. 3683–3689, Aug. 2018.
- [102] S. Boyd, and L. Vandenberghe, *Convex Optimization*. Cambridge, UK: Cambridge University Press, 2004.
- [103] J. Nelder, and R. Mead, “A Simplex Method for Function Minimization,” *Computer Journal*, vol. 7, pp. 308–313, Jan. 1965.
- [104] J. Lagarias, J. Reeds, M. Wright, and P. Wright, “Convergence Properties of the Nelder-Mead Simplex Method in Low Dimensions,” *SIAM Journal on Optimization*, vol. 9, no. 1, pp. 112–147, Dec. 1998.
- [105] R. Haupt, “An Introduction to Genetic Algorithms for Electromagnetics,” *IEEE Antennas and Propagation Magazine*, vol. 37, no. 2, pp. 7–15, Apr. 1995.
- [106] MATLAB. “Nelder-Mead Simplex Method.” (Jul. 2020), [Online]. Available: <https://de.mathworks.com/help/matlab/ref/fminsearch.html>.
- [107] H. Curry, “The Method of Steepest Descent for Non-Linear Minimization Problems,” *Quarterly of Applied Mathematics*, vol. 2, no. 3, pp. 258–261, Oct. 1944.
- [108] K. McKinnon, “Convergence of the Nelder-Mead Simplex Method to a Nonstationary Point,” *SIAM Journal on Optimization*, vol. 9, no. 1, pp. 148–158, 1998.
- [109] National Instruments. “Data Acquisition Board.” (Sep. 2020), [Online]. Available: <https://www.ni.com/de-de/support/model.pci-6115.html>.
- [110] DIN. “DIN 1986-100.” (Jul. 2020), [Online]. Available: <https://www.din.de/de/mitwirken/normenausschuesse/naw/wdc-beuth:din21:264064948>.
- [111] EN. “DIN EN 752.” (Jul. 2020), [Online]. Available: <https://www.din.de/de/mitwirken/normenausschuesse/naw/wdc-beuth:din21:263746339>.
- [112] N. Pohl, T. Jaeschke, and K. Aufinger, “An Ultra-Wideband 80 GHz FMCW Radar System Using a SiGe Bipolar Transceiver Chip Stabilized by a Fractional-N PLL Synthesizer,” *IEEE Transactions on Microwave Theory and Techniques*, vol. 60, no. 3, pp. 757–765, Mar. 2012.

-
- [113] M. Pauli, B. Göttel, S. Scherr, A. Bhutani, S. Ayhan, W. Winkler, and T. Zwick, “Miniaturized Millimeter-Wave Radar Sensor for High-Accuracy Applications,” *IEEE Transactions on Microwave Theory and Techniques*, vol. 65, no. 5, pp. 1707–1715, May 2017.
- [114] J. Grzyb, K. Statnikov, N. Sarmah, B. Heinemann, and U. Pfeiffer, “A 210–270-GHz Circularly Polarized FMCW Radar with a Single-Lens-Coupled SiGe HBT Chip,” *IEEE Transactions on Terahertz Science and Technology*, vol. 6, no. 6, pp. 771–783, Nov. 2016.
- [115] S. Saponara, M. Greco, and F. Gini, “Radar-on-Chip/in-Package in Autonomous Driving Vehicles and Intelligent Transport Systems: Opportunities and Challenges,” *IEEE Signal Processing Magazine*, vol. 36, pp. 71–84, Sep. 2019.
- [116] National Instruments, *4 GHz Vehicle Radar Test System*, Product Flyer, Austin, Texas, USA, 2020.
- [117] Texas Instruments, *AWR1642 Single-Chip 77- and 79-GHz FMCW Radar Sensor*, Data Sheet, revised Apr. 2020, Dallas, Texas, USA, May 2017.
- [118] Infineon. “Automotive Radar.” (Jul. 2020), [Online]. Available: <https://www.infineon.com/cms/en/product/sensor/radar-image-sensors/radar-sensors/radar-sensors-for-automotive/#!products>.
- [119] Analog Devices. “High Performance 76-81GHz 28nm RF CMOS Automotive Radar.” Video. (Jul. 2020), [Online]. Available: <https://www.analog.com/en/education/education-library/videos/5339313132001.html>.
- [120] R. Hult, G. Campos, E. Steinmetz, L. Hammarstrand, P. Falcone, and H. Wymeersch, “Coordination of Cooperative Autonomous Vehicles: Toward Safer and More Efficient Road Transportation,” *IEEE Signal Processing Magazine*, vol. 33, pp. 74–84, Nov. 2016.
- [121] A. Jász, A. Rák, I. Ladjászki, and G. Cserey, “Classical Molecular Dynamics on Graphics Processing Unit Architectures,” *Wiley Interdisciplinary Reviews: Computational Molecular Science*, vol. 10, Sep. 2020.
- [122] D. Geer, “Industry Trends: Chip Makers Turn to Multicore Processors,” *Computer*, vol. 38, pp. 11–13, May 2005.
- [123] C. Hung, F. Magoulès, M. Qiu, R. Hsu, and C. Lin, “Embedded Multi-Core Computing and Applications,” *The Journal of Supercomputing*, vol. 73, 3327–3332, Jul. 2017.